FINITE ELEMENT BASED MICROMECHANICAL ANALYSIS OF PRECIPITATED NITI SHAPE MEMORY ALLOYS

A Thesis

by

AUSTIN EDWARD COX

Submitted to the Office of Graduate and Professional Studies of
Texas A&M University
in partial fulfillment of the requirements for the degree of

MASTER OF SCIENCE

Chair of Committee,	Dimitris Lagoudas
Committee Members,	Ibrahim Karaman
	Theocharis Baxevanis
	John Whitcomb
Head of Department,	Rodney Bowersox

August 2015

Major Subject: Aerospace Engineering

ABSTRACT

In recent years, great strides have been taken in the advancement of Shape Memory Alloy (SMA) modeling capabilities. The accompaniment of advanced constitutive models with standardized solution techniques have meant that we can dive deeper into the material and its thermomechanical response than ever before. The most widely modeled and produced SMA class in industry today is one which hosts Ni as a core component of its composition, and usually takes the form of NiTi. When these SMA materials are heat treated, particles form in the microstructure and the material response changes drastically. This work directly models aspects of the precipitated microstructure by creating a modeling framework based on the Finite Element Method (FEM).

The framework is able to conduct micromechanical studies through the use of cubic Representative Volume Elements (RVEs) where the response of the SMA material matrix is driven by a currently developed SMA model with extended capabilities. The RVEs have Periodic Boundary Conditions (PBCs) applied to the cube faces, satisfying the assumption that the cube of material is an excerpt of a continuous material microstructure. Under these conditions, coherency stresses are introduced into the material through the introduction of elastic Eshelby-type stresses. The material has Ni depleted under the assumption of Fickian diffusion in accordance to the presence of precipitates, giving a heterogeneous distribution of Ni in the matrix, and the final conditioned microstructure is taken through a thermomechanical cycle. The final

responses of the material are extracted as the volume average response of the microstructure during these cycles.

The current work is broken down into two studies. The first study utilizes the newly developed framework in order to probe various changes in the microstructure which may come about during precipitation, and to determine effects of precipitate volume fraction on the material's macroscopic response. Of key interest in this study are the results of stresses arising from particle coherency with the matrix, changes due to Ni depletion arising from precipitation, and effects arising from purely structural interactions in the microstructure. The study shows that the presence of precipitates in SMAs smoothens their hysteretic behavior, decreases transformation strains, and shifts transformation temperatures to higher values.

The subsequent study takes this modeling framework and applies it to predict responses of precipitated materials. It does this by estimating precipitate volume fractions in a heat treated material, and building and solving RVEs to predict the effective response of the precipitated material. The predicted RVE responses are then compared to experimental results. Excellent agreement is seen for low volume fractions of precipitates while trends are captured for higher estimated volume fractions.

Using this modeling framework to understand the effects of various aspects of the aforementioned precipitation can help in the design of future materials and in the prediction of their energetic responses.

DEDICATION

I would like to dedicate this work to my mother and father, without whom I would not have had my passion for science which has entertained my mind for so long. They have graciously shared their knowledge of this world, and selflessly sacrificed time in their own lives in order to direct me in my own. They have not only taught me the basics of mathematics and language, but also have taught me to take in the love and advice of others. They have taught me focus and conformity, but also independence. And for that I owe them the world and much more.

For mein 母 et père e .م عالا

ACKNOWLEDGEMENTS

Firstly, I would like to thank my parents for their help throughout all of my schooling. They have always been there for me.

I would like to thank my brothers for being around when some good entertainment is needed. I know they are working hard and keeping the athletic side of the family well alive.

I would like to also thank the many mentors I was fortunate to have growing up that kept and pushed my interest in the maths and sciences, and life in general, specifically Susan Anderson and Sohail Khan. They were not only paid teachers, but took their work a step further in putting passion into their classrooms far beyond what was necessary, and many students have benefited from their teachings.

In coming to Texas A&M I had originally planned on pursuing a bachelor's degree and going into industry, but at the university I found many more opportunities outside of class. I found many of the professors to be friendly and had the fortune of being involved in research my second year at the university. This research under Dr. Zoubeida Ounaies sparked my initial interest in materials research and showed me that I wanted to achieve more than my undergraduate degree in aerospace engineering. For that spark and for the years of research under her I am forever thankful.

Outside of the department I had the opportunity to join many organizations and learn the social aspect of life. One of these organizations was my fraternity, Delta Sigma Phi, Theta Upsilon chapter at Texas A&M. These men were a great inspiration to me as

many of them were very hard workers and loving friends. They were a constant source of advice in my undergraduate career and always helped bring fresh ideas into my life. I have been with them in waters warm and cold, listened to tales from their young and old, travelled with them from sea to shining sea, and have truly learned how to become a better, well-rounded man from my time with them.

I would like to thank some specific mentors during my time under the guidance of work related to and leading up to my Master's degree. In my last year of undergraduate study I came upon a post-doc, Dr. Yves Chemisky, who became my mentor in this time. He was not only a mentor, but a friend while he was here. He kept me focused, taught me how to be an inspiration to others, and taught me how to charge full speed ahead towards a goal. In the time he was here he provided pivotal guidance that told the group I was worthy of staying for a higher degree, and with his guidance I very quickly improved my knowledge of computer languages and programming skills far beyond a basic working level. I would like to thank him for his mentorship not only in that time, but also during work travel to France where he greatly helped with administration technicalities and adjustment to the unfamiliar culture. With his help I was able to develop an (almost) working level of the French language and thrive in the new environment quite foreign to my usual life.

During a separate work visit to Europe, I met another great mentor named Dr. Jan Frenzel, a member of the super alloys group under Dr. Gunther Eggeler in Ruhr University, Bochum, Germany. Jan was always kind and had a joyous disposition about his work and students. Under his guidance I learned about the state-of-the-art techniques

and equipment used in making shape memory and superalloy materials, and without his insight, would never have known enough about the real-world side to the processing of these materials to present my thesis.

One person that was crucial in my studies as a master student was Dr. Theocharis Baxevanis. He was not only essentially my direct boss, but also my mentor and a good friend. He was there with me for my entire research period, and helped immensely with much of the formulation of my early work when I lacked experience and insight. His ideas and style of thinking, being completely different from my own, allowed me to see the opposing side of any argument without even having to leave the building. For his insight and guidance I am deeply grateful.

Finally I would like to thank Dr. Dimitris Lagoudas who has given me the opportunity to study under him, and all the resources necessary to conduct some very interesting research. He has taught me to have a new favorite word, "collaboration" and has given me the opportunity to use this word on more occasions than I can count. I am deeply indebted to him for all his help. Even as he rose from department head into the dean's office, taking on ever more work, he found ever more energy to have weekly meetings with me and all of his students. I am eternally thankful for his time and insight.

I would specifically like to thank the AFOSR, whose funding has helped put me through the master's program, and whose research project has been great fun to work on.

Also, I would like to thank the administration at Texas A&M, specifically Karen Knabe and Bonnie Reid, whose behind the scenes work has helped the department and its students to run (in the best fashion of engineering) like a well-oiled machine.

TABLE OF CONTENTS

Page

LIST OF FIGURES

Page

LIST OF TABLES

Page

CHAPTER I

INTRODUCTION AND LITERATURE REVIEW

Shape Memory Alloys (SMAs) are materials which are able to produce mechanical work from thermal variation and vice versa. This material property comes about through a diffusionless phase change between two crystallographic states of the material, austenite at high temperature, and martensite at low temperature. The phase change causes a lattice shear which develops high elastic strains in the material termed transformation strains. The amount of attainable strain varies in accordance with composition and processing but typically induces strain upwards of a few percent. Today, much of the focus on SMA research is on NiTi and NiTi-based systems as they have well developed processing methods and relatively stable response. Currently, one of the prominent methods to process the material includes a furnace aging step which changes the microstructure from nominally homogeneous NiTi into one with many precipitates. The introduction of such particles has many benefits which are discussed later. For the case of aging Ni-rich NiTi, the majority of heat treatments result in particles which have a composition of Ni_4Ti_3 [1]. These particles are non-transforming, have a higher stiffness than the SMA matrix, and can constitute a volume fraction of the material upwards of 10% [2, 3]. Being Ni-rich, they also change the fundamental atomic composition of the matrix, reducing the ratio of Ni to Ti, which has a direct impact on the material's effective transformation temperatures [4]. Although there has been much work in development of these precipitated materials and modeling their macroscopic

response, little work has focused on direct modeling of the precipitates on a *microscopic* scale and determining the microstructural effects on *macroscopic* properties.

Motivation

The purpose of this work is to use a microstructurally informed model to determine the effects of precipitation on the macroscopic thermomechanical response of SMAs using the Finite Element Method (FEM) [5]. The use of Finite Elements (FEs) to directly model the microstructure allows one to account for many features which would be neglected or approximated using other methods. For instance, in Ni-based SMAs it is known that particle-particle interactions, effective Ni content and local Ni distribution play key roles in the material's thermomechanical response [3, 4]. Direct evidence of this is given through TEM micrographs of precipitated NiTi materials near phase transformation temperatures which demonstrate the non-uniformity of martensitic transformation throughout the microstructure. The images show clear evidence that phase transformation features are heavily influenced by the existence of the precipitates, showing that one martensite variant pair will form between a pair of precipitates, a different pair between two other precipitates, and austenite between two other precipitates, all in a single TEM image. These features are demonstrated in Figure 1. Such local variations demonstrate the heterogeneity of transformation at the microstructural level and motivate the need for a microscopically informed model to probe these non-uniformities and determine their effects on the material's macroscopic response.

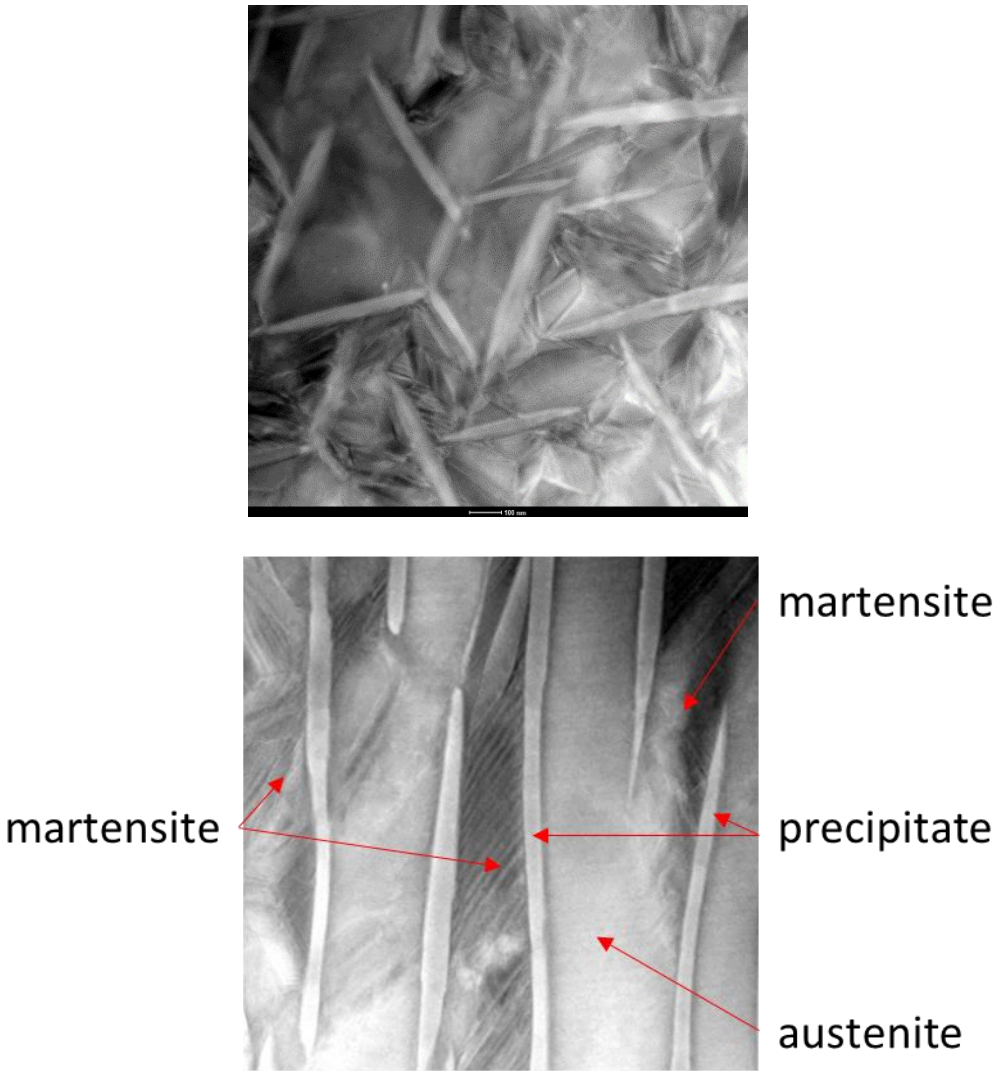

Figure 1. Microstructure of precipitated NiTi SMA showing Ni_4Ti_3 precipitates, austenite, and martensite structures

A model is hereby proposed which will be informed from processes inherent to multiple length-scales, similar to Figure 2. It will incorporate features from the crystal lattice, up to the level of multiple precipitates and polycrystalline structure. Incorporating information at these different length scales will allow for the inclusion of

key microstructural features and processes, namely diffusion of Ni in the lattice, coherency between individual particles and the matrix, and particle-particle interactions.

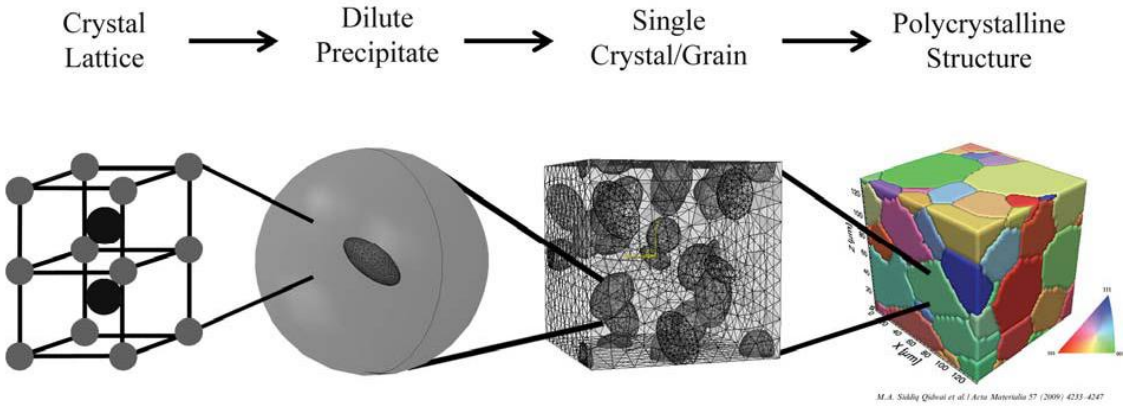

Figure 2. Length scale heiarchy of modeling microstructural features [90]

The result is a modeling framework described in Chapter II that is used initially in Chapter III to explore effects of microstructural features and ultimately in Chapter IV to predict the changes in properties of SMAs due to precipitation. Having such a framework is useful to give insight to specific effects associated with second phase particles and their interactions, and to assist in selecting material processing steps to obtain desired thermomechanical responses. The framework is built around a robust Finite Element Analysis (FEA) package, Abaqus, and makes use of their User MATerial subroutines (UMATs) for various computations.

A portion of Figure 2 is reprinted with permissions from "Using image-based computational modeling to study microstructure–yield correlations in metals" by

Qidwai, S.M., and Lewis, A.C, and Geltmacher, A.B, 2009, Acta Materialia. doi:10.1016/j.actamat.2009.05.021

Shape Memory Alloys

Shape Memory Alloys are a class of intermetallic active materials which are able to convert energy between thermal and mechanical forms. The underlying mechanism of this conversion is a reversible diffusionless phase transformation between a high-order austenite phase and a low-order martensite phase [1, 6]. This phase change induces strains >1% in the material at loads surpassing 100MPa as seen in Figure 3, making it an excellent candidate as a high work density actuator. Investigated applications in actuation range from using SMA wires to create self-folding SMA structures [7], to integration into bio-inspired devices for propulsion [8], and even on aircraft engine cowlings for noise-reduction [9] and spacecraft for deployment of solar panels [10].

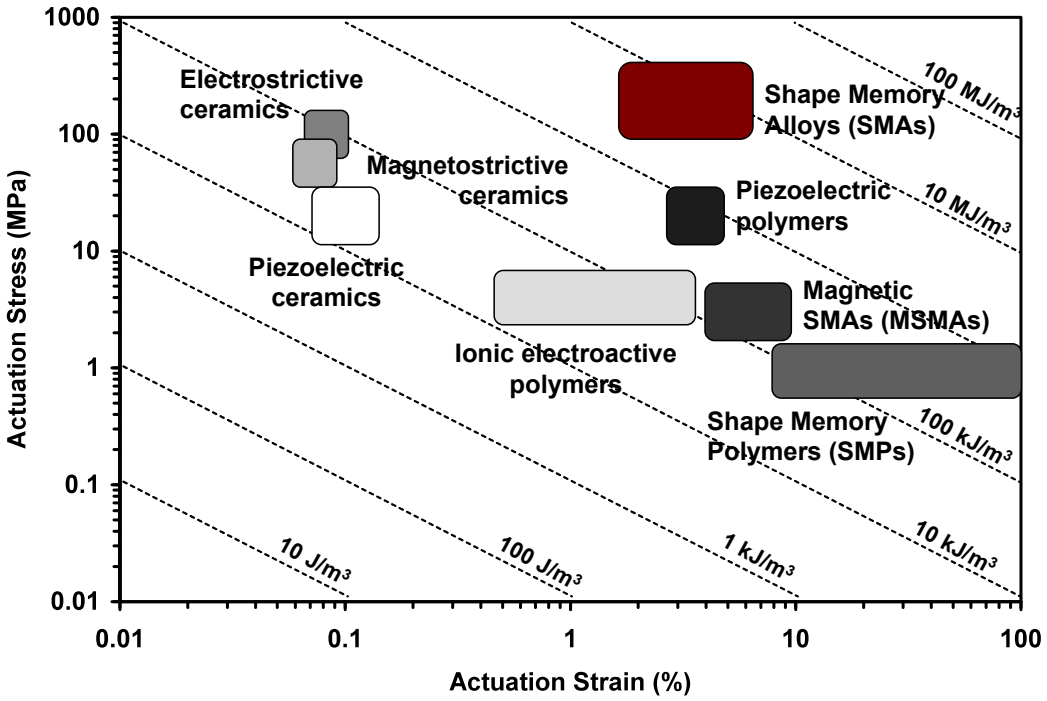

Figure 3. Work density of smart materials [11]

The focus of this paper will be on NiTi, a highly used class of SMAs. This alloy system is known to be one of the most stable and high work output SMAs available, and receives a considerable amount of focus in SMA research and production today [11, 12].

Figure 3 is reprinted with permission from chapter 1 of the book "Introduction to Shape Memory Alloys" by D.C. Lagoudas, and P.K. Kumar, 2008.

Phase Change

The primary driving mechanism of a shape memory alloy's ability to undergo high macroscopic deformations is the atomic lattice shearing produced when taken from a stressed austenitic state to detwinned martensitic state. In order to change atomic

lattice configuration to martensite the material must shear to form either self-accommodated (twinned) martensite preserving shape, or detwinned martensite (if the material is under stress), causing macroscopic shape change. The martensite has the ability to take the form of various specific lattice configurations depending on the material and processing, but in general is orthorhombic, tetragonal or monoclinic while the austenitic state is of cubic form. The phase change is able to be induced by a change in temperature, stress, or a combination thereof, and may form varying amounts of twinned and detwinned martensite in the microstructure along a number of transformation directions depending on the exact nature of the stress and temperature fields. The formation of the detwinned state is of primary concern in this paper as the attainment of the high associated strains associated with a detwinned martensitic state are what give the material its excellent properties as a high work density actuator [13]. This has produced uses for SMA materials in fields including aerospace [14-18], biomedical [19-21], and many others [22-24].

The diagram shown in Figure 5 demonstrates the most common thermomechanical paths in stress-temperature space which produce macroscopic deformation in SMA materials, while Figure 4 gives the primary material parameters. If the material begins in the austenitic state, it will begin to change phases into martensite along the solid line which terminates at M_s. Transformation will complete once it reaches the dashed line emanating from M_f, having partial transformation in-between. The amount of transformation strain attained is dependent on many features of the material, but varies in accordance with the stress level (and associated amount of

detwinned martensite formed) at which the material is transformed. If beginning in the martensite phase, the material will start to change into austenite along the solid line which terminates at A_s and will complete transformation once it reaches the dashed line above A_f, recovering its transformation strain. These four transformation temperatures, M_s, M_f, A_s, and A_f are the temperatures at which the material begins and finishes phase change under no externally applied load. Their shifts in temperature at non-zero stress levels are given by the Clausius-Clapeyron relation, shown for each phase change as C_M and C_A. The red lines in the diagrams are associated with the material twinning where below the dashed line, nearly all material forms in a twinned state and above the solid line, the vast majority forms detwinned.

Three of the most common thermomechanical paths taken by SMAs are given in Figure 5 and described following:

- Shape Memory Path

  Material is cooled to martensite, then loaded to induce detwinning in the martensitic phase to achieve deformation. Then it is unloaded and heated back into austenite, recovering its original shape. This path is less used in application, but is the most classical path and is commonly used for demonstration of the material's ability to recover shape.

- Pseudoelastic Path

  Material initially in austenite is increasingly stressed until phase change into martensite occurs. The material is then unloaded back to austenite. This path

is typically used for damping applications where the phase change is able to absorb energy put into the system [9, 25, 26].

- Actuation Path

  Material is stressed, then thermally cycled at constant stress such that phase change occurs. This path is typically used such that the change in strain results in utilized actuation and has the potential to replace smaller electric or hydraulic actuators. This ability to deform and recover makes it suitable as a solid state actuator driven by changes in temperature, deriving use in many industries [27-29].

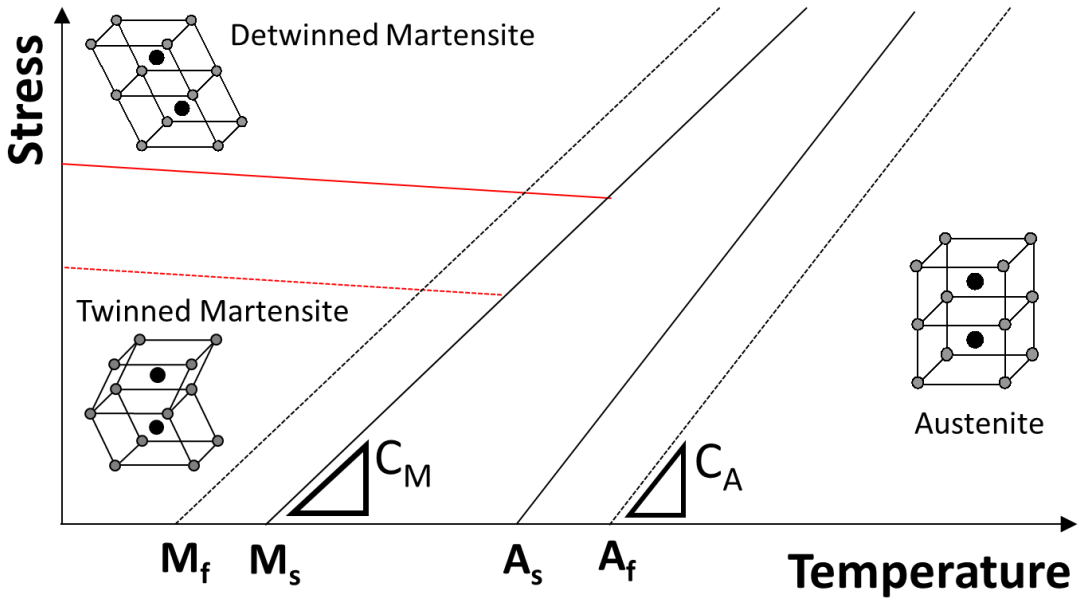

Figure 4. Essential phase diagram for SMAs in stress-temperature space

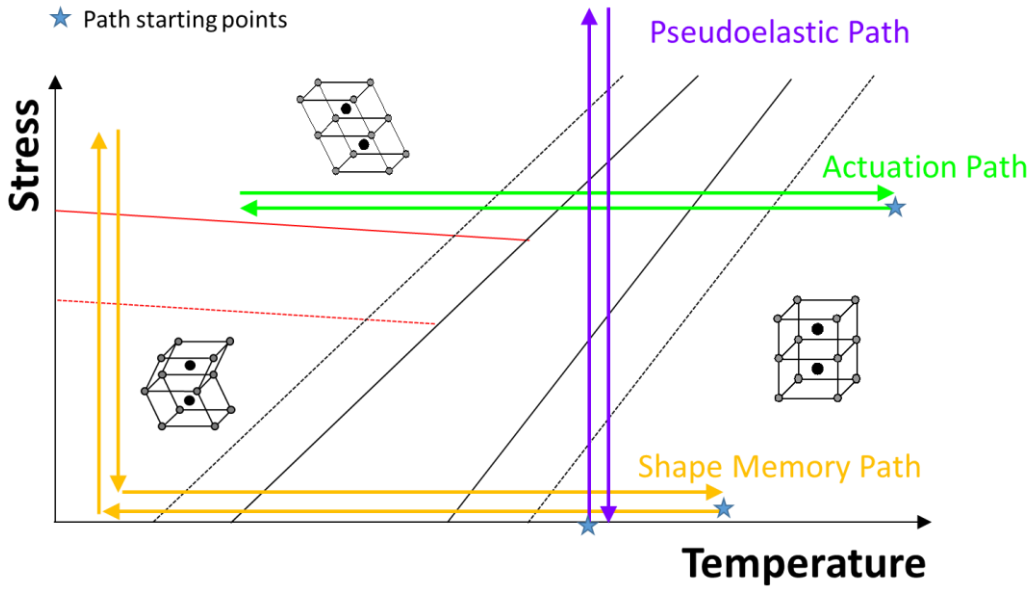

Figure 5. Phase diagram of SMAs showing typical thermomechanical paths

A majority of the work presented in this paper will focus on the actuation path. Examples of typical actuation responses for both a solutionized and a precipitated SMA under different uniaxial tensile loads are shown in Figure 6 and Figure 7 respectively. In these figures, the applied stress ranges from 0-300MPa and it is seen that where the solutionized material response (Figure 6) includes large amounts of irrecoverable strain at the end of a 200MPa cycle, almost no residual strain occurs even at the highest stress level in the precipitated material (Figure 7), though the material strains approximately 6% during transformation. Also some of the features described in the phase diagram can be seen, such as the transformation temperatures (marked in Figure 7) and the increase in transformation temperatures when higher stresses are applied (both figures).

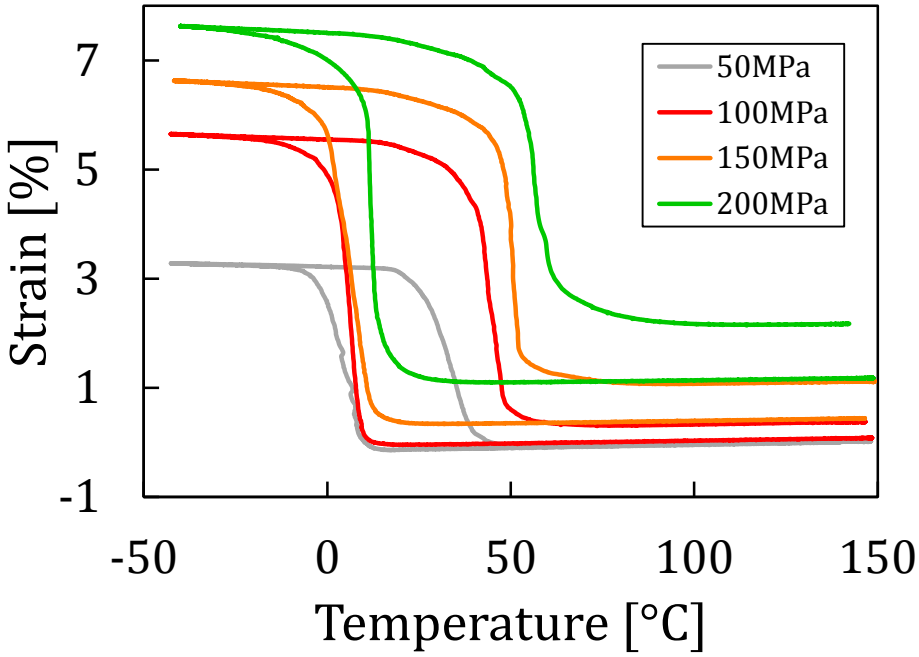

Figure 6. Typical actuation response of solutionized NiTi SMA

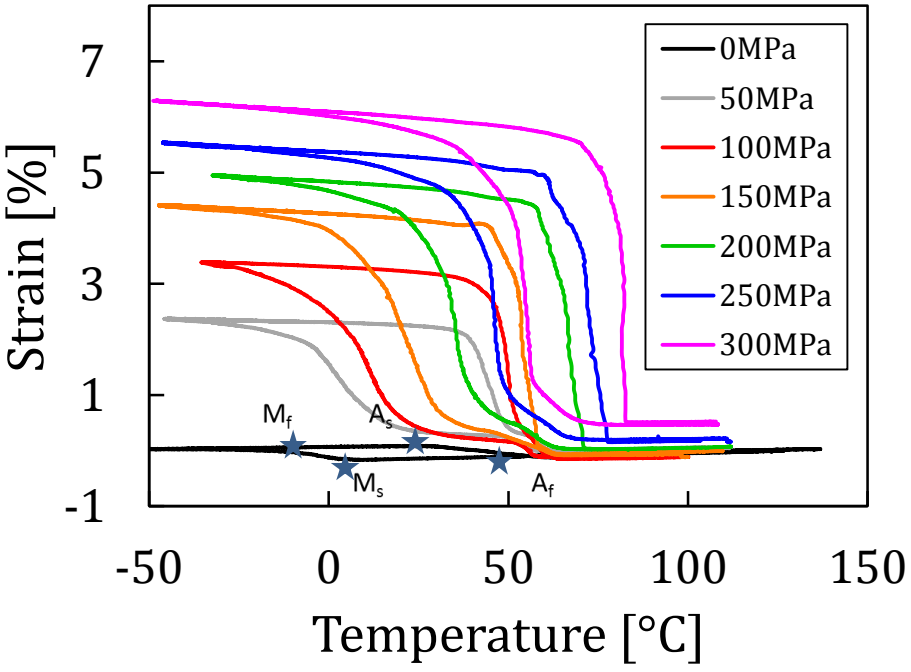

Figure 7. Typical actuation response of precipitated NiTi SMAs

Background of Precipitation in SMAs

Since the properties of any material are highly dependent on the manufacturing process, and SMAs are notorious for being sensitive to small variations in the processing conditions [30-36], they require highly controlled environments for processing. In Ni-rich NiTi, a small difference in initial composition will result in a large change in transformation temperatures, with a 1at.% difference in Ni composition shifting transformation temperatures upwards of 100°C [4, 37]. The materials have to be vacuum sealed under argon when at elevated temperature to minimize impurity uptake [30, 33, 38], and melting crucibles are typically graphite based in order to maintain higher purity during melting since even small volume fractions of impurities can greatly alter the material's thermomechanical response and fatigue life [39].

In order to produce an SMA ready for application, the material is taken through many processing steps. A typical processing path for NiTi material is as follows:

1. Purified Ni pellets and Ti rods are melted together in a graphite crucible in an argon filled and evacuated chamber using the Vacuum Induction Melting (VIM) process [40].
2. The resulting mixture is re-melted a number of times in order to create a homogeneous distribution of Ni and Ti in the material.
3. The material is then processed at elevated temperature to form the initial billets of homogenized material (hot rolling or hot extrusion for our materials).

Further processing steps vary depending on the desired application of the material, but may include a step in which the material is again placed in an evacuated chamber sealed under argon, and held in a furnace for a specified duration at elevated temperature in order to form precipitates in the microstructure. Typical precipitation treatments of Ni-rich NiTi will form Ni-rich precipitates such as Ni_4Ti_3. The formation of these Ni_4Ti_3 particles via precipitation is known to affect the transformation behavior through a variety of mechanisms. These mechanisms are summarized by the following:

(1) The transformation temperatures are highly dependent on the Ni content [4]. Aging of Ni-rich precipitates depletes the Ni content of the matrix, increasing the transformation temperatures [41].

(2) The fraction of compound twins to type I and II twins changes with interparticle distance, and in cases where the interparticle distance is sufficiently small, the dominating twinning types change from type I and II twins to (001)m compound twins [42]. The additional energy required to form compound twins requires additional undercooling to initiate the martensitic transformation, so the M_s temperature decreases with interparticle distance [43].

(3) Compositional inhomogeneity surrounding precipitates leads to local differences in M_s. The Ni content immediately surrounding the precipitates is lower than that of the matrix, and transforms at a higher temperature [44].

(4) Coherent precipitates exist in a local stress field; these local stresses increase the transformation temperature of the matrix relative to the precipitate free regions [45].

(5) In order to remain coherent with the matrix, non-transforming precipitates must experience some shear during the transformation. This necessitates the storage of elastic energy in the precipitates, which corresponds to a decrease in transformation temperatures [46].

In this work we focus on the effect of precipitates on the thermomechanical response due to changes in composition and the presence of elastic gradients, which cover a majority of the previously stated mechanisms. These mechanisms are known to have a large effect on the transformation temperatures and thermomechanical response [43]. Long duration aging conditions reduce the effects of particle nucleation and compound twinning and produce larger particles which are closer to microscopic size. In cases where particles are large, the transformation temperatures should be affected primarily by the bulk change in composition and local gradient effects.

The evolution of precipitates in a supersaturated solution during aging can be divided into two different regimes; nucleation and coarsening. During the initial stages of aging the precipitate evolution is nucleation dominated, and the formation of new precipitates continuously decreases the average distance between precipitates. This increases the yield strength and suppresses the transformation temperatures [46]. During the subsequent coarsening regime, Ostwald ripening becomes the dominant effect. The free energy of the system is increased by the curvature of the precipitates; small

precipitates with large curvature are more energetic than large precipitates. So, the dissolution of small precipitates combined with the growth of large precipitates reduces the overall curvature driven by the reduction of free energy [47]. It is also expected that during coarsening the volume fraction and composition of the matrix remains relatively constant [48]. This means that after coarsening the interparticle distance becomes large and the size dependence effect on the transformation temperature can be reduced.

The final result of the aging procedure is a precipitated material which has minimal TRansformation Induced Plasticity (TRIP) due to the introduction of dislocation barriers and accompanying increase in critical stress required for slip [37], increased transformation temperatures from a lower effective Ni content in the matrix, and has better biocompatibility [49, 50], as the amount of Ni that may potentially leech from the material is reduced.

In order to explore how different mechanisms of precipitation change the macroscopic response of these materials, we turn to the field of micromechanics. Using theory from this field, one is able to take a relatively small domain of the material microstructure and determine the effective material response using appropriate boundary conditions. Not only can it give effective responses for the material, but since a random material subdomain containing many particles is simulated, microstructural features are taken into direct consideration, and various components of the microstructure may be studied in detail.

Background of Micromechanical Methods

Micromechanics-based simulations can be used to complement experimental efforts in exploring the influence of precipitation on the response and structural behavior of SMA material systems, thereby accelerating their development cycle for specific applications. Many micromechanical approaches are available to simulate the response of polycrystalline SMAs, including a host of long-established mean-field micromechanical models sparked by the works of Eshelby [51] and others on embedded inclusions. Notably, Lu and Weng developed a micromechanical theory to describe single crystal SMA behavior [52] which was subsequently adapted in a self-consistent polycrystal theory to determine the stress–strain response of NiTi SMAs at constant temperatures [53]. The same strategy was followed in [54, 55] to examine the structural effect of precipitates in polycrystalline SMA material systems. Some of the earliest work on SMA composite modeling utilized the Mori–Tanaka method [56-59] to predict effective inelastic composite responses [60, 61]. More recently, the Mori–Tanaka method was used in conjunction with spheroidal SMA inclusions to study the influence of embedded SMA particles on the strength of metal matrix composites [62].

In the past decade, finite element simulations have gained popularity as the level of available computational power continues to increase, especially with the increased use of distributed computing methods. Such finite element analyses are able to simulate the effect of microstructural features on the effective macroscopic response that may not be fully captured by mean-field approaches, such as the effect of Ni depletion during precipitation in Ni-rich NiTi SMAs.

There are many differences between full-field and mean-field based solution methods, with the key difference in how the microstructure is discretized for solution. Both methods use particle volume fraction, aspect ratio, and orientations as their main defining geometric quantities, and since particle size is not used directly, size effects are not captured through these methods except in material behavior definitions. Methodologies considering only the phase-averaged response of the various constituents are defined to be mean-field approaches while full-field methods are those in which the position dependent field values are determined and then averaged for the effective, macroscopic response.

Relating to the current work, the microstructure is comprised of two physical components, Ni_4Ti_3 precipitates and SMA matrix. For solution, the FEM breaks down each instance of these microstructural components into a set of simple geometries such as tetrahedrons. This allows points to be defined in the simple geometry as discreet solution points which are related to its immediate neighbors through Ordinary Differential Equations (ODEs). At the level of the entire domain, solutions are inter-related algebraically as a system of equations defined by a large matrix related to the connectivity between the individual solution points.

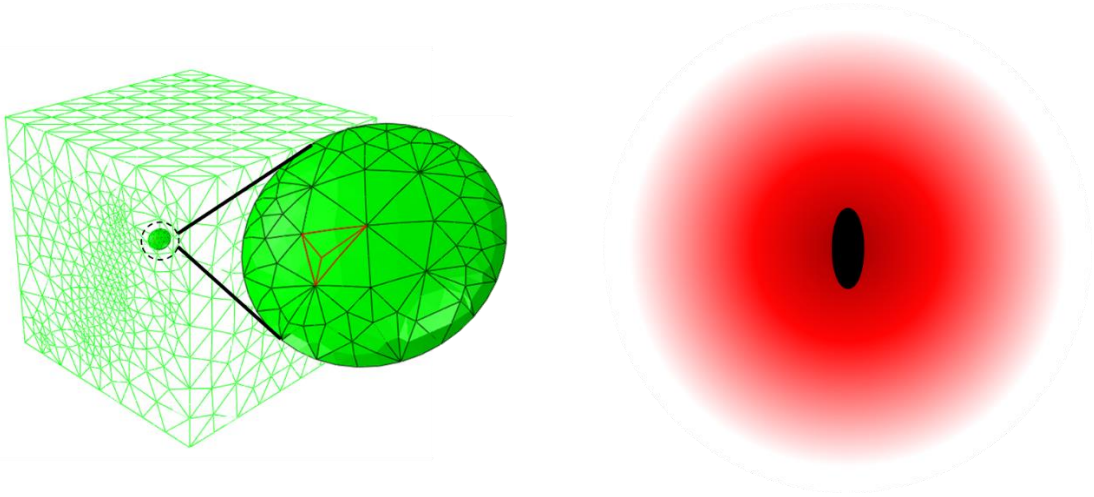

Figure 8. Precipitate and matrix domains in FEA and mean-field approaches

In contrast, Eshelby-based solution methods do not break down the microstructural components further than particle domains. Instead, they use the assumption of the existence of uniform eigenstrains inside particles to relate mechanical fields inside smooth geometries (precipitates) to the fields outside the geometries (matrix) based on assumptions about the loading and/or deformation. A visual comparison of FE and mean-field domains are given in Figure 8.

Also, the mean field approach takes into account particle-particle effects through incorporating their effects into the effective applied loading or boundary conditions of other particles, whereas the FEM models the particles (and therefore their interactions) discreetly. The discreet modeling allows the user to look at specific interactions and configurations of particles, for instance if they only appear along grain boundaries in a material, only form in pairs, or have other such spacing considerations.

Another advantage of the FEM approach is the ability to have pointwise defined material properties in the microstructure instead of averaged properties. The FEM is

inherently designed to discretize at this level, and requires little additional consideration for computation of heterogeneous fields, as relevant changes are local to the element domains. However, to have property variance in an Eshelby-based method, many new matrix domains must be added. For instance, to model a precipitated SMA, particles of a certain orientation are counted as a single domain, another orientation constitutes another domain, etc. and to have property variance in the SMA matrix domain, shell domains must be created around the particles, each with their own properties. In order to get a fine property distribution, many shells must be added, and as the microstructural domain becomes more discretized, solution time sharply increases and can easily surpass an equivalent problem formulated in a FE framework, but result in less accurate solutions. For these reasons, the presented work is based around the FEM.

Summary

This chapter introduces shape memory alloys and characteristics of their phase change mechanism, providing information about different typical loading paths taken. It gave the motivation for the thesis, namely that the thesis describes a modeling effort to simulate and predict the effective macroscopic response of precipitated NiTi SMAs using the finite element method in a micromechanical framework. This framework incorporates the concept of a periodic representative volume element including multiple discretely modeled Ni_4Ti_3 particles in an SMA matrix domain with an incorporated coherency stress field and diffuse material properties based on the solved eigenstrains and Ni profile in the microstructure. This domain then is then used for application of

macroscopic thermomechanical loading paths and solution of effective properties. The chapter also outlined the difference between the current method and other solution methods while providing reasons why the FE method was chosen.

Consideration of loading and boundary conditions are given in later sections. For the reasons listed in this section, specifically the ability to handle diffuse material properties, the finite element method was selected as the solution method for the precipitated SMA microstructures.

Notes about Presented Information

This work has close relations to a large amount of produced experimental data. I am deeply grateful to Mr. Brian Franco and Dr. Ibrahim Karaman for conducting experiments and allowing me access to the resulting data. All presented laboratory experimental data in this thesis comes from their hard work unless otherwise specified.

Outline of the Thesis

- Chapter II describes in detail the developed modeling framework which is used to construct and solve microstructural models of precipitated SMAs. It will give details of the methods used to generate the microstructures and prepare them for analysis, as well as methods used in computing particle/matrix coherency, Ni diffusion patterns, and the effective thermomechanical response.
- Chapter III presents an exploration of the use of such analysis tools to determine how precipitation affects characteristics of the effective material response of precipitated NiTi SMAs. Numerous volume fractions of particles are taken through both actuation and pseudoelastic cycles, effective thermomechanical responses are extracted and macroscopic material properties are estimated.
- Chapter IV demonstrates the use of the developed model to predict responses of precipitated NiTi SMA materials. Predictions are made and compared to experimental responses for a wide range of estimated precipitate volume fractions.
- Chapter V gives a summary of the presented work and describes where the developed modeling framework may be taken in the future.

CHAPTER II

MODELING FRAMEWORK*

In this paper, FE simulations based on material subvolumes are used to extract information on the effective response of precipitated Ni-rich NiTi SMAs using the concept of a Representative Volume Element (RVE). A RVE is a modeled material subdomain which has inherent randomness, but retains a large enough section of modeled material such that the effective response of the RVE is equivalent to that of the macroscopic material domain.

A modeling framework has been created to handle the multiple steps involved in the RVE analysis. It includes many scripts written in the coding language Python to handle all simulation setup and data processing, as well as a few UMATs written in the FORTRAN language to handle subroutines for computation during the FE analysis. Many of these codes and their functions are described in detail in this chapter and their necessity in the modeling process is explained. The first section describes the methods involved in generating the RVE, including the particle placement routine and general pre-processing, and describes the loading and boundary conditions applied in the analysis. The next section discusses the simulated materials and their constitutive responses. It then details the steps involved in running an analysis and extracting computed data, including the determination of the stress field arising from coherency

*Portions of this chapter are reprinted with permission from "Micromechanics of precipitated near-equiatomic Ni-rich NiTi shape memory alloys" by Baxevanis, T., Cox, A., and Lagoudas, D.C., 2014, Acta Mechanica. doi: 10.1007/s00707-013-1071-3.

between the particles and matrix, Ni profile in the matrix arising from precipitate formation and growth, and the determination of final thermomechanical response.

Boundary Value Problem

In this section, the Boundary Value Problem (BVP) is given for an analysis. Figure 9 shows the simplified BVP for an RVE, where RVE cube dimensions are given as L, and uniaxial tension is applied along the x_1 direction. The conservation laws and constitutive equations which are used in the analysis are given immediately following.

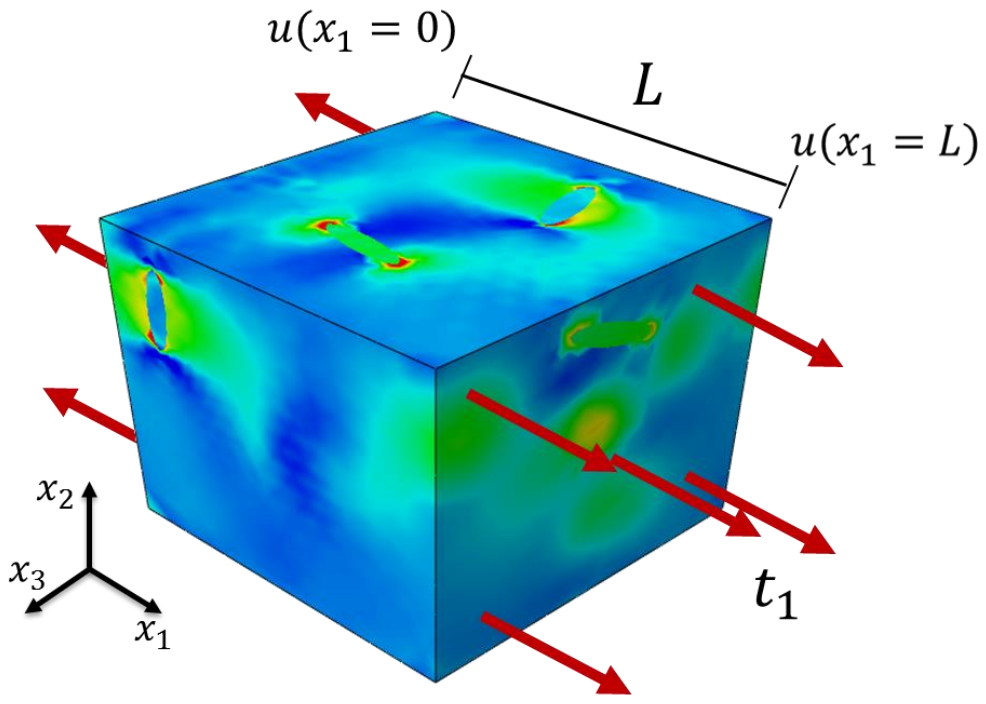

Figure 9. Simplified representation of the RVE boundary value problem showing coordinate system, RVE dimensions, coordinates, and loading directions

Summary of Constitutive Equations and Conservation Laws

All equations are given in indicial notation with respect to a 3D Cartesian coordinate system and come from theories of continuum- and micro-mechanics.

Thermomechanical Equations

- Conservation of linear momentum

This equation in another form is known as Newton's second law. With the assumptions of no acceleration or body forces, it is given as

$$\frac{\partial \sigma_{ij}}{\partial x_j} = 0 \tag{1.1}$$

where σ_{ij} are the components of the stress tensor in the body and x is the coordinate location.

- Kinematics

Kinematics describes the motion of the continuum. In our case it is given as

$$\varepsilon_{ij} = \frac{1}{2}\left(\frac{\partial u_i}{\partial x_j} + \frac{\partial u_j}{\partial x_i}\right) \tag{1.2}$$

where ε_{ij} are the components of the strain tensor and u_i, u_j are components of the displacement vector. Here, the small-strain assumption is used for both precipitate and matrix domains as the total strain of either domain in the analysis is typically below 5%, and under uniaxial tension the material will not experience large rotations.

- Effective macroscopic response

$$\Sigma_{ij} = \frac{1}{\Omega}\int_{\Omega} \sigma_{ij} dV, \; \mathrm{E_{ij}} = \frac{1}{\Omega}\int_{\Omega} \varepsilon_{ij} dV \tag{1.3}$$

The effective macroscopic stress and strain values are given as the average of the stress and strain values in the modeled domain Ω (the entirety of the RVE).

The following equations are given with respect to strain increment as they are implemented in a finite element framework which is formulated for incremental displacement.

- Constitutive response of Shape Memory Alloy matrix

Details of the full thermomechanical constitutive model for the SMA is given later in this chapter, however, for a strain increment, the constitutive response is as follows:

$$d\varepsilon_{ij} = S_{ijkl} d\sigma_{kl} + dS_{ijkl}\sigma_{kl} + d\varepsilon_{ij}^{t} + d\varepsilon_{ij}^{therm} \tag{1.4}$$

where d denotes an increment of the component value, and ε_{ij} are the components of the strain, S_{ijkl} are the components of the compliance tensor, ε_{ij}^{t} are the components of the transformation strain, and ε_{ij}^{therm} are the components of the thermal strain. This formula is given for rate-independent behavior.

- Constitutive response of Ni_4Ti_3 precipitates

$$d\varepsilon_{ij} = S_{ijkl} d\sigma_{kl} \tag{1.5}$$

The precipitates are modeled as elastic particles where the stress is directly related to the strain through the compliance tensor.

Diffusion Equations

- Conservation of Mass

For any equation where mass is shifted around but not created or destroyed, we must make sure that the mass is conserved. Conservation of mass is given as

$$\rho \frac{\partial v_i}{\partial x_i} + \frac{D\rho}{Dt} = 0 \tag{1.6}$$

where ρ is the material density, $\frac{\partial v_i}{\partial x_i}$ is the derivative of component velocity with respect to coordinate location, and $\frac{D\rho}{Dt}$ is the material derivative of density.

- Fickian diffusion

The classical equation describing diffusional processes is that of Fickian diffusion which is given by

$$\dot{c} = D \frac{\partial^2 c}{\partial x_i \partial x_i} \tag{1.7}$$

where $\dot{c}$ is the rate of change of the concentration, D is the diffusivity coefficient, and $\frac{\partial^2 c}{\partial x_i \partial x_i}$ is the Laplacian of the concentration value.

Steps of Thermomechanical Cycling

All RVE material is taken as initially in the austenite phase where ε_{ij}^{t} and ε_{ij}^{therm} are null valued. During cycling, these strains are developed and the response is measured and reported.

Pseudoelastic Path

The pseudoelastic path is typically utilized for dampening purposes and has excellent capability for energy absorption. Also, many commercial applications such as orthodontic wires and arterial stents utilize the loading portion of the path in order to respectively, provide resistance against teeth such that they align and straighten, and provide support to an artery such that good blood flow is maintained. The pseudoelastic loading path and material response are given in Figure 10 and Figure 11 respectively, and the path steps are described immediately following.

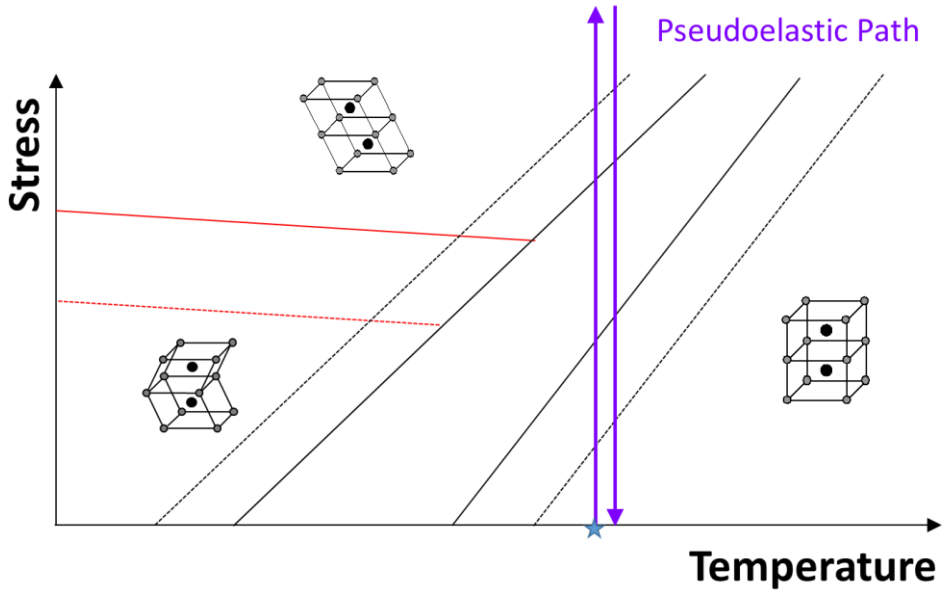

Figure 10. Pseudoelastic path in stress-temperature space

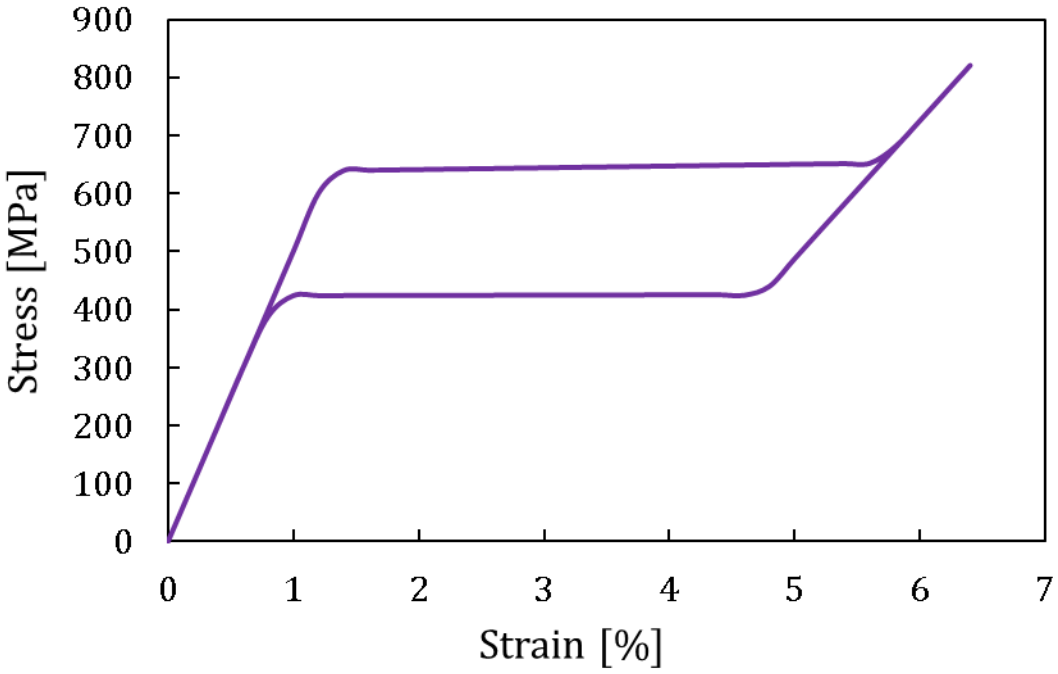

Figure 11. Example modeled pseudoelastic response of a NiTi SMA

Step 1: Loading

Material is maintained at constant temperature above A_f. It is loaded under uniaxial tension until the SMA matrix has completely changed phase to martensite.

Step 2: Unloading

Material is unloaded back to its original null value of effective applied stress. As long as the material is unloaded above A_f, full reverse transformation will occur.

Actuation Path

The actuation path finds utility in applications where it is necessary to displace a component under an applied load. The full actuation path is the most utilized response path of the aerospace industry where a lightweight SMA component and thermal regulator have the potential to replace heavier, bulky actuators, as the SMA component has a high usable work energy density and requires almost no moving external parts. The heating portion of the path finds use in the petroleum industry and others, prominently for pipe couplings, as when the material is heated, it tightens around the pipes helping to form a proper seal even when condition extrema such as large temperature variation heavily influence pipe dimensions. The actuation loading path and material response are given in Figure 12 and Figure 13 respectively, and the steps of the path are described immediately following.

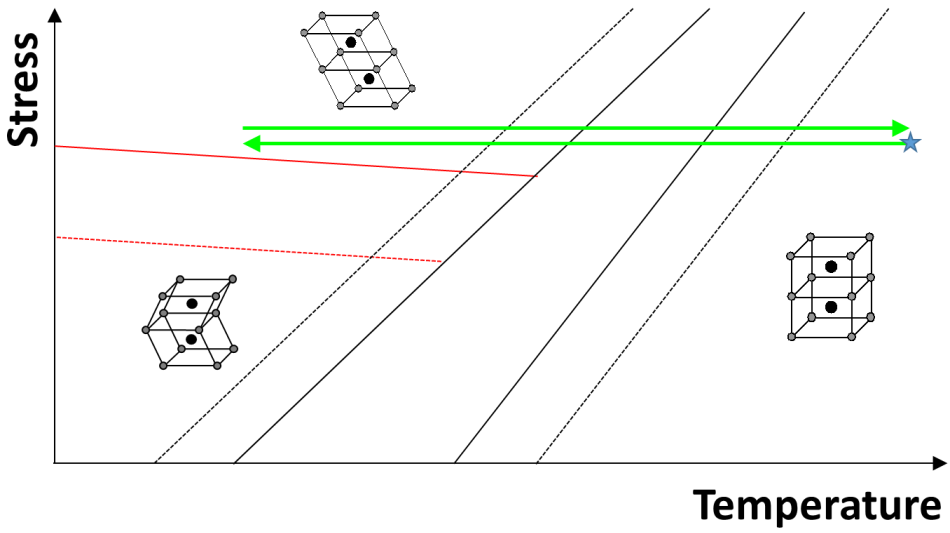

Figure 12. Actuation path in stress-temperature space

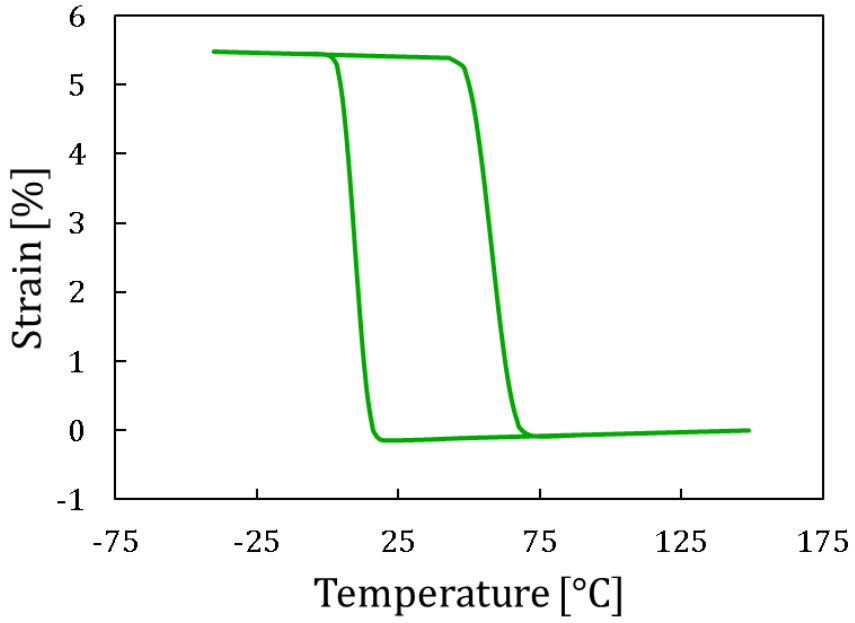

Figure 13. Modeled actuation response of a typical NiTi SMA

Step 1: Loading

Material is loaded above A_f under uniaxial tension at a constant temperature such that martensitic transformation does not yet occur.

Step 2: Cooling

While maintaining constant effective loading, the material is cooled, inducing phase change until full martensitic transformation occurs.

Step 3: Heating

The material is then heated back above A_f while maintaining a constant effective load such that full reverse transformation into austenite occurs.

Boundary Conditions

In solving RVEs (or mean-field equations), there are three typical boundary/loading conditions used: averaged displacement (Reuss), averaged traction (Voigt), and periodic (self-consistent). Specifically, uniform traction or uniform displacement loading conditions will give strict upper or lower bounds respectively for the average elastic properties of unbounded elastic materials with dilute distributions of particles, the derivation of which is given in multiple texts [63-65]. When applied to RVEs, they form relative bounds for material properties. A comparison of these three boundary conditions are given in Figure 14.

For the averaged traction or averaged displacement conditions in an RVE, the simulated microstructure does not need to be periodic to obtain a solution, but may require a very large domain size in order to converge to a solution which minimizes local fluctuation effects on the effective material response, and may not converge to an energetically optimal solution [66]. In the averaged displacement assumption, the prescribed displacement at the material boundary is a uniform value while the traction is allowed to vary. This will result in a response which is an over-approximation of the strain energy, and is near the termed Voigt upper bound.

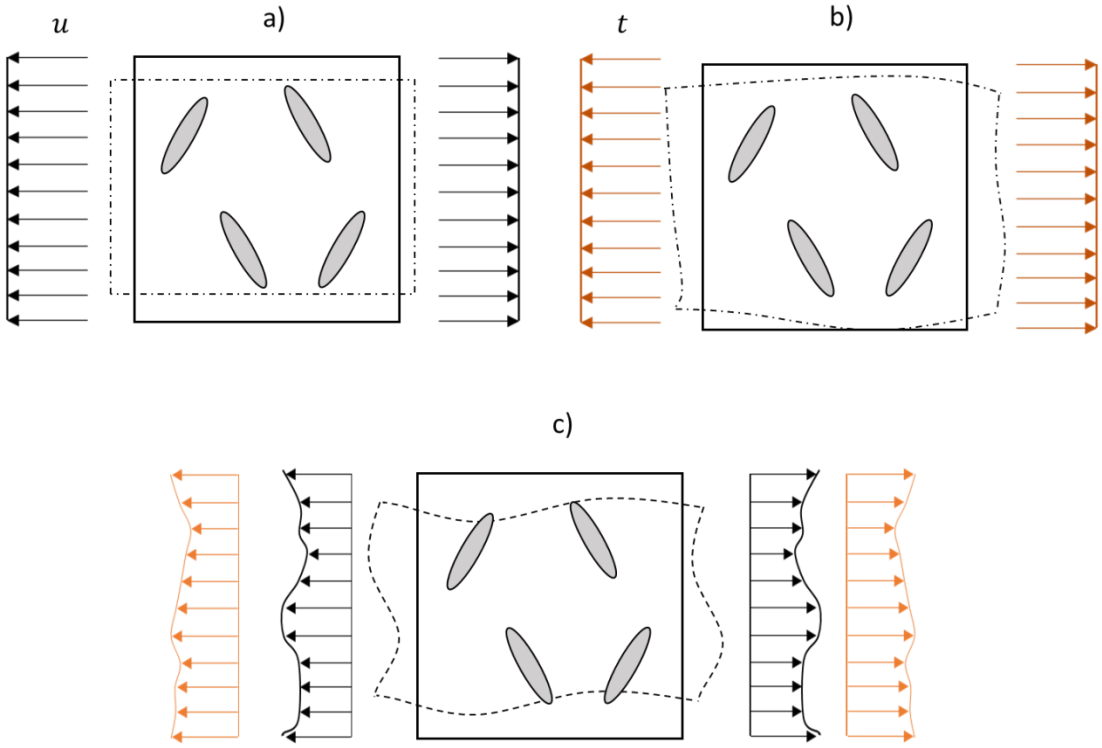

Figure 14. Common boundary conditions for uniaxial loading (displacements in black, tractions in orange). a) averaged displacement condition. b) averaged traction condition. c) periodic loading

In the averaged traction assumption, the prescribed traction at the material boundary is a uniform value while the displacement is allowed to vary. This will result in a response which is an under-approximation of the strain energy, near what is termed the Reuss lower bound of elastic properties. Then there are periodic conditions in which the boundary displacements and tractions are both allowed to vary with respect to the opposing boundary such that continuity in displacement and traction is maintained. This set of conditions will give the most appropriate approximation of the strain energy. For properly formulated periodicity, all aspects of the microstructure such as geometry,

tractions, displacements, and any features which affect material properties will be periodic on the external domain boundary. Having such periodicity will eliminate edge effects of the domain completely and result in an energetically accurate representation of the material response equivalent to a subdomain of an infinitely repeating domain. Such boundary conditions result in deformations of the domain such as the one shown in Figure 15 which demonstrates clear periodicity in deformed domain shape and Martensitic Volume Fraction (MVF) values, where if the material domain is patterned, such as in Figure 16, the idea of an infinitely repeating subdomain becomes clear.

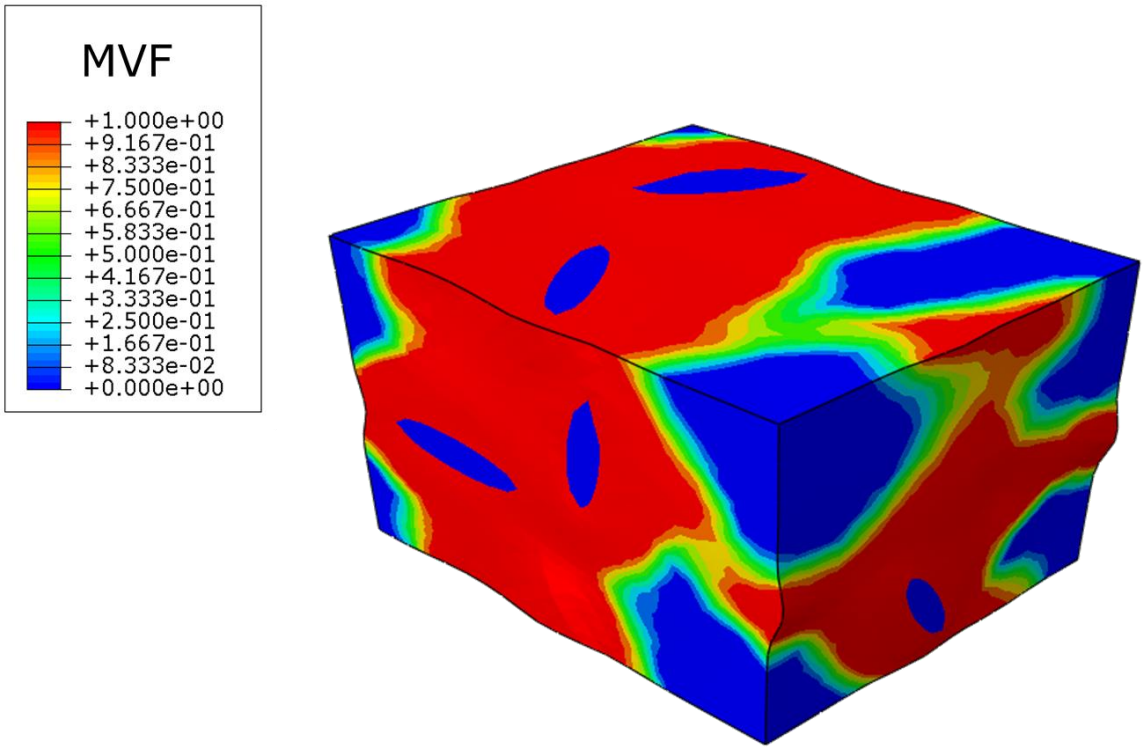

Figure 15. Example transforming RVE showing periodicity of deformation

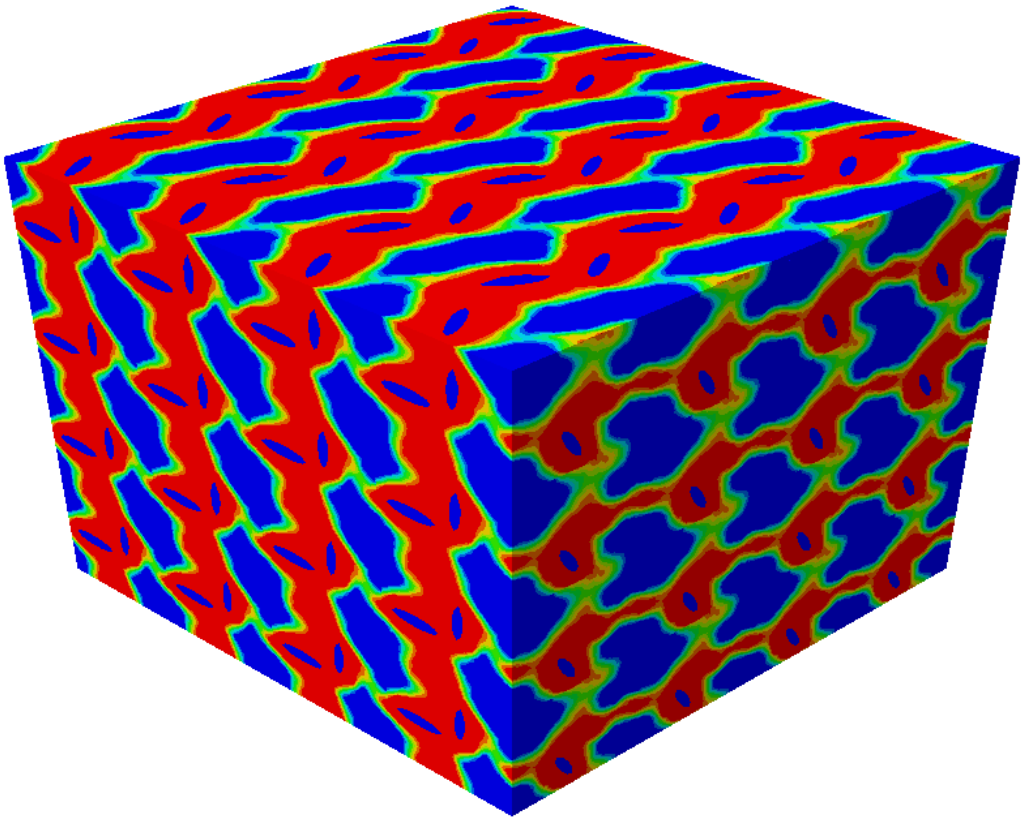

Figure 16. RVE linearly patterned in all dimensions demonstrates the periodicity in martensitic transformation

For simulations, the differences seen in estimated effective properties using any boundary conditions depends on the ratio of stiffness between particles and matrix. In general, if an analysis is conducted on a material whose components have elastic properties of values within the range of ~5:1 of each other, minimal variation of linear elastic response is seen using any set of boundary conditions. However, for non-linear elastic and inelastic responses, variance can increase dramatically for different internal particle configurations or boundary conditions. Since no FEA studies have previously

been conducted to compare boundary conditions on the response of SMAs, and their response is known to be highly non-linear, periodic conditions are used as they will result in the best approximation of the microstructural response. The equations for periodicity in mechanical conditions and diffusion are given as the following:

- Periodic mechanical boundary conditions

$$\begin{aligned} u(x_1,\, x_2,\, 0) - u_3 &= u(x_1,\, x_2,\, L), \\ u(x_1,\, 0,\, x_3) - u_2 &= u(x_1,\, L,\, x_3), \\ u(0,\, x_2,\, x_3) - u_1 &= u(L,\, x_2,\, x_3) \end{aligned} \tag{1.8}$$

- Periodic diffusion conditions

$$\begin{aligned} c_A(x_1, x_2, 0) &= c_A(x_1, x_2, L), \\ c_A(x_1, 0, x_3) &= c_A(x_1, L, x_3), \\ c_A(0, x_2, x_3) &= c_A(L, x_2, x_3) \end{aligned} \tag{1.9}$$

RVE Generation

For this work, we have chosen to employ an established method used to model a material's microstructural response, namely the solution of a representative volume element. The RVE is built with periodic geometries and solved under periodic boundary conditions as these are the most energetically appropriate for micromechanical simulations [67] and will result in the smallest necessary domain size to obtain a repeatable effective response. In our case, we have been able to use Abaqus to create RVEs which have periodicity in geometry and all considered features which affect

material response, namely chemical composition, traction, and displacement. The methods used to generate such RVEs, set them up for analysis, and extract their results are detailed out in the following sections.

Particle Placement

In order to build a domain with two constituents, some method for determining spatial arrangement of the constituents must be devised. In our RVEs, a Random Sequential Adsorption (RSA) algorithm [68] with considerations for periodicity has been used. The scripts utilize this placement method such that the end result is a cubic RVE domain with periodically embedded precipitates. The RVEs are of dimensions L×L×L, and contain a random dispersion of non-overlapping identical precipitates. The precipitates are assumed to have fully grown into the matrix and reached an equilibrium state, taking up their final observed volume fraction in the NiTi matrix, which is dependent on the heat-treatment conditions. They take the shape of oblate spheroids with a specified major-to-minor axis ratio, λ. Given a total precipitate volume fraction, v, and number of precipitates, N, the radius of the major ellipsoid axis, r, may be calculated as $r = L\,[v3\lambda/(4\pi\,N)]^{1/3}$. To place these precipitates, translation vectors and rotation angles are randomly generated for a new precipitate, and then geometries are tested for precipitate-precipitate overlap and precipitate-RVE domain intersection. If intersecting the RVE's external domain, precipitate geometries are copied to opposing sides of the RVE in order to maintain geometric continuity in linear translation. The new precipitate (or precipitate set) is accepted if the distance between its (their) surface(s) and all

previously generated precipitates is larger than a specified minimum distance. Enforcing such a minimum distance allows for an adequate finite element discretization of the space between neighboring inclusions, and also reflects experimental observation that particles have some small amount of separation. If any of these conditions are not met, new center translation vectors and rotation angles are generated, and the process is repeated. When the predetermined volume fraction of precipitates is reached, placement is stopped. The following flowchart in Figure 17 summarizes the particle placement, and a resulting 'spheroids in box' morphology is shown in Figure 18.

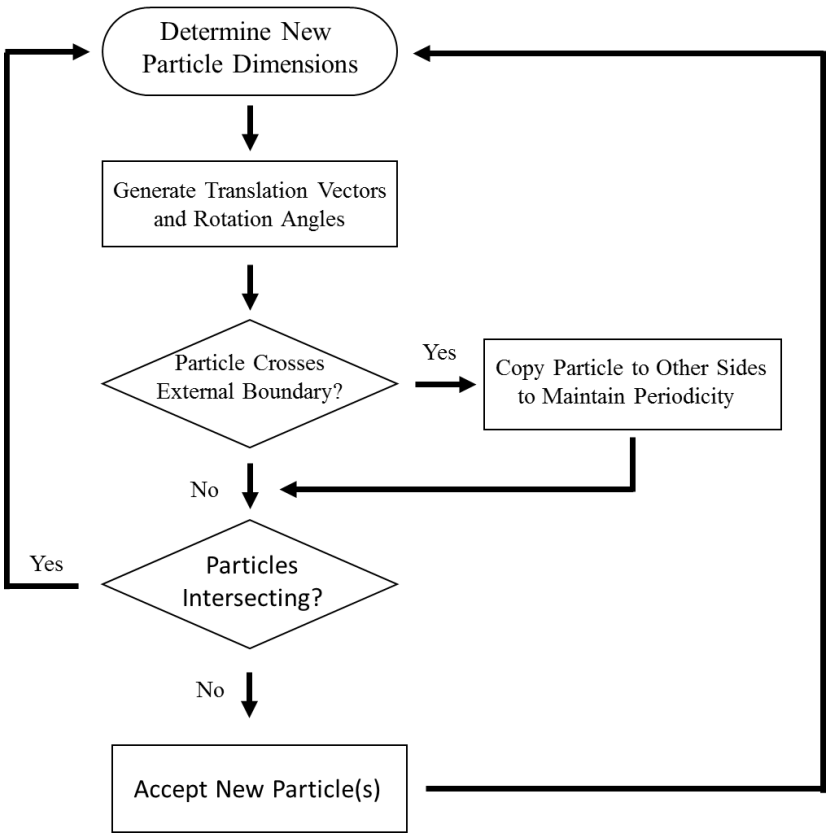

Figure 17. Flowchart of particle placement method

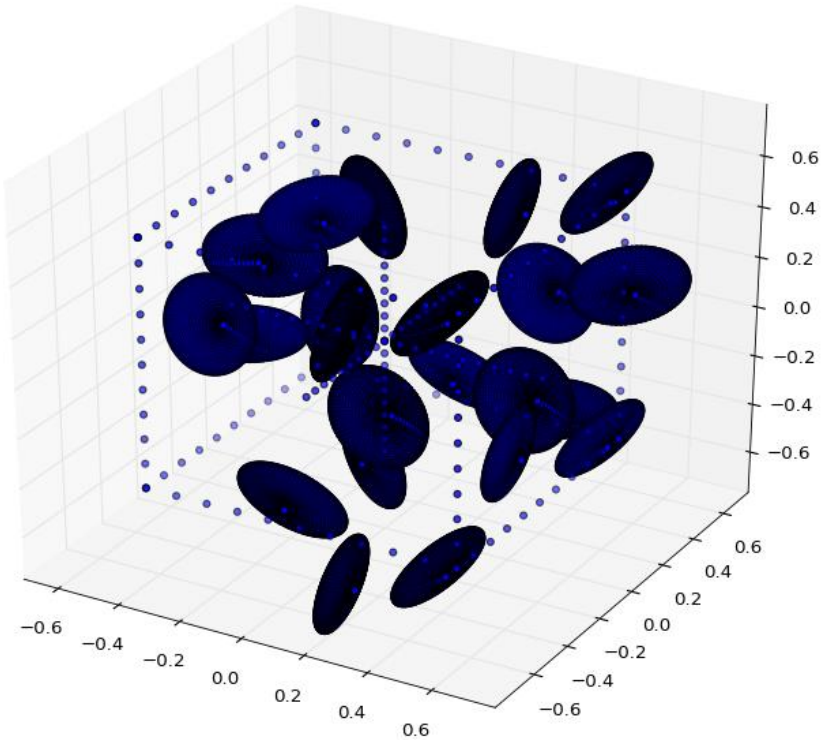

Figure 18. Image of a generated RVE with periodically placed particles

Abaqus Pre-processing

Once the RVE geometry is determined, it must be converted into finite elements and the simulations must be prepared. This part of the model setup is termed Abaqus pre-processing as it involves all steps which lead up to the prepared model aside from the already completed determination of RVE geometry. All of the steps following are done inside the Abaqus software package through the aid of its Python interface.

Pre-processing steps include:

1) Translation of the initial geometry data into Abaqus formatted data

2) Creation of a periodically bounded mesh for FE discretization

3) Application of periodic loading and BCs

4) Creation of geometry sets and element sets for use in post-processing

5) Assignment of material properties to the constituent phases of the microstructure

6) Assignment of particle orientations used for coherency calculations

7) Creation of model for coherency analysis

8) Creation of model for diffusion analysis

9) Creation of model for thermomechanical cycling analysis

10) Cleaning input files for job submission

It is of note that every aspect of the pre-processing is automated and that some of the features listed above have never been implemented to such extents in the Abaqus package as they are in the current work. Of primary interest is the newly developed ability to create a periodic microstructure with many non-spherical particles crossing external RVE boundaries while also having periodic loading and boundary conditions. The author has seen papers which, using Abaqus, have made 3D RVEs with periodic boundary conditions but no particles on the external boundaries, or RVEs with periodic boundary conditions and perfectly aligned or spherical particles crossing external boundaries [69], but no works which have the ability to include periodic boundary conditions with arbitrary particle shapes of arbitrary alignment which cross external boundaries. This is difficult to achieve primarily due to the fact that arbitrary geometries

are being sliced by RVE boundary, creating new complexly shaped particle domains which are difficult to discretize and mesh the exact same on opposing faces and edges.

For the assignment of periodic conditions, each node must be constrained with reference to its periodic positions on the cube. If the node is on a face, it must be constrained with reference to the same position on the opposing face. If on an edge, it must be constrained with respect to the same position on the other 3 edges sharing a common axis orientation. If on a corner, it must be constrained with respect to all other corners. This is demonstrated visually in Figure 19.

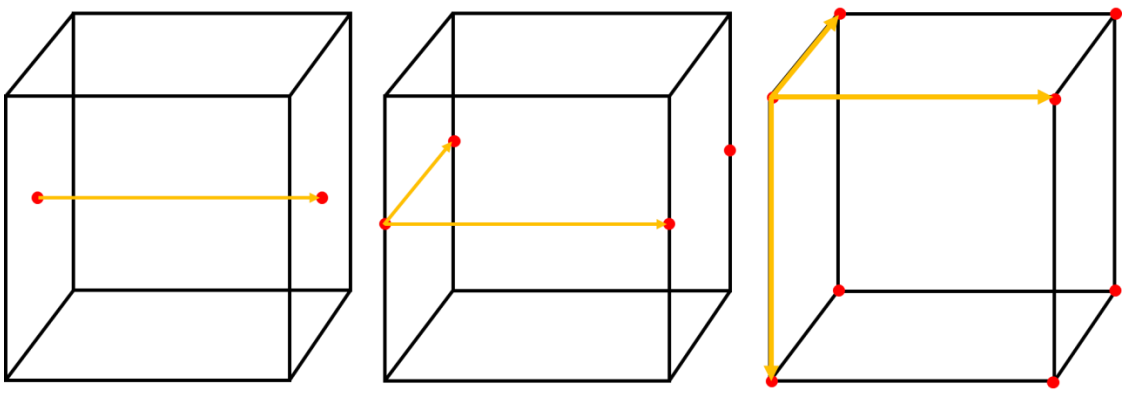

Figure 19. Periodic connectivity of nodes on a cubic domain boundary

There are two potentially available methods to ensure proper constraint of the nodes (constraint of a face node will be used as an example). The first is to have a non-periodic mesh which relates the node on one face to a weighted sum of the closest nodes on the opposing faces. There are some methods of this being implemented using polynomial interpolation [70], however, such methods are not included in commercially

available FE packages and require high order polynomials for accurate interpolation between nodes. The method which is able to be implemented in Abaqus requires an exact 1:1 correlation between nodal positions on opposing boundaries, necessitating that the mesh be exactly periodic on the external domain boundary. If the mesh is periodic, the equations can be formed with respect to each node's exact periodic partner(s). Methods which are utilized to create the proper MultiPoint Constraints (MPCs) in Abaqus are described by [71] where the constraint relations are reduced to a format which has constrained slaved node(s) following a single master node, following an external reference point designated in the assembly.

When creating particle sets, precipitate geometry is designed to be of arbitrary shape and number of subdomains, and the geometry cuts at the RVE boundary may clip any particle into a small piece potentially far away from the particle center. Therefore, particle centers cannot be used to find geometries later in preprocessing for orientation assignment. Therefore, it became necessary to devise a method which allows for the particle domains to be found and stored as sets in Abaqus. For this purpose a single point on each particle's surface which resides inside the RVE domain is stored during initial placement. An iterative searching algorithm is created and implemented to take the initial material point on the particle surface and iteratively find the adjacent geometric features of the particle. The specific process is as follows:

1. Given a point on the particle's surface, find its associated face.
2. Given a face, determine what cells it bounds.
3. Given the cells, determine all bounding faces of the cells.

4. Add new faces and cells to the set of particle geometry features
5. While new faces are found: Goto 2

This method is shown in Figure 20. Once all subdomains of the particle are found, a set is created for the particle. If the particle has periodic partners, all sets from periodic copies of particles are conglomerated into a single set. The final set is then assigned a material orientation for use in applying the directional eigenstrains inside the particles.

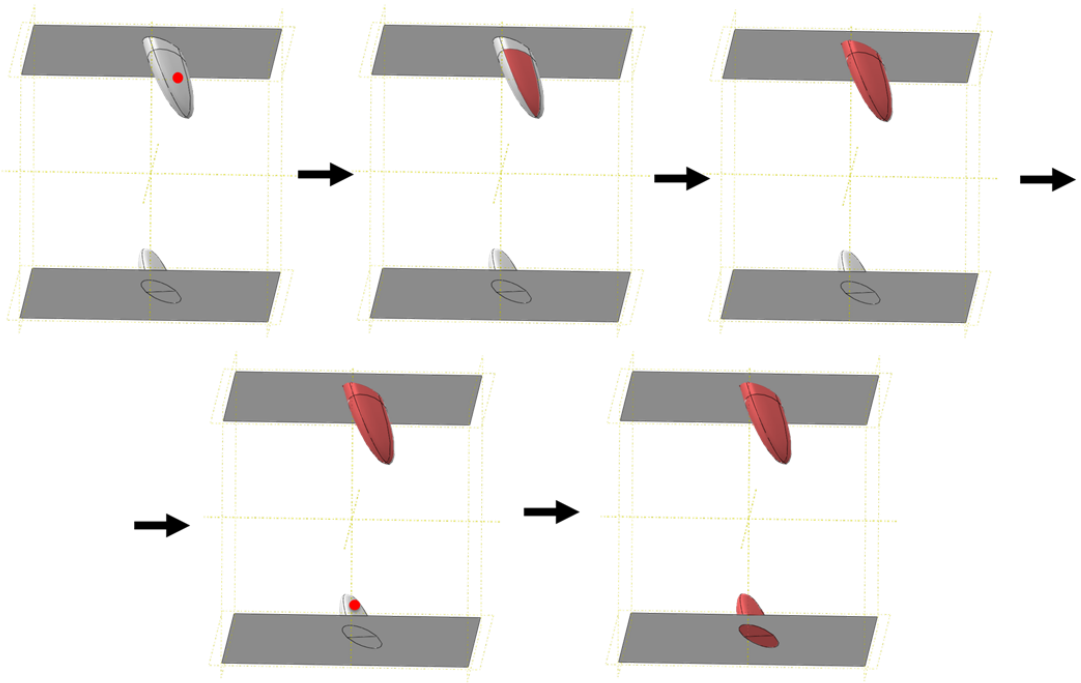

Figure 20. Iterative domain searching algorithm implementation

Numerical Implementation of RVE Model

The model takes into account the effects of many processes which change the microstructure during aging. Major features of precipitation were identified in the literature and included in the analysis models. These features are: the introduction of elastic precipitates, coherency of the precipitates in the matrix, and the diffusion of Ni to form the precipitates. This is in contrast to the works of [54, 55] which only take into account the introduction of elastic precipitates in a mean-field approach.

Constituent Phases of RVE

The precipitated Ni-rich NiTi SMA is viewed as a micro-scale composite comprised by thermoelastic non-transforming precipitates and a polycrystalline SMA matrix. Precipitated polycrystalline SMAs consist of a polycrystalline ensemble with random texturing and populations of ellipsoidal subgranular precipitates oriented in four different orientations with respect to the orientation of the crystal [72]. However, a point-wise representation of the Ni concentration fields surrounding distinct precipitates into a finite element polycrystalline ensemble requires a large RVE with a heavy computational burden. The high computational costs of such simulations inhibit extensive study of multiple realizations of the microstructure of such material systems to obtain accurate effective thermomechanical responses, and such polycrystalline averaging makes decoupling the texture and precipitate effects on the effective response difficult. Instead, in this work, a less computationally costly approach is adopted that allows for easier study of the effect of precipitates on the effective response. Namely, it

is assumed that the constitutive response of the matrix is representative of polycrystalline ensembles and incorporates the influence of the texture.

Constitutive Responses of Materials in RVE Domain

Two key assumptions are made to enable such an approach: (i) the precipitates are assumed to behave as linear elastic isotropic solids and (ii) the elastic and transformation constitutive behavior of the matrix material is assumed a priori isotropic as a result of random texture. To this end, material subvolumes (RVEs) containing randomly distributed non-overlapping precipitates are generated, which are assumed to have reached their equilibrium size, shape, and resulting volume fraction observed in experiments. The RVEs generated in the current work are comprised of two constituent phases: thermoelastic Ni_4Ti_3 precipitates and phase transforming SMA matrix. An exploded view of the phases is given in Figure 21.

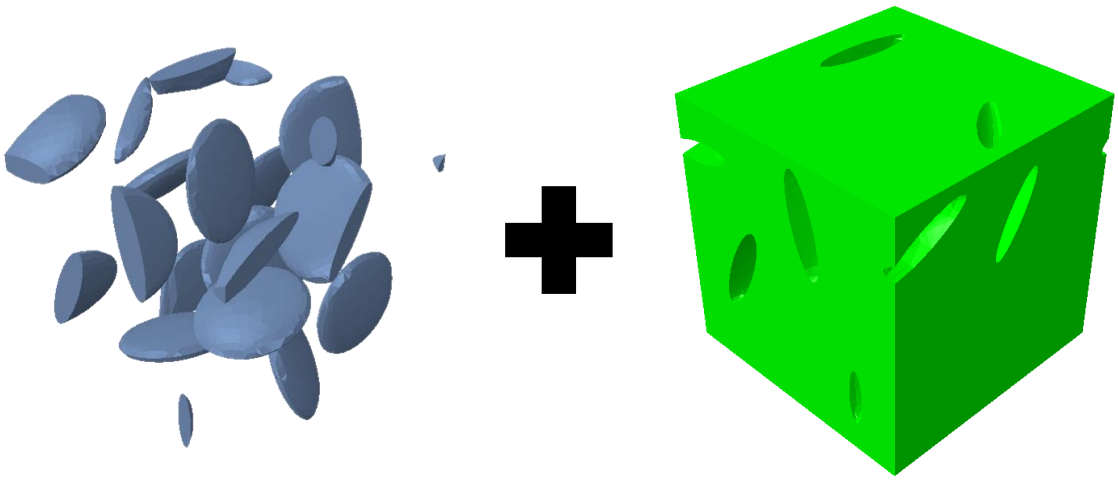

Figure 21. Exploded view of typical RVE domain constituents

The elastic properties of the precipitates are extracted from the first principle calculations of Wagner and Windl [2] and given as Young's modulus, $E_p = 107GPa$, and Poisson's ratio, $\nu_p = .39$. The aspect ratios of the precipitates are estimated from analysis using the phase field method [72].

The SMA matrix uses the Lagoudas et al. polycrystalline model for its constitutive response [29]. The constitutive laws have been implemented such that transformation temperatures are allowed to vary pointwise in the microstructure depending on the determined local Ni content computed from the diffusion analysis. The SMA constitutive model is formulated using rate-independent small-strain flow theory [29, 73, 74]. Increments in strain utilize additive decomposition, where the increment in the total strain tensor $d\varepsilon_{ij}$ may be broken down as

$$d\varepsilon_{ij} = S_{ijkl}d\sigma_{kl} + dS_{ijkl}\sigma_{kl} + d\varepsilon_{ij}^{t} + d\varepsilon_{ij}^{therm}$$

where σ_{ij}, ε_{ij}^{t}, and ε_{ij}^{therm} respectively represent the Cartesian components of the stress, transformation strain, and thermal strain tensors, and S_{ijkl} is the current compliance tensor. The current compliance is a function of the martensitic volume fraction ξ, and is computed as $S_{ijkl} = (1-\xi)S_{ijkl}^{A} + \xi S_{ijkl}^{M}$ where S_{ijkl}^{A} and S_{ijkl}^{M} are the compliance tensors of austenite and martensite in the polycrystalline material. The compliances of each of these tensors may be computed from the equation

$S_{ijkl}^{\alpha} = \frac{1-\nu_\alpha}{2E_\alpha}\left(\delta_{il}\delta_{jk} + \delta_{ik}\delta_{jl}\right) - \frac{\nu_\alpha}{E_\alpha}\delta_{ij}\delta_{kl}$ where the index α is replaced with A for the pure austenite phase or M for the pure martensite phase, E_α and ν_α represent the

Young's modulus and Poisson's ratio of the respective phases, and δ_{ij} is the Kronecker delta. The transformation strain evolves with the martensitic volume fraction ξ as

$$d\varepsilon_{ij}^{t} = \Lambda_{ij} d\xi,\ \Lambda_{ij} = \begin{cases} \Lambda_{ij}^{fwd},\ d\xi > 0 \\ \Lambda_{ij}^{rev},\ d\xi < 0 \end{cases} \tag{1.10}$$

where the components of the transformation direction tensor Λ_{ij} are defined as

$$\Lambda_{\mathrm{ij}}^{fwd} = \frac{3}{2} H^{cur} \frac{\sigma_{ij}^{'}}{\bar{\sigma}},\quad \Lambda_{ij}^{rev} = \frac{\varepsilon_{ij}^{t}}{\xi}\ . \tag{1.11}$$

The forward transformation direction tensor is dependent on H^{cur}, the uniaxial transformation strain magnitude of full transformation, σ_{ij}', the deviatoric stress tensor, and $\bar{\sigma}$, the von Mises effective stress defined as $\bar{\sigma} = \sqrt{\frac{3}{2}\sigma' : \sigma'}$. Therefore, it is seen that the forward generated strain is developed in the direction of the applied stress. As there may be a mixture of twinned and detwinned martensite in the material depending on the ability of the stress to detwin the martensite, H^{cur} is defined as a decaying exponential function of the applied load and given as

$$H^{cur}\left(\bar{\sigma}\right) = \begin{cases} H_{min}; & \bar{\sigma} \le \bar{\sigma}_{crit} \\ H_{min} + \left(H_{sat} - H_{min}\right)\left(1 - e^{-k(\bar{\sigma} - \bar{\sigma}_{crit})}\right); & \bar{\sigma} > \bar{\sigma}_{crit} \end{cases} \tag{1.12}$$

where H_{min} gives the transformation strain attained when no external loads are applied to the material, H_{sat} is the maximum potentially attainable transformation strain under uniaxial loading, and $\bar{\sigma}_{crit}$ is the minimum equivalent stress required to generate transformation strains higher than H_{min}. The k parameter alters the shape of the curve relating applied stress and attained transformation strain, denoting how steeply H_{cur} will

increase as the stress is increased, giving a steep increase for higher k values and shallow increase for lower k values. During reverse transformation, the transformation strain recovery is assumed governed by the orientation and magnitude of martensite at the beginning of reversal normalized by the volume fraction of martensite. This allows the complete recovery of generated transformation strains resulting in a null valued tensor at the end of full reverse transformation.

During transformation, the thermodynamic driving forces π^t must balance the critical thermodynamic driving force required for transformation, Y^t. This balance is termed the transformation yield surface Φ^t which has the condition that during transformation, there should be maximum dissipation, analogous to J_2 plasticity theory, such that $\Phi^t_{fwd} = \pi^t_{fwd} - Y^t_{fwd} = 0$ and $\Phi^t_{rev} = -\pi^t_{rev} - Y^t_{rev} = 0$, ie. the stresses must remain on the yield surface during transformation. The thermodynamic driving force is written as

$$\pi^{fwd} = \sigma_{ij}\Lambda^{fwd}_{ij} + \frac{1}{2}\Delta S_{ijkl}\sigma_{ij}\sigma_{kl} + \sigma_{ij}\Delta\alpha\left(\mathrm{T}-\mathrm{T}_0\right) + \rho\Delta s_0 T - \rho\Delta u_0 - f^{fwd} \qquad (1.13)$$

for forward transformation, and

$$\pi^{rev} = \sigma_{ij}\Lambda^{rev}_{ij} + \frac{1}{2}\Delta S_{ijkl}\sigma_{ij}\sigma_{kl} + \sigma_{ij}\Delta\alpha\left(\mathrm{T}-\mathrm{T}_0\right) + \rho\Delta s_0 T - \rho\Delta u_0 - f^{rev} \qquad (1.14)$$

For reverse transformation where f^{fwd} and f^{rev} are functions describing the behavior of transformation hardening during forward and reverse transformation respectively. s_0 is specific entropy, u_0 represents internal energy, ρ is density, and Δ denotes difference in phase properties. The gradual transition seen in the polycrystalline response of a typical

SMA is represented in the hardening functions f^{fwd} and f^{rev} by giving them as a general power law form:

$$f^{fwd}(\xi) = \frac{1}{2}a_1\left[1+\xi^{n_1}-(1-\xi)^{n_2}\right]+a_3$$
$$f^{rev}(\xi) = \frac{1}{2}a_2\left[1+\xi^{n_3}-(1-\xi)^{n_4}\right]-a_3 \quad (1.15)$$

where a_i $(i = 1,2,3)$ are coefficients that assume real values, and n_i $(i = 1,2,3)$ are exponents which assume real numbers $0 < n_i \leq 1$.

The constitutive relations necessitate calibration of: (i) thermoelastic parameters for austenite and martensite phases, (ii) parameters which make up the $H^{cur}(\sigma)$ function, and (iii) model parameters describing the phase transformation $(\rho\Delta s_0, \rho\Delta u_0, a_1, a_2, a_3, Y_0)$. The material properties that are used to calibrate the model are broken down by category below:

(i) $E_A, E_M, \nu_A, \nu_M, \alpha_M, \alpha_A$

(ii) $H_{min}, H_{sat}, \bar{\sigma}_{crit}, k$

(iii) $M_s, M_f, A_s, A_f, C_M, C_A, n_1, n_2, n_3, n_4$

M_s, M_f, A_s and A_f are respectively the martensitic-start, martensitic-finish, austenitic-start, and austenitic-finish temperatures at zero load, C_M and C_A are the forward and reverse transformation slopes on the stress-temperature phase diagram and $n_1 \ldots n_4$ are smoothening coefficients. The elastic constants can be calculated directly from nominally isothermal stress-strain curves in each phase where loads are applied at temperatures such that the material does not undergo phase transformation. The thermal expansion coefficients may be obtained by applying a load and changing the temperature

in each individual phase (such that it does not transform), measuring the change in thermoelastic strain. The parameters for $H^{cur}(\bar{\sigma})$ can be calibrated directly from material testing under thermal variations at a constant applied load (ie. actuation cycles) where the value of k in particular is chosen to best fit the experimental trend. The remaining six parameters are calibrated by considering the conditions under which forward transformation begins and ends in the stress–temperature space [74]. The hardening coefficients $n_1 \ldots n_4$ do not have a directly associated material property but are chosen to best fit the smooth behavior of the transformation hysteresis plots.

Coherency Between Particles and Matrix

Eigenstrains, $\varepsilon_{ij}^{Ni_4Ti_3}$, are incorporated into ellipsoidal precipitates corresponding to the lattice mismatch between the precipitates and austenitic matrix phase in order to develop the coherency stress and strain fields. These eigenstrains are introduced by assuming an additive decomposition of strains into elastic and stress-free strains of the form $\varepsilon_{ij}^{Ni_4Ti_3}\Delta t$, where Δt is a parameter that changes in the numerical calculations from its initial value 0 to its final value 1. The eigenstrains corresponding to the lattice mismatch between the precipitates and austenitic phase imposed into the precipitates are given as

$$\varepsilon_{ij}^{Ni_4Ti_3} = \begin{bmatrix} -0.00417 & 0 & 0 \\ 0 & -0.00417 & 0 \\ 0 & 0 & -0.0257 \end{bmatrix} \tag{1.16}$$

with respect to local precipitate coordinate systems (x_1', x_2', x_3'), taken such that their origins are located at the center of the precipitates, where the coordinate axis x_3' is extending along the direction of the minor axis, and x_1' and x_2' lie in the plane perpendicular to x_3' as shown in Figure 22. The values of the eigenstrains are determined using experimental data on the lattice constants of the austenitic-B2 and Ni_4Ti_3-rhombohedral unit cells. The initial shape and volume fraction of the precipitates is such that the precipitates assume their observed shape and volume fraction at the end of the simulation process, in which periodic boundary conditions are used,

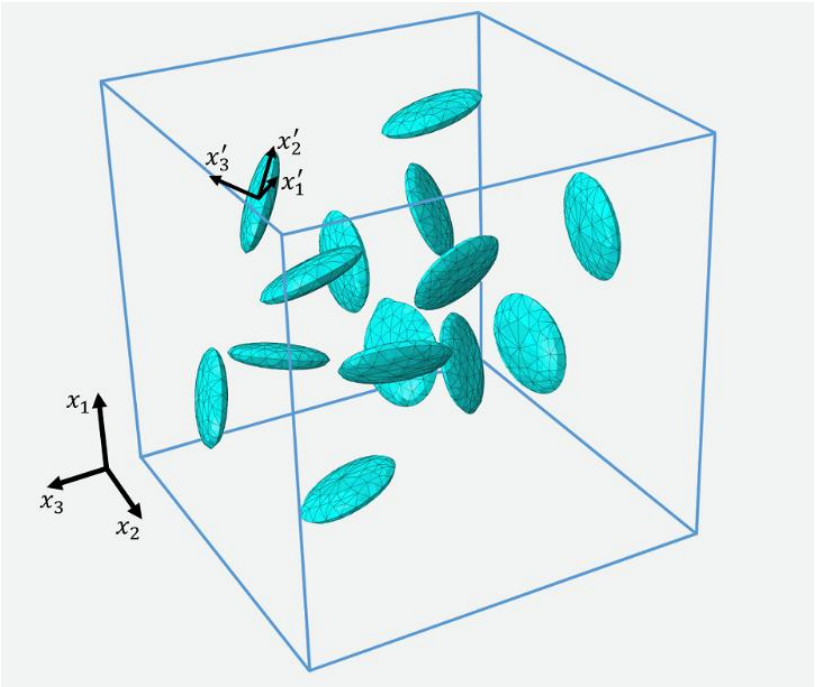

Figure 22. Ellipsoids in RVE showing global (x) and local (x') coordinate systems

$$u(x_1, x_2, 0) - u_3 = u(x_1, x_2, L),$$
$$u(x_1, 0, x_3) - u_2 = u(x_1, L, x_3),$$
$$u(0, x_2, x_3) - u_1 = u(L, x_2, x_3),$$

where u stands for the displacement vector on the different RVE faces and the vectors u_3, u_2 and u_1 depend on the loading applied to the cell, i.e., on the eigenstrains introduced to the precipitates. These conditions are applied using a modified version of an Abaqus plug-in [75] which takes a periodic mesh, and given the two faces to be paired as well as the vector of periodicity, creates appropriate equation constraints in Abaqus for each minimally interdependent set of nodes in the manner described in [71].

Diffusion of Ni in the Matrix

The strong impact of Ni content on the phase transition temperatures is captured by (i) using Fick's approximation to describe the Ni depletion from the matrix during the precipitation process and (ii) translating the resulting Ni concentration distribution to a phase transition temperature distribution in accordance with experimental results for unprecipitated material systems [4].

The average Ni concentration c in the RVE is computed from the equation

$$c = vc_{Ni_4Ti_3} + (1-v)\,c_A \tag{1.17}$$

where $c_{Ni_4Ti_3}$ and c_A represent the Ni concentrations of the precipitates and austenitic matrix, respectively. Since $c_{Ni_4Ti_3}$ is constant, only diffusion in the austenitic matrix needs to be considered. Initially, the matrix material is set to the homogeneous

concentration before precipitation, and the development of the Ni concentration field is simulated using Fick's approximation

$$\dot{c}_A = D_A \nabla^2 c_A \tag{1.18}$$

where the dot denotes differentiation with respect to time and D_A is the temperature-dependent diffusivity coefficient.

Periodic boundary conditions are used on the RVE faces in solving the diffusion equation as well

$$\begin{aligned} c_A(x_1, x_2, 0) &= c_A(x_1, x_2, L), \\ c_A(x_1, 0, x_3) &= c_A(x_1, L, x_3), \\ c_A(0, x_2, x_3) &= c_A(L, x_2, x_3), \end{aligned}$$

which are generated in similar manner to the mechanical periodicity.

The Ni concentration in the precipitates is given as $c_{Ni_4Ti_3} = 56.8\ at.\%$, and the equilibrium Ni concentration used for precipitate boundary conditions in the matrix is estimated at $50.1\ at.\%$, ($50.4\ at.\%$ for later work in Chapter IV), while the diffusivity coefficient is given as $D_A = 1.085x10^{-15} m^2 s^{-1}$. Once the Ni content distribution in the matrix is evaluated, phase transition temperatures are individually assigned to each integration point in the matrix by using a polynomial least square fit of the experimental data in Table 1 relating the Ni content in unprecipitated NiTi material systems to phase transition temperatures.

Table 1. Tabulated transformation parameters as a function of average Ni content, given in [4]

c_{Ni}	M_s(K)	M_f(K)	A_s(K)	A_f(K)
49.99	338.7	311.7	352.1	380.2
50.19	325.8	296.1	337.1	365.8
50.39	302.1	275.9	319.4	339.3
50.59	290.2	263.4	302.0	324.6
50.80	272.1	245.3	284.2	308.3
50.86	266.0	237.9	277.9	301.3
51.00	246.1	222.4	245.5	268.0
51.10	226.9	207.5	240.9	254.0
51.21	210.9	181.4	226.4	242.0

Thermomechanical Cycling

The macroscopic actuation and pseudoelastic response are obtained by subjecting the RVEs to their respective loading paths: a thermal cycle under constant uniaxial tensile load and a loading–unloading cycle at constant nominal temperature (see Figure 5). In the former, the diffused material with coherent precipitates is loaded uniaxially to a predetermined level and subsequently thermally cycled to induce forward and reverse phase transformation, from austenite to martensite and back, in order to obtain its actuation response. The latter path corresponds to the material being loaded uniaxially at a nominally constant temperature until it transforms to martensite. Subsequent unloading induces reverse phase transformation back to austenite. Such a cycle is shown in Figure 23.

Periodic boundary conditions are applied in all cases by equation constraints in Abaqus, as is done for the finite element calculations determining the coherency stress and Ni concentration fields.

The effective response of the RVEs is presented in terms of the volume average stress and total strain over the RVE, defined respectively as

$$\Sigma_{ij} = \frac{1}{\Omega}\int_{\Omega}\sigma_{ij}dV,\ \mathrm{E_{ij}} = \frac{1}{\Omega}\int_{\Omega}\varepsilon_{ij}dV \tag{1.19}$$

where σ_{ij} and ε_{ij} are the Cartesian components of the stress and strain. Note that the effective elastic and transformation strains are not necessarily the volume averages of the corresponding local strains. In the calculations, these strains are resolved from the boundary displacements that correspond to the volume average of the total strains.

A standard RVE is discretized with ~50,000 quadratic 10 node tetrahedral elements with integration at four Gauss points and hourglass control (C3D10MT in [76]). This tetrahedron exhibits minimal volumetric locking during transformation and captures strain gradients in the matrix better than the standard 10-node tetrahedron due to its three extra internal degrees of freedom. The high-performance computing cluster EOS at Texas A&M University was used to run the majority of the simulations. The appropriateness of the simulations' mesh density was checked by discretizing one model using ~150,000 elements and comparing the overall strain–temperature response with the one obtained with the standard discretization.

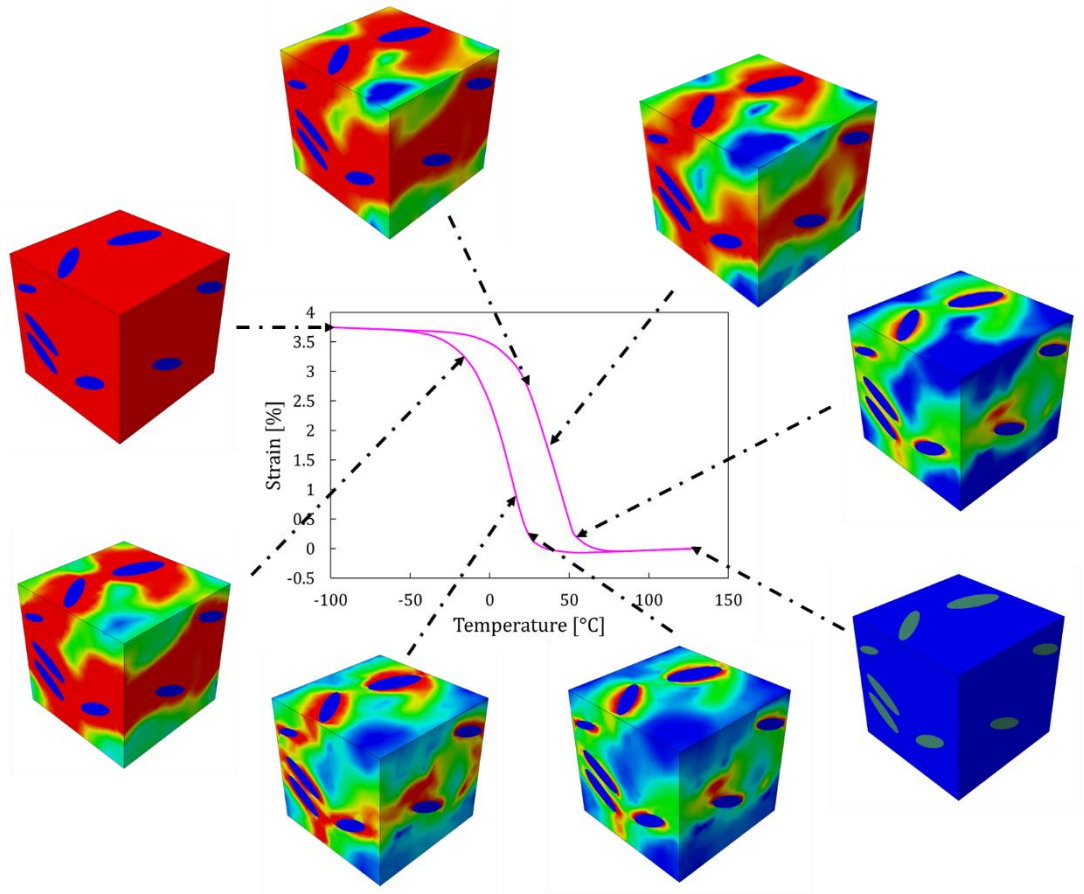

Figure 23. Martensite volume fraction through an actuation cycle in an RVE. Red denotes martensite, blue denotes austenite

Summary

This chapter has introduced the problem formulation including the boundary value problem, constitutive relations, and conservation laws. It also has discussed the modeling framework used to conduct an analysis, including the methods used for the setup of a finite element analysis, description of the generation of an RVE, computation of the coherency stress field and Ni distribution and running of a thermomechanical analysis. It also describes the applied periodic boundary conditions and gives the

required pre-processing steps necessary to set up an analysis as well as an introduction to the thermomechanical paths considered in an analysis.

CHAPTER III

EFFECTS OF MICROSTRUCTURAL CHARACTERISTICS ON THE MACROSCOPIC THERMOMECHANICAL BEHAVIOR OF PRECIPITATED SMAS*

In this chapter, the specific behavior of precipitated, Ni-rich NiTi shape memory alloys, i.e., thermal actuation under stress and pseudoelasticity, are investigated via the finite element method. The deformation response of the material-at-large is simulated using an RVE, taking into account the structural effect of the precipitates, as well as the effect of the Ni concentration gradient in the matrix. The obtained results reproduce and provide important insight into several of the experimentally observed precipitation-induced changes on the transformation characteristics of these materials. It is assumed that the heating-cooling and loading rates are sufficiently slow to justify the assumption of constant temperature throughout the RVE [77, 78] and rate-independent behavior of the constitutive model. Moreover, the deformation response of the RVEs is used to calibrate an existing rate-independent constitutive SMA model, similar to the one employed to describe the matrix behavior, and the computed effective material parameters are compared with those of the matrix. The obtained results reproduce several of the experimentally observed precipitation-induced changes on the maximum transformation strain, phase transition temperatures, and transition from the elastic to

*Portions of this chapter are reprinted with permission from "Micromechanics of precipitated near-equiatomic Ni-rich NiTi shape memory alloys" by Baxevanis, T., Cox, A., and Lagoudas, D.C., 2014, Acta Mechanica. doi: 10.1007/s00707-013-1071-3.

transformation response and vice versa.

Analysis Setup

A brief explanation of the solutionized calibration and method for determination of final average Ni content after precipitation is given in this section.

Solutionized Material Calibration

For this study, many RVEs are built and solved in order to determine general trends and changes to the SMA response due to a number of factors. In order to simulate the SMA material, some reference properties in the form of a calibration of homogeneous solutionized material before precipitation are given. To this extent, thermomechanical parameters of a solutionized material are determined and used as inputs for the model. The material used for calibration has an initial composition of approximately 50.8 at.%Ni and the estimated thermomechanical properties of that listed in Table 2 below.

Table 2. Material parameters used for the SMA matrix

Parameter	Value	Parameter	Value
E_A [GPa]	50	H_{sat}	0.029
E_M [GPa]	23.8	k [MPa^{-1}]	∞
$\nu_A = \nu_M$	0.33	C_A [MPa K^{-1}]	7.0
		C_M [MPa K^{-1}]	7.0
		$n_1 = n_2 = n_3 = n_4$	1

Determination of Target Final Average Ni Content

As the Ni profile of the matrix is estimated using a Fickian diffusion equation, requiring boundary conditions for the precipitate surface, the diffusion process must be stopped at a certain time since if it were left running, it would equilibrate to the given boundary condition of Ni content. Therefore, the simulation is stopped once it reaches a specified volume average Ni content in the matrix, such that mass balance is maintained between the added precipitates and removed Ni in the matrix. This volume average value is determined using (1.17) which is repeated below

$$c = vc_{Ni_4Ti_3} + (1 - v)c_A$$

where the homogenized concentration is given as c, the volume fraction of precipitates is given as v, and the final average concentration is given as c_A.

A thermodynamically consistent constitutive law is used to model the matrix with transformation transition temperatures assigned to every integration point with respect to the results of the Ni depletion process. The constructed RVEs are then subjected to thermal cycles under constant load and loading-unloading cycles at constant nominal temperatures to examine the effects of precipitates on the effective actuation and pseudoelastic response of precipitated Ni rich NiTi SMAs.

Effect of Coherency Between Particles and SMA Matrix

The coherency stress field in an RVE with 3% precipitate volume fraction, resulting from the introduction of the eigenstrains given in (1.16) into the precipitates, is shown in Figure 24. All RVE figures in this chapter show a section cut of the inside of

the cube for illustration purposes as the framework at the time which the studies were conducted did not have the capability for the particles to cross external domain boundaries. Note that the values of the von Mises stress get as high as 350MPa adjacent to the precipitates.

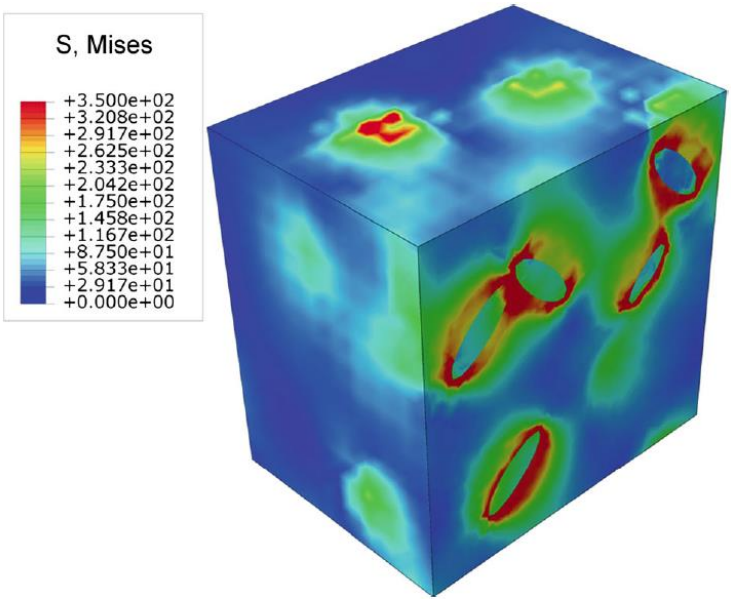

Figure 24. Computed coherency stresses in an RVE

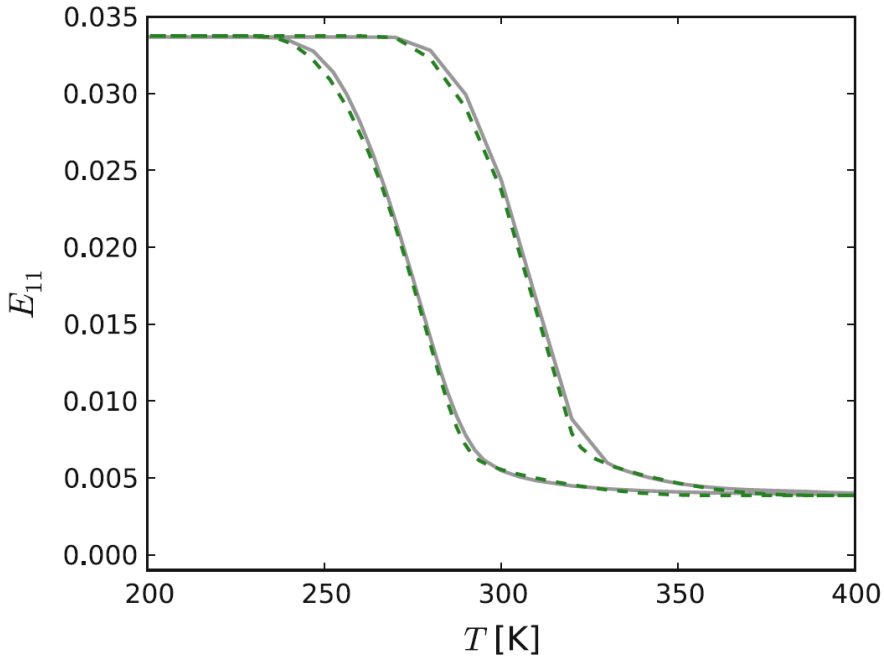

Figure 25. Comparison of uniaxial RVE response with and without coherency stresses

Comparison of the effective strain in the direction of loading versus temperature responses of 3% volume fraction precipitated material with (solid line) and without (dashed line) the coherency stress field accounted for under a constant uniaxial stress of 200MPa is given in Figure 25. Although the values of coherency stress are as high as 350MPa, resulting locally in a shift of the phase transition temperatures up to 50K ($C_M = C_A = 7$ in Figure 25), little difference is noted in the effective macroscopic response with their presence. Thus, although locally significant, the coherency stresses are only marginally important macroscopically in materials of similar volume fractions.

Effect of Diffuse Ni Content in the Microstructure

In Figure 26, the Ni concentration profile for the same RVE is shown. Although the variation of Ni concentration in the matrix caused by the presence of precipitates is relatively small, it may have a significant effect on the martensitic transformations, since a 0.1 at.% difference in Ni of Ni-rich NiTi alloys can lead up to a 20K change in the phase transition temperatures, M_s, M_f, A_s, and A_f as seen in Table 1. Above 50 at.%Ni, the phase transition temperatures fall down drastically with increasing Ni content. Under 50 at.%Ni, there is no relation between Ni concentration and phase transformation temperatures, and constant values of these temperatures are observed. A comparison between the Ni concentration surrounding a single precipitate and experimental measurements reported in [79] is presented in Figure 27. These concentration values are obtained by taking a precipitate relatively away from the others and measuring the Ni content radially outward along the minor axis of the ellipsoid. It is seen that although simplifications were made for simulating the diffusion process, including the calculation of Ni concentration without accounting for sub-granular anisotropy and specific particle orientations, the simulated results are in reasonable agreement with the experimental ones. The phase transformation temperature distributions of an RVE are presented in Figure 28. They result from assignment of phase transformation temperatures to each integration point in the matrix using a least square fit of the experimental data in Table 1.

.

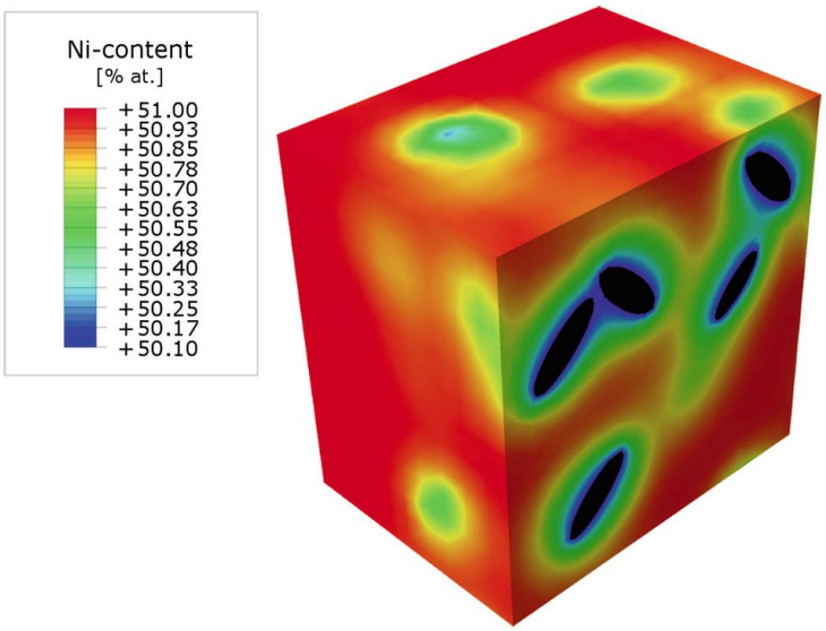

Figure 26. Ni profile in an RVE after Fickian diffusion

To identify the significance of the heterogeneous Ni profile, simulations are performed on the same RVE in which separate studies incorporate either a uniform or diffuse Ni profile. For the uniform case, the matrix volume average Ni concentration is computed and assigned to all corresponding material. In this way, the two cases presented in Figure 29 with a homogeneous and a heterogeneous Ni profile have the same total Ni concentration. Comparing these responses demonstrates that the diffuse profile produces a more gradual transition from elastic to transformation response and a smaller maximum transformation strain. These differences will become more pronounced as the precipitate volume fraction increases.

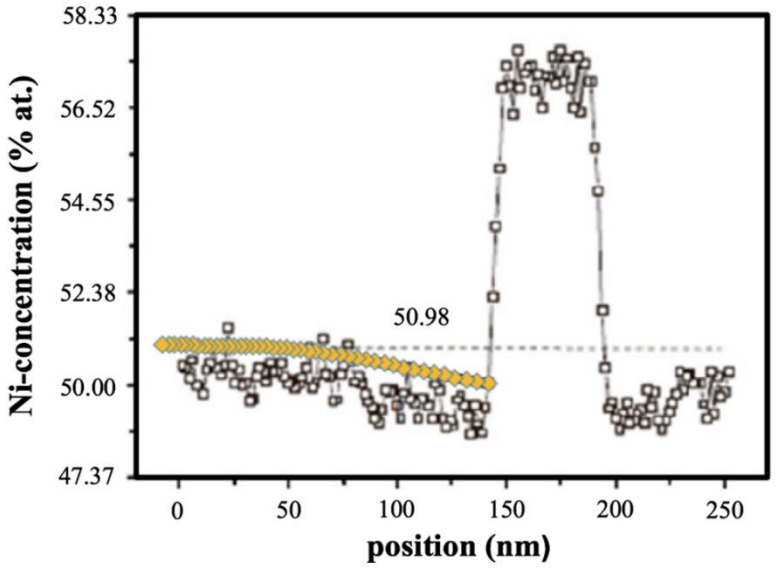

Figure 27. Comparison of computed and measured Ni composition approaching a precipitate

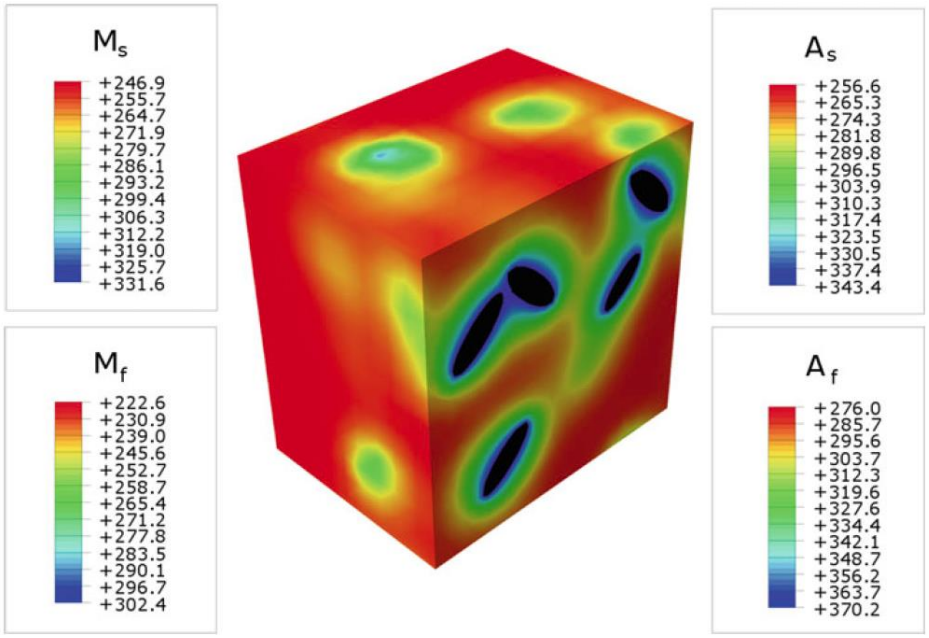

Figure 28. Computed transformation temperature distribution

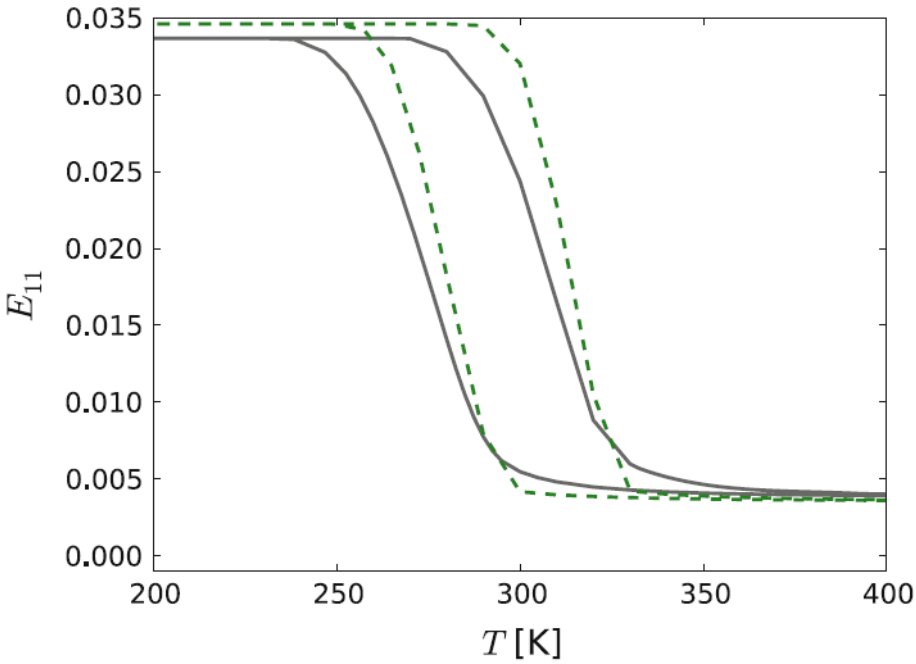

Figure 29. Comparison of computed RVE response with diffused (solid black line) and averaged Ni profiles (dashed green line)

Accuracy of Numerical Calculations

In an RVE, it is assumed that the representative domain which is modeled is large enough that using equivalent placement metrics, other generated realizations of the microstructure will have the same effective response, and if the domain size is increased, the response will not change. The necessary domain size required to accurately model a microstructure will be dependent on the ratio of the particle and matrix stiffnesses, where consideration of difference in elastic properties of the phases is well documented [67, 80] and below a 5:1 ratio, generally only small differences in effective properties are seen for elastic and elasto-plastic materials of configurations under periodic boundary conditions. Kanit et al. [67] showed that the effective physical properties of a heterogeneous material can be determined either by a few number of measurements on

large RVE volumes (large number of particles for a given volume fraction) or by many realizations for small volumes of material. They also show that the number of realizations needed for a given RVE volume is less for periodic boundary conditions than for homogeneous stress or strain boundary conditions. However, the mean values computed on smaller RVE domains may not accurately represent the effective response for the composite material even when using periodic boundary conditions and a sufficient number of realizations. These studies give insight into effective elastic and elasto-plastic response dependence on particle to domain size and properties, however, as SMA materials can have sharp transitions in which effective elastic properties may drastically change, and the current study considers diffuse properties in the matrix, a study is conducted to confirm accuracy of computed effective RVE properties.

The accuracy of the numerical simulations is checked by generating RVEs and examining their actuation response for different dispersions of the precipitates in each case. Three microstructural particle dispersions are created for each of three numbers of particles: 12, 15, and 18. The effective response of the three in each category are averaged and variation from the average in each category is quantified (Figure 30). The maximum relative difference in strain for a given temperature between different realizations of the microstructure is 7.12% for 12 precipitates, 6.81% for 15 precipitates, and 6.24% for 18 precipitates, while the maximum difference between the average values resulting from microstructures with different number of particles is less than 4%. Since the material behavior considered is highly nonlinear, and a slight shift in transformation start and finish temperatures gives high differences in strain values near

the beginning and end of transformation, the energy dissipated during thermal cycling is used as a method of comparison as well. Using this parameter, it is found that the maximum difference between the dissipated energy of any individual RVE simulation in one of the particle count categories and the average dissipated energy of three different dispersions in the respective category is less than 0.75% of the latter for the case of 12 precipitates, 0.55% for 15 precipitates, and 0.18% for 18 precipitates. Based on these results, the average response of microstructures obtained from 3 different dispersions of 15 precipitates is considered as representative of the material-at-large.

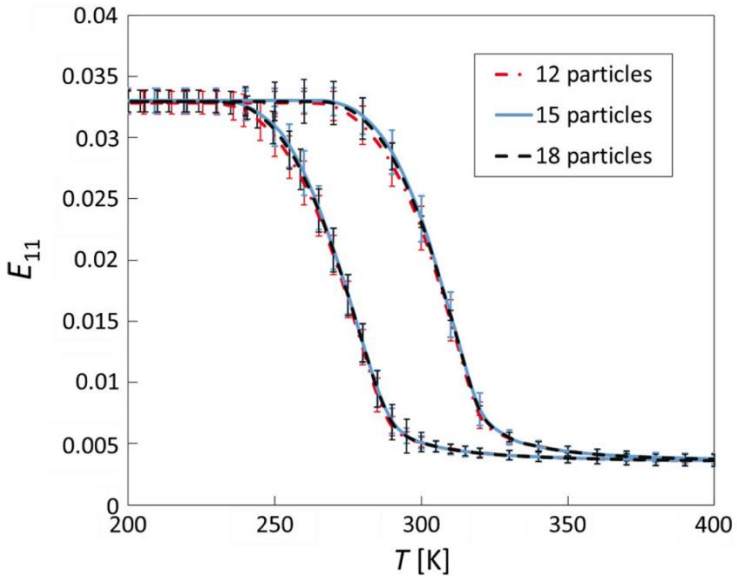

Figure 30. Variation in effective RVE responses between realizations for increasing number of particles

Effects of Precipitate Volume Fraction on Macroscopic Response

For an isobaric response, the martensite volume fraction and von Mises effective stress field during forward transformation (cooling) under a constant uniaxial load of 200MPa are shown in Figure 31. The heterogeneity of transformation and stress is clearly visible in these figures. Microstructural stress concentrations and low levels of Ni content around precipitates lead to formation of martensite earlier than in matrix regions away from precipitates (Figure 31a). Martensitic regions first grow in between Ni_4Ti_3 precipitates before cross spreading of martensite occurs in line with the results of [81]. The process of phase transformation relaxes stresses near precipitates (Figure 31b) until the majority of transformation completes. Then, precipitates become stress concentrators due to their higher Young's modulus as before the initiation of phase transformation. During reverse transformation (heating) under constant load, at equal levels of effective strain, the martensite volume fraction and von Mises effective stress fields are very similar to the ones presented in Figure 31.

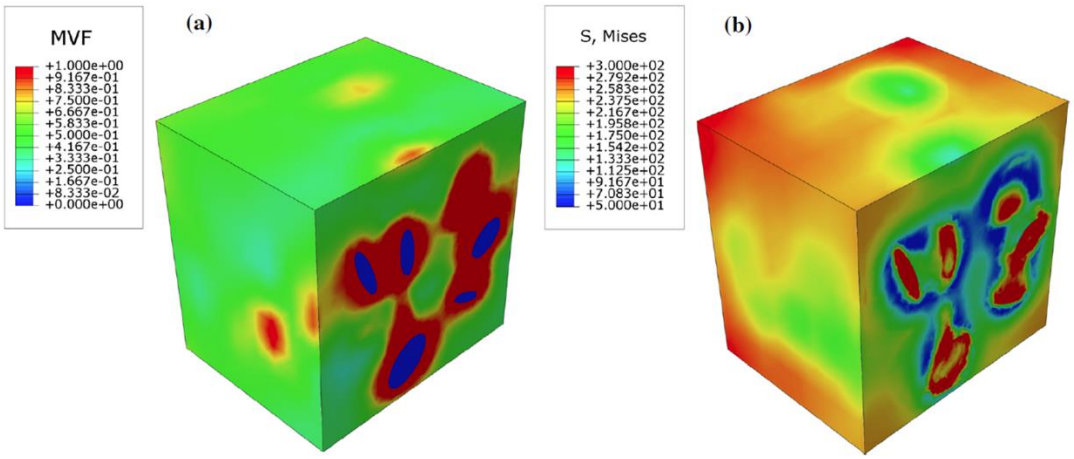

Figure 31. Microstructure during forward transformation under constant load while cooling a) Martensite volume fraction, b) von Mises stress (MPa)

The effects of precipitation on the response during a thermal cycle under constant uniaxial load with respect to multiple volume fractions of particles are examined next. As shown in Figure 32, which displays the effective strain–temperature response of thermally cycled material systems with different precipitate volume fractions, the formation of elastic precipitates at the expense of transformable material decreases the maximum transformation strain. Moreover, the heterogeneous nature of the precipitated microstructure is shown to significantly alter the effective strain–temperature hysteresis loop by shifting the phase transition temperatures to higher values. Additionally, a more gradual or 'smooth' transition from the elastic response to the transformation response (and vice versa) is evident and in accordance to experimental observations. Note that sharp transition from the elastic to transformation response is chosen for the unprecipitated SMA matrix to clearly show that precipitates have a strong impact onto

the gradual transition from the elastic to transformation response observed in experiments. Specifically, it is the heterogeneity of the Ni concentration distribution that results in this gradual transition in the calculations, as it can be seen in Figure 29. Also, from Figure 32, it is shown that the higher the volume fraction of precipitation, the more pronounced the aforementioned effects. Specifically, the 9% case results in smaller maximum transformation strains, a more gradual transition between the elastic and the transformation response, and higher martensitic-start and austenitic-finish temperatures than the 6 and 3% cases.

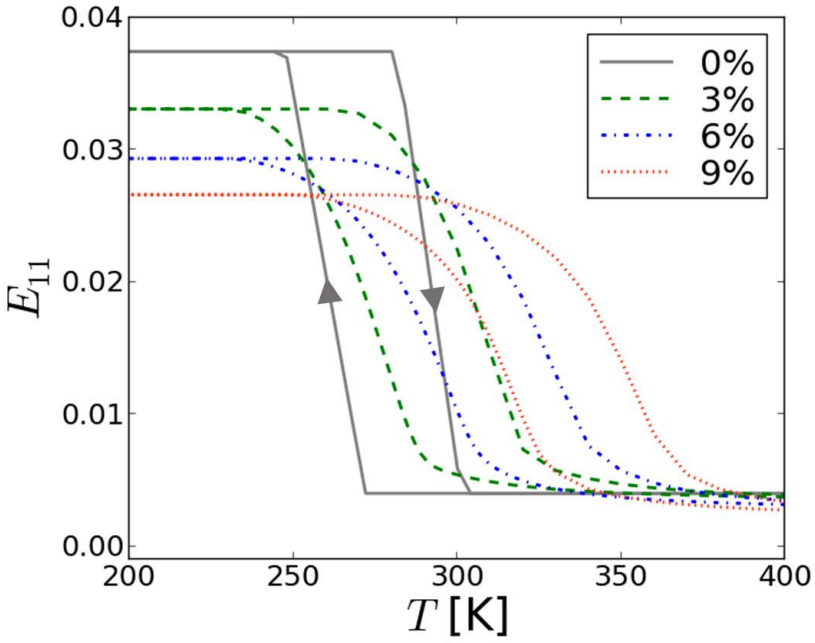

Figure 32. Actuation responses of RVEs with precipitate volume fractions ranging from 0% to 9%

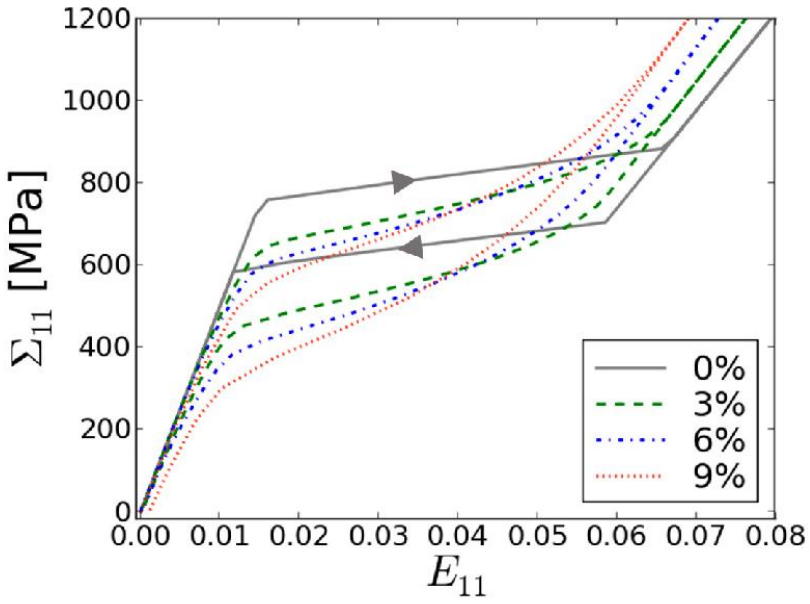

Figure 33. Pseudoelastic responses of RVEs with precipitate volume fractions ranging from 0% to 9%

RVEs were also constructed to explore the pseudoelastic response of materials. In Figure 33, the effective stress–strain response of material systems with different volume fractions of precipitates under a uniaxial loading–unloading cycle at a constant nominal temperature T = 360K is presented. From such simulations, it is noted that as the precipitate volume fraction increases lower critical stresses for initiation and completion of forward and reverse phase transformation, more gradual transitions between the elastic and the transformation response, steeper slopes of the transformation region of the stress–strain curves, and smaller maximum transformation strains are observed. These effects of precipitation on the effective response of Ni-rich NiTi material systems are in agreement with those observed under thermal cycling at a

constant uniaxial load, since a shift of the phase transformation temperatures to higher values results in a decrease in the critical stresses required for initiation and completion of forward and reverse phase transformation in a loading-unloading cycle at a given temperature (Figure 5).

To consider such shifts further, the effective tangent phase diagram of the RVEs is presented in Figure 36 and Figure 37 along with that of the base $Ni_{50.8}Ti_{49.2}$ unprecipitated material. In comparing these two sets of surfaces, a general shift of the composite transformation temperatures to the right is evident. These shifts are associated with local effects induced by the presence of the precipitates-particularly the Ni concentration diffusion. Specifically, by referencing Figure 26 and Table 1, it is noted that the transformation temperatures in the matrix material surrounding the precipitates are substantially higher due to local Ni depletion. Interestingly, the martensitic finish surface does exhibit a smaller magnitude change in temperature than its corresponding start temperatures. This points to the structural effect of the precipitates that results in local stress redistributions that decrease the effective transformation temperatures [82].

Generated Transformation Strain as a Function of Applied Load

The magnitude of the maximum transformation generated in polycrystalline precipitated SMA systems during forward transformation under constant applied load is known to be a function of the applied load [9, 83-85]. This SMA characteristic is explored in Figure 34, in which the effective strain–temperature response is presented as a function of the bias load. Note that this dependence results from the presence of the

precipitates since in the matrix model this dependence is not accounted for, i.e., the maximum transformation strain is a constant in this chapter (Table 2). The higher the applied uniaxial load, the less the 'triaxiality' induced due to the heterogeneity of the microstructure, resulting in higher maximum transformation strain generated in the direction of the applied load. This dependence is further considered in Figure 35, in which the maximum attainable transformation strain at a series of applied load levels is presented. Here, not only the applied load dependence of maximum transformation strain is readily observed, but also a decaying exponential relationship noted in [9, 83-85].

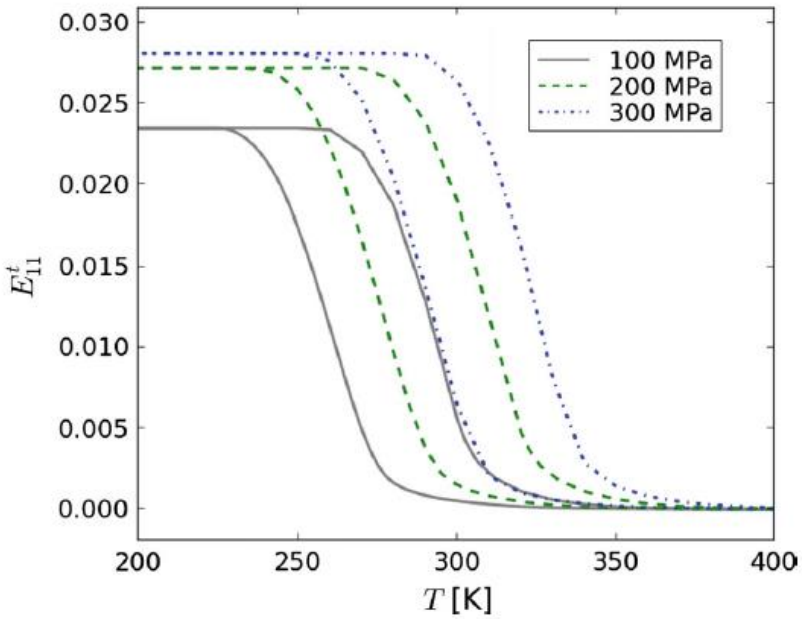

Figure 34. Response of RVE with 3% precipitation at uniaxial tension loads of 100 to 300MPa

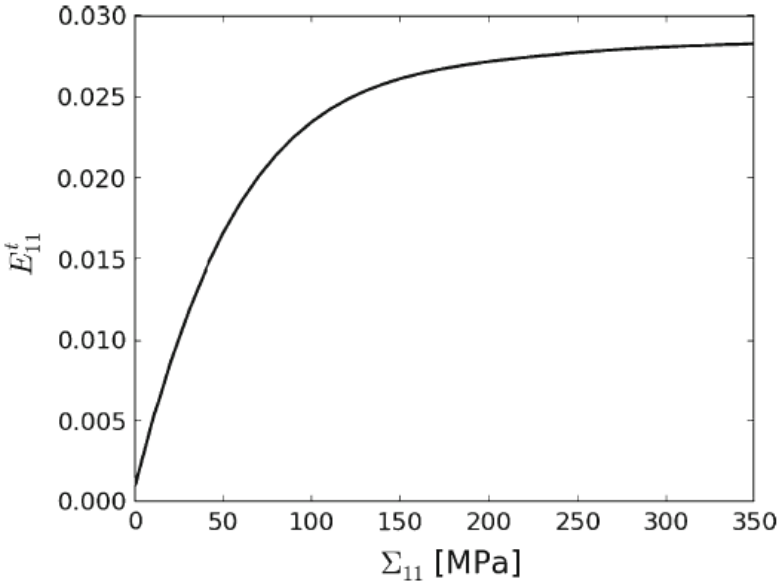

Figure 35. Effective transformation strain in the loading direction as a function of applied load

Homogenization

With the effective response of the RVEs described, a homogenized SMA material is now determined by calibrating the same SMA model used previously for the matrix material (and described in Chapter II) based on the RVE effective response. Calibration details may be found in previous works [9, 29]. The resulting properties of the homogenized SMA material are given in Table 3. The response of the homogenized material for thermal cycles at different bias loads and for pseudoelastic loadings are determined and presented along with the RVE results in Figure 38 and Figure 39. The homogenized simulations show very good agreement with the RVE results in all cases, thereby validating the ability of the model to incorporate the effects of precipitation into the response. This result is not trivial since the effect of precipitates, despite their small

volume fraction, on the homogenized response is profound as it can be seen by comparing it with the response of the material without precipitates (Figure 32 and Figure 33). Importantly, the homogenized responses were determined using single element simulations taking a miniscule fraction of the time that the RVE simulations needed.

Such a capability is necessary, and critical, for predicting the structural response of SMA components with such precipitated materials. In this way, the influences of the microstructure may be brought up to the structural scale.

Table 3. Calibrated material parameters for effective response of 3% precipitated RVE material

Parameter	Value	Parameter	Value
E_A^H (MPa)	50.8	H_{sat}^H	0.0277
E_M^H (MPa)	24.36	k^H (MPa^{-1})	0.015
$\nu_A^H = \nu_M^H$	0.33	M_f^H (K)	156
		M_s^H (K)	334
		A_s^H (K)	206
		A_f^H (K)	354
		C_A^H (MPa K^{-1})	6.4
		C_M^H (MPa K^{-1})	6.6
		$n_1^H = n_2^H = n_3^H = n_4^H$	0.1

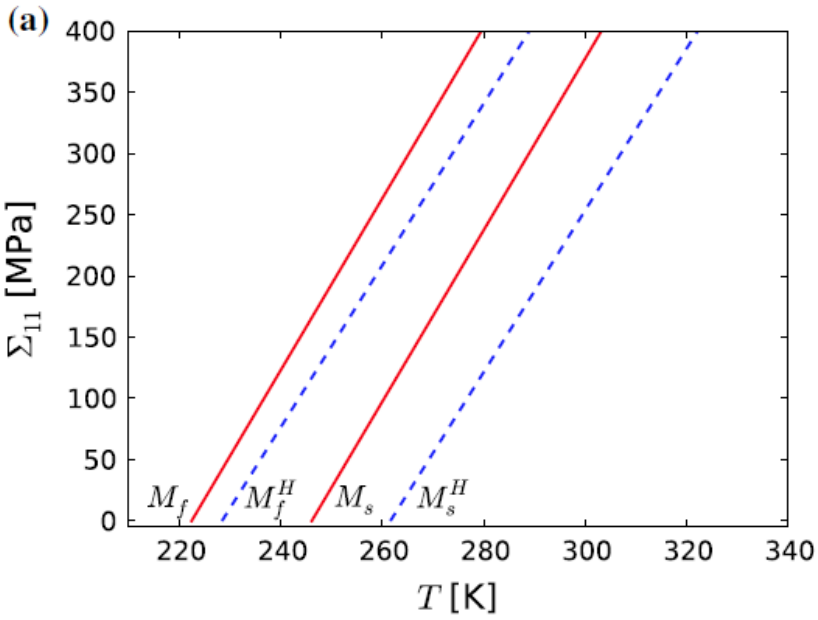

Figure 36. Comparison of homogeneous (solid red lines) and precipitated material's (dashed blue) martensitic Clausius-Clapeyron slopes

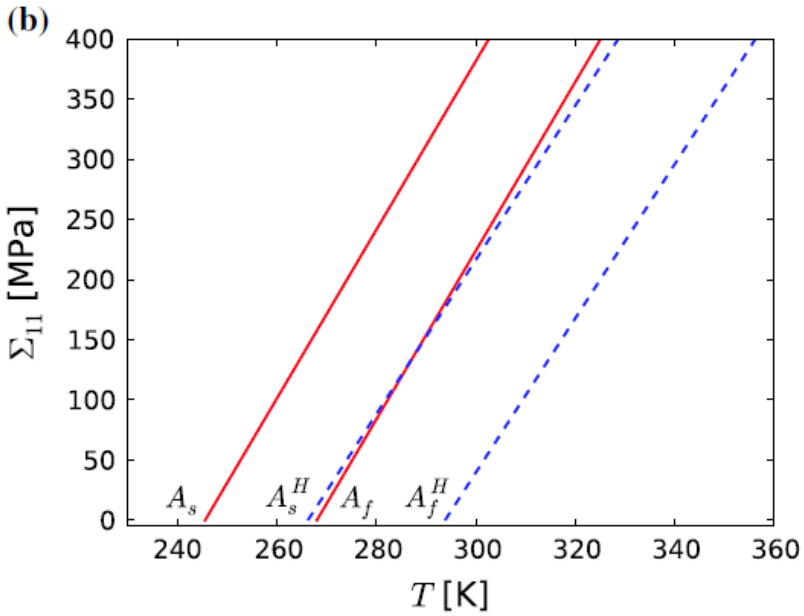

Figure 37. Comparison of homogeneous (solid red lines) and precipitated material's (dashed blue) austenitic Clausius-Clapeyron slopes

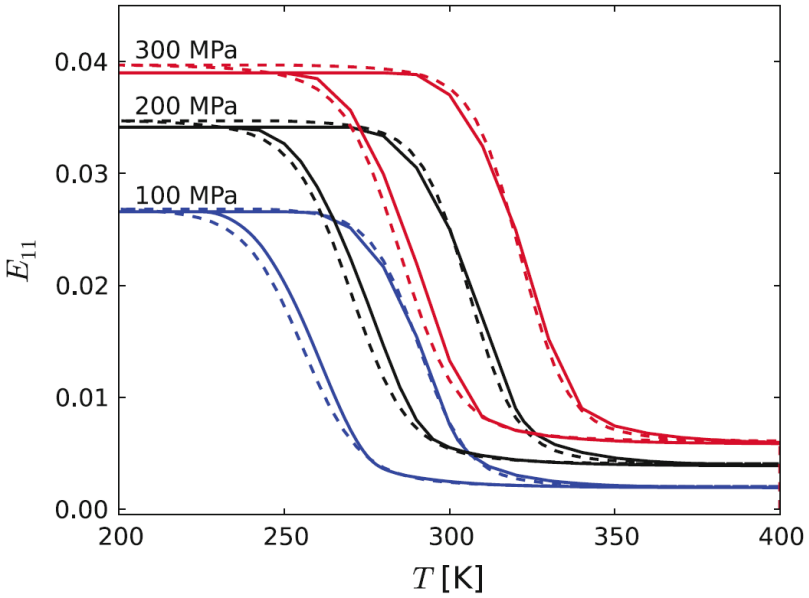

Figure 38. Comparison of homogenized and RVE responses at different bias loads

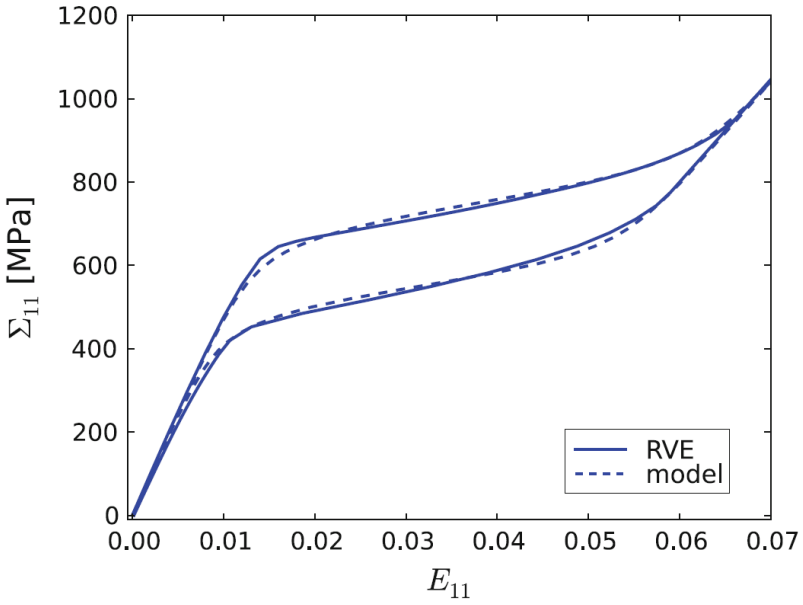

Figure 39. Comparison of homogenized and RVE responses during pseudoelastic loading

Summary

During heat treatment of Ni-rich NiTi SMAs, coherent Ni_4Ti_3 precipitates form by depleting Ni from the matrix. A finite element analysis is carried out to model the macroscopic response of precipitated Ni-rich NiTi SMAs under idealizations of typical loading paths that utilize their actuation effect and pseudoelastic properties. The Ni concentration and coherency stress fields arising due to the lattice mismatch between precipitates and matrix are found to decrease the maximum transformation strain, shift the phase transformation temperatures to higher values, increase the difference between the start and finish temperatures for forward and reverse phase transformation, and result in a gradual transition from the elastic to transformation response and vice versa. The intensity of all these precipitation-induced transformation behavior characteristics increases with precipitate volume fraction. Moreover, the magnitude of the maximum transformation generated during forward transformation under constant applied load is shown to be a monotonic function of the load, with a maximum attainable transformation strain reached at a high level of applied load. All of these trends are in accordance with experimental evidence. The constitutive model employed to describe the matrix behavior is used to calibrate new homogenous macroscopic material properties based on the deformation response of the representative volume elements. The response of the homogenized material is found to be very close to that of the representative volume elements.

CHAPTER IV

PREDICTING PROPERTIES OF PRECIPITATED SMAS

In this chapter, changes to the thermomechanical behavior of Ni-rich NiTi alloys due to heat treatment and subsequent precipitate formation are predicted using a finite element based model. Simulations are run where unprecipitated (solutionized) material responses and Time-Temperature-Transformation (TTT) maps are used as input to create a predicted microstructure representative of the precipitated material which is solved for its macroscopic behavioral response. This microstructural model takes into account both structural effect of precipitates formed during the heat treatment, as well as the change in Ni composition due to precipitate formation. The analysis results in predictions of the Shape Memory Alloy's (SMA's) post-aging responses which are directly compared to experimental results.

Problem Formulation

When designing applications which include SMA materials, each application will have its own requirements for material properties. For example, in actuation driven applications, the material will have a desired transformation strain and ideal range of temperature in which the material will transform. In order to alter the material's transformation temperatures, among other properties, the Ni-rich NiTi SMA material may undergo a processing step where it is kept at elevated temperature (furnace aged) and second-phase Ni-rich Ni_4Ti_3 particles precipitate from the Ni-rich matrix, thereby

reducing the amount of Ni in the matrix and increasing transformation temperatures. The changes in the microstructure which come about through this precipitation drastically alter the material's thermomechanical response [44]. Originally characterized by Nishida et al. and Saburi et al. [86, 87], such particles are known to reduce tansformation-induced plasticity and quickly stabilize actuation response after a few cycles [88]. In contrast, homogeneous unprecipitated materials typically require hundreds of cycles to stabilize the material response [85]. Evidence of this difference in accumulation of irrecoverable deformation throughout cycling can be seen in Chapter I in Figure 6 and Figure 7 where example responses are given for solutionized and precipitated Ni-rich NiTi materials.

Currently, there is no way to accurately predict how the thermomechanical response of such SMA materials will change when precipitated, necessitating that if a material is subjected to a new heat treatment, the final material must be fully re-characterized to determine its new properties. Presently, precipitated SMA material properties are only known for a few initial compositions and aging paths due to the high cost and preparation time needed to produce and characterize the materials. The processing necessary for these materials includes multiple melts, casting, high temperature deformation, machining, solution treatment, and aging, with most steps in an argon purged and vacuum sealed environment. The required precision and complexity of the processing makes it desirable to minimize the number of experiments (and therefore produced materials) required for characterization. With this in mind, we develop numerical models to predict changes to the behavior of SMA materials which

are brought about by precipitation such that properties may be predicted without requiring such lengthy and costly procedures.

In order to determine accuracy of predictions throughout ranges of precipitate volume fraction, NiTi materials of multiple initial compositions and aging paths are studied. A table of the chosen materials and conditions is given below as Table 4.

Table 4. Tested materials detailing initial compositions, processing conditions, and estimation of final precipitate volume fraction.

Initial Composition [Ni at.%]	Aging Temp. [°C]	Aging Time [hr]	Estimated Precipitate VF [%]
50.8	300	100	1.7
50.8	500	24	4.2
51.3	400	100	10.0
51.3	500	100	11.5

Review of Features Incorporated in the RVE Framework

The RVE models which are used for such predictions are able to capture three main features of precipitated microstructures:

(1) Elastic mismatch in the microstructure due to precipitation, with the precipitates defined as linear elastic, and the matrix defined as shape memory material.

(2) Ni diffusion which occurs during the aging process associated with precipitate formation and coarsening. In order to form the Ni-rich precipitates, Ni must be depleted out of the matrix. This depletion is calculated using a 3D Fickian diffusion solver built into Abaqus. The output of this diffusion calculation is a distribution of Ni in

the material which is mapped into transformation temperatures of the constitutive response of the SMA matrix at each integration point.

(3) Coherency of the precipitates. Eigenstrains given in the work of Zhou et al. [72] are able to be induced in the precipitates, accounting for the lattice mismatch of the two phases. This has been shown in Chapter III [89] to have minimal effect on thermomechanical properties in the RVE simulations, and as such is not covered further in this paper. An example meshed RVE is given in Figure 40 for visual reference for the chapter.

Calibrations of Solutionized Material

Materials of two initial compositions are considered in this study. Using the assumption of a 1:1 correlation between Ni content and aging temperature, and the relations of transformation temperature and Ni content given in [4], an average effective Ni content was first estimated for the solutionized (un-aged) materials by converting M_s temperature into Ni content. The lower Ni content material is measured to have a transformation temperature M_s of -2.2°C, correlating to a composition of 50.8 at.%Ni, while the higher Ni content material has a M_s of approximately -120°C, correlating to a Ni content of 51.3 at.%Ni.

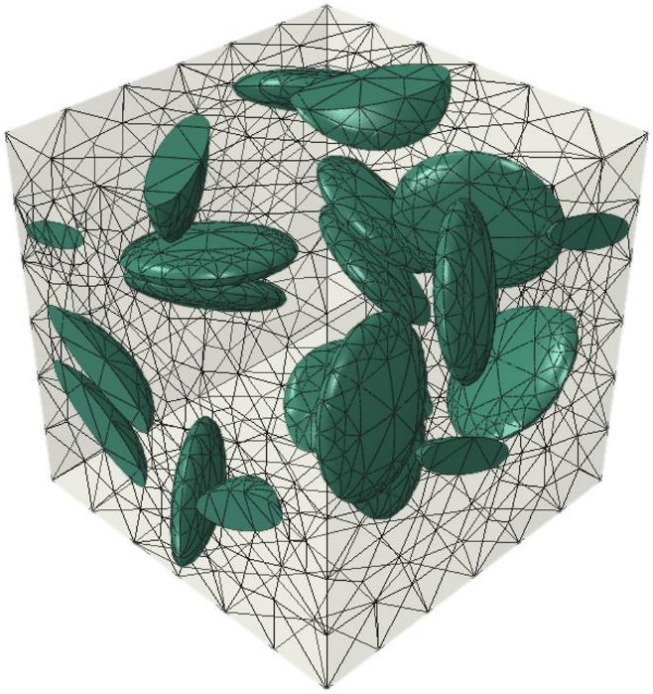

Figure 40. RVE of precipitate and matrix domains showing surface FE meshes

The two solutionized materials will be referred to as 50.8 and 51.3 (in reflection of their estimated atomic Ni composition) for the remainder of the chapter. The solutionized materials are calibrated using parameters of the Lagoudas model where TRIP has been taken out of the material response proportionate to the maximum transformation strain in the cycle. TRIP is measured as the final strain at the end of a cycle minus the strain at the beginning of the cycle. This strain is removed during forward transformation into martensite such that at the beginning of the cycle, strain equal to all measured residual strain is removed, and during cooling in the cycle, strain equal to $TRIP - \left[1 - (\varepsilon - \varepsilon_0)/(\varepsilon_f - \varepsilon_0)\right]$ is removed where ε is the current strain, ε_0 is the initial strain at the beginning of cooling, and ε_f is the final strain at the end of

cooling, such that the strain is taken out proportionately during a cycle. The responses are then moved such that the beginning of the cycle is at zero strain for comparison purposes.

Comparisons of calibration to actual properties are given in Figure 41 and Figure 42. Properties obtained by these calibrations are summarized in Table 5. In determining the calibrated response of the 51.3 solutionized material, it is noted that loading conditions below 200MPa result in minimally usable data since the equipment which is used to conduct the experiment has a thermal limit at -100°C which is in the transformation region of the material.

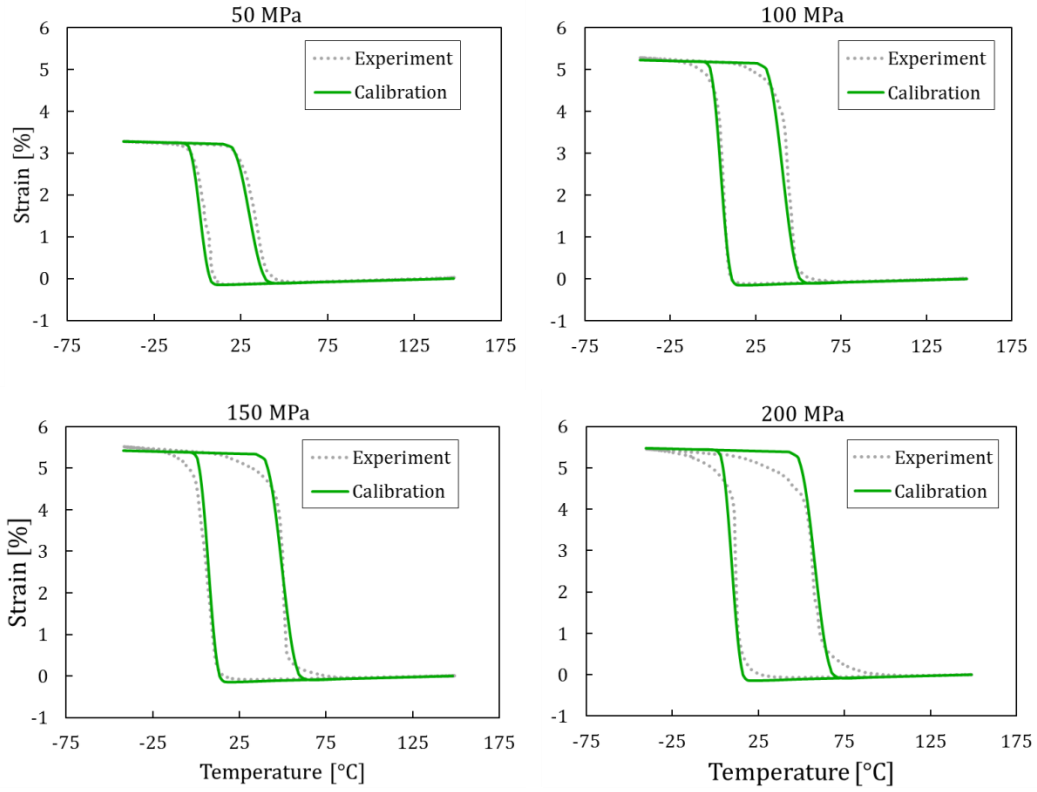

Figure 41. Calibration of homogeneous 50.8 at.%Ni SMA material

Table 5. Calibrated parameters of 50.8 and 51.3 homogeneous materials

Parameter	Value	Parameter	Value (50.8 at.% Ni)	Value (51.3 at.% Ni)
E^A [GPa]	68	H^{min}	0.0	.002
E^M [GPa]	43	H^{max}	0.051	.072
$\nu^A = \nu^M$	0.33	k [MPa^{-1}]	.05	.01
		σ_0 [MPa]	30	25
		C^A [MPa K^{-1}]	6.0	5.5
		C^M [MPa K^{-1}]	6.0	5.5
		$n_1 = n_{...} = n_4$	0.3	0.3

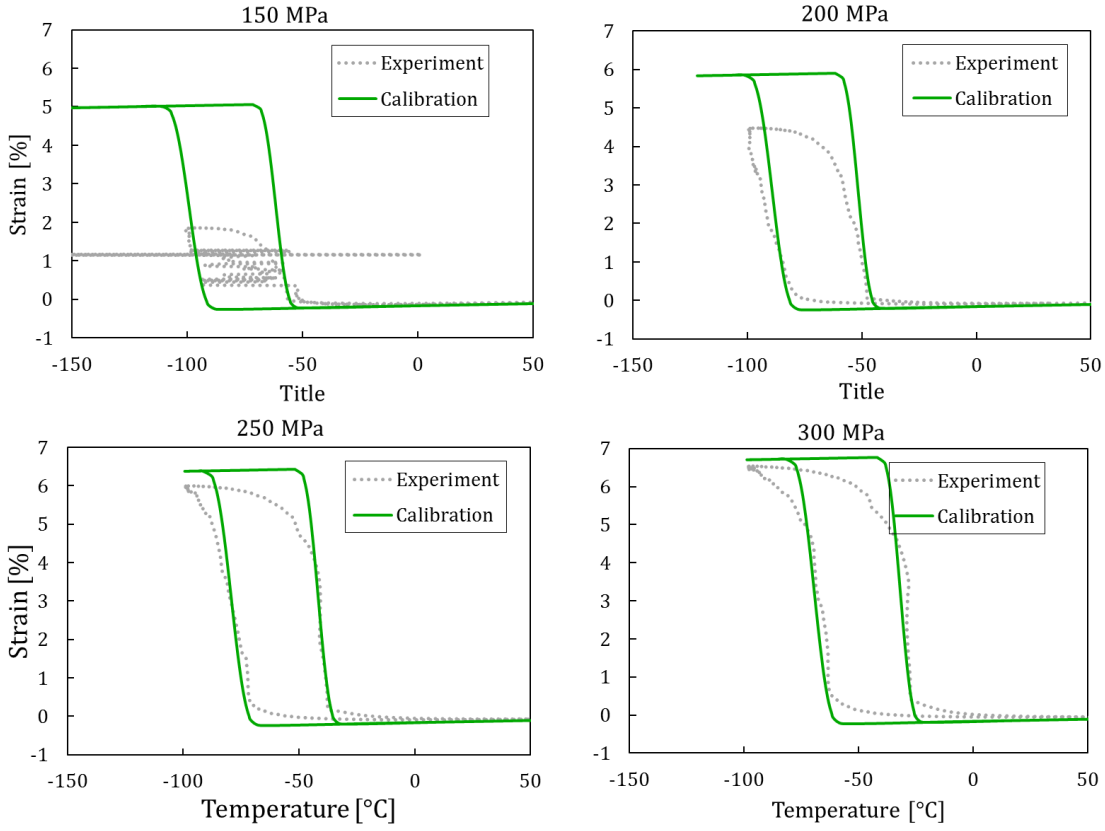

Figure 42. Calibration of homogeneous 51.3 at.%Ni SMA material

Estimated Precipitate Volume Fractions

Once the calibrations are made for the solutionized SMA material, the modeling framework requires an estimation of the volume fraction of precipitates in order to create an RVE to solve for the effective macroscopic response. This volume fraction is determined using (1.17) where the initial and final matrix Ni concentrations are estimated from the M_s transformation temperatures. A step-by-step guide and graphic illustration (Figure 43) is given for the process of estimating precipitate volume fraction:

1. The solutionized material's transformation temperature is measured using a calorimetric technique such as Digital Scanning Calorimetry (DSC).
2. A Time-Temperature-Transformation (TTT) map or DSC result is used to determine the M_s temperature of the final precipitated material after the heat treatment.
3. These two transformation temperatures are converted into estimations of the average Ni content pre- and post-aging using relations given for solutionized materials [4].
4. These Ni content estimations are plugged into (1.17) to determine an estimate of the precipitate volume fraction to be constructed in the RVE model.

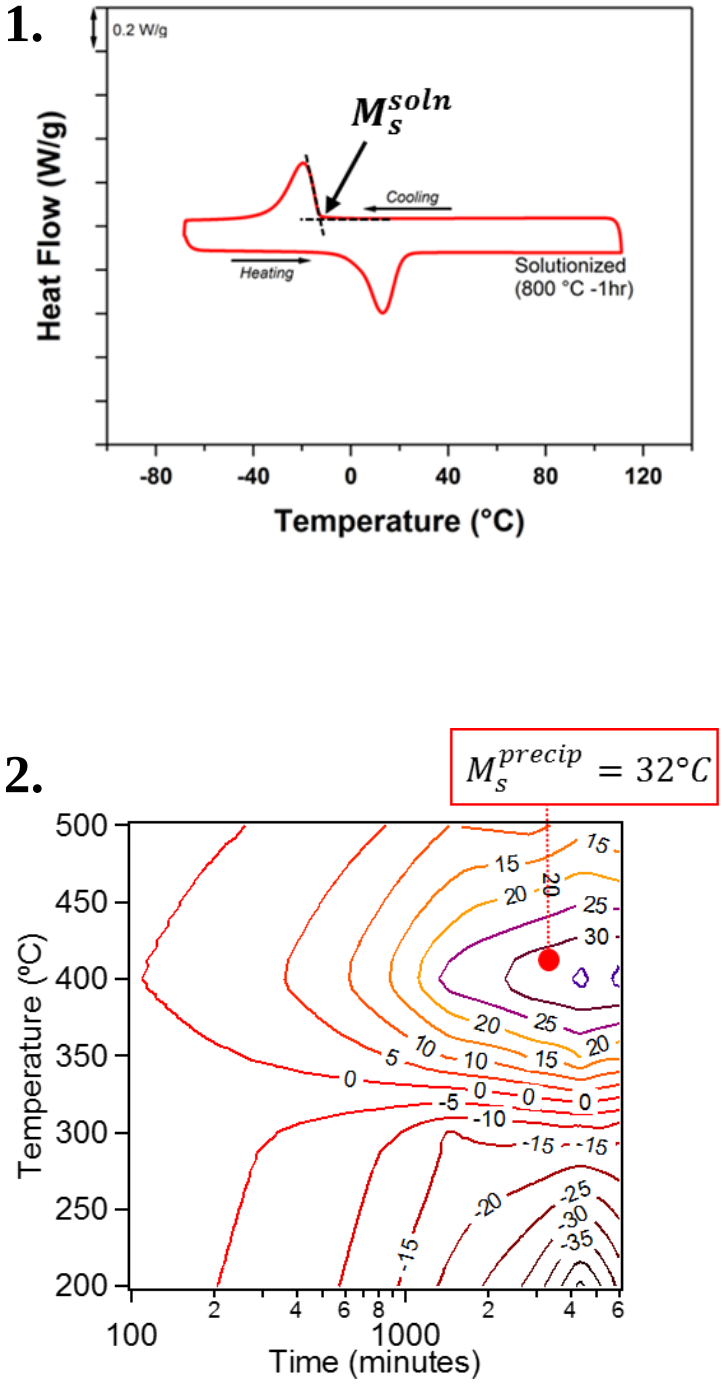

Figure 43. Process for estimation of precipitate volume fraction

3.

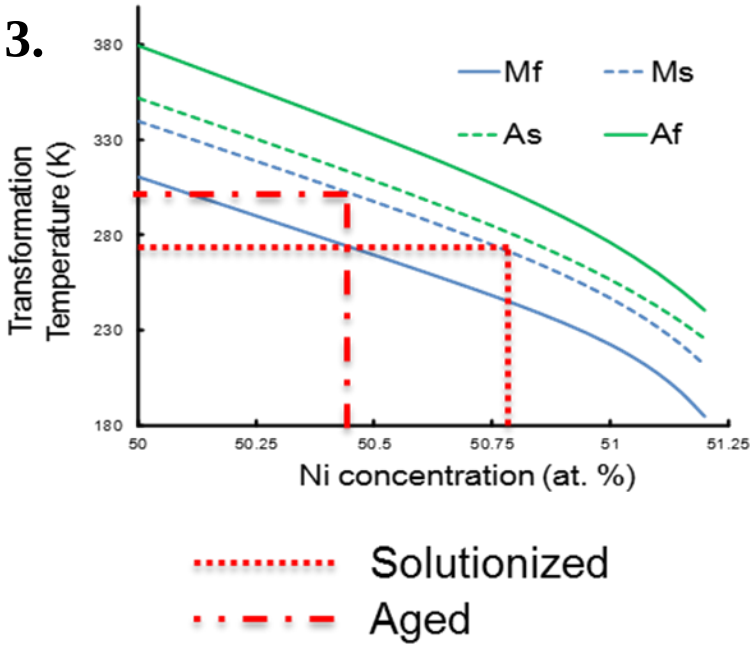

4. $c = vc_{Ni_4Ti_3} + (1 - v)c_A$

Figure 43. Continued

TEM imaging was carried out on specimens in order to determine if appropriate estimates of precipitate volume fraction were made. The images, shown in Figure 44-Figure 46 give evidence that indeed trends in VF estimation are valid, with aging treatments which had higher predicted volume fractions also showing higher volume fractions in TEM images. Also, a RVE cross-section is given in Figure 47 for model comparison.

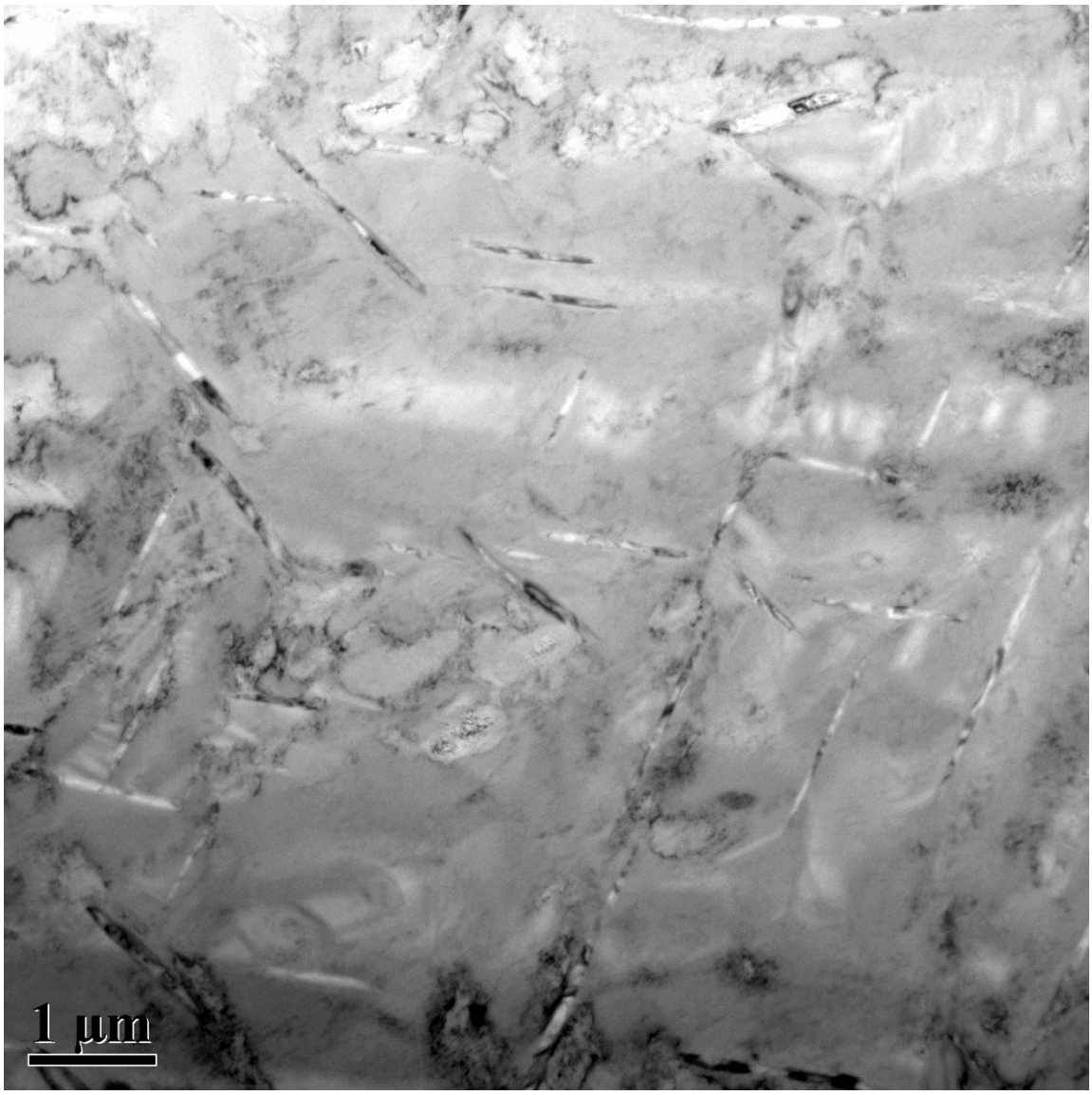

Figure 44. 50.8 material aged at 500°C for 24 hours with estimated VF of 4.2%

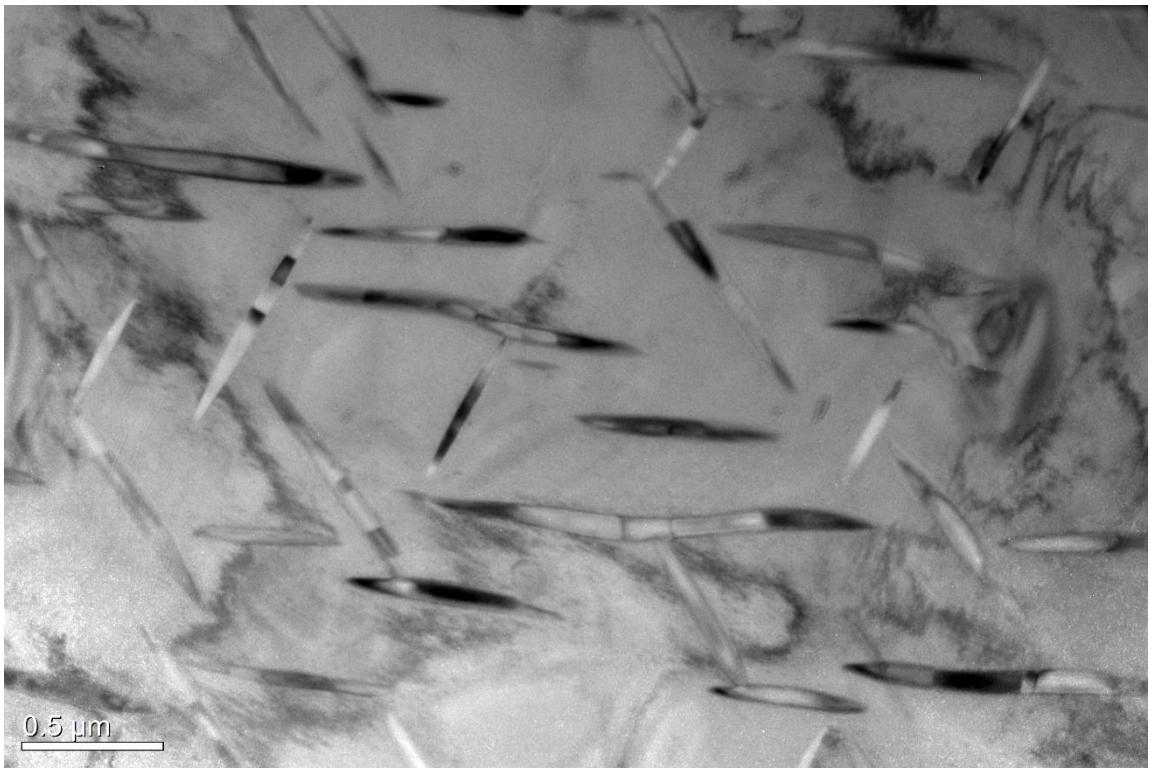

Figure 45. 51.3 material aged at 400°C for 100 hours with estimated VF of 10.0%

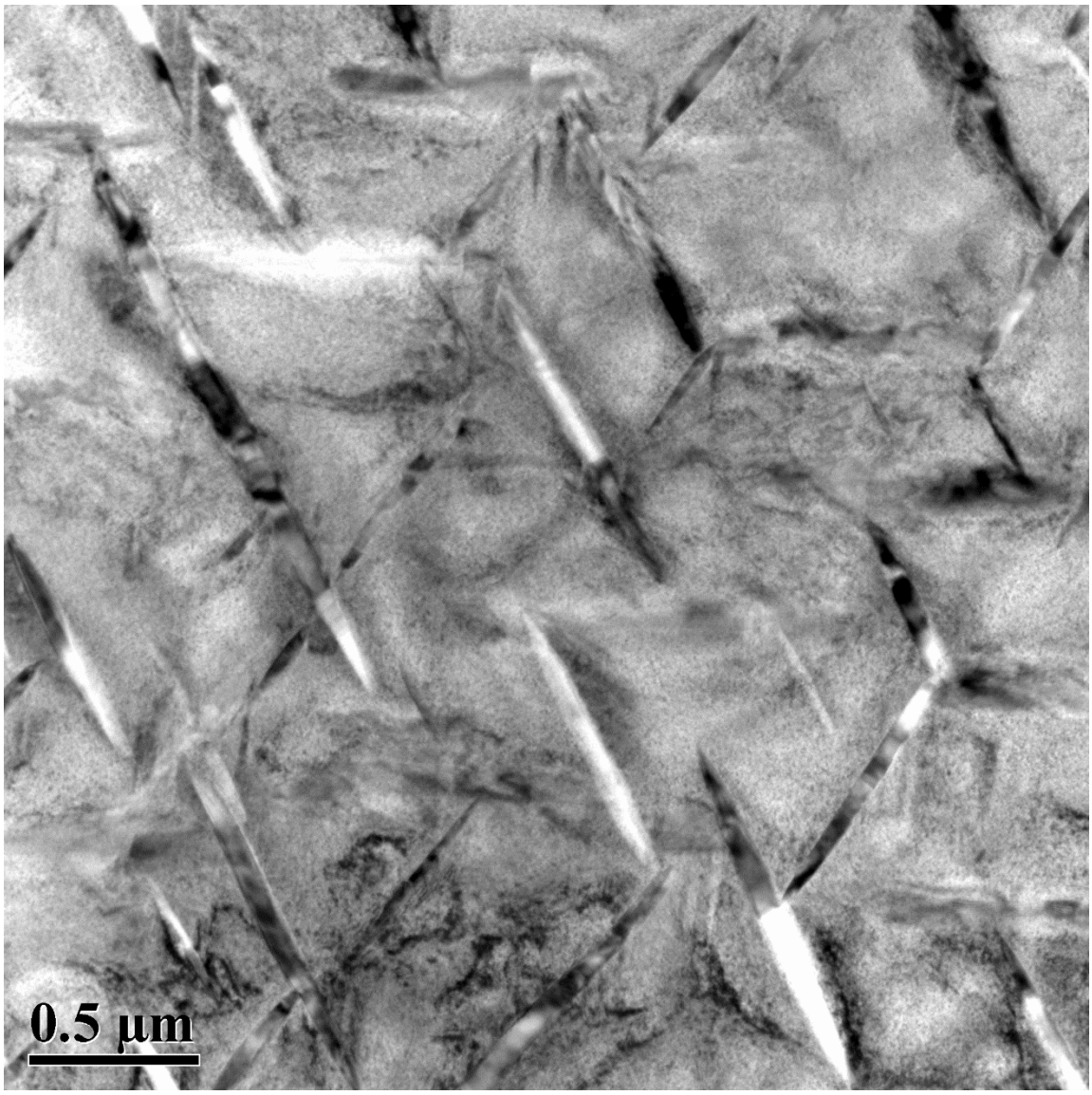

Figure 46. 51.3 material aged at 500°C for 100 hours with estimated VF of 11.5%

For comparison, a cross-section of one of the simulated RVE domains is given. It is noted that the modeled structure quite well represents the TEM images, with the only prominent difference being the higher particle aspect ratio in the TEM images which was assumed 4:1 oblate in the model.

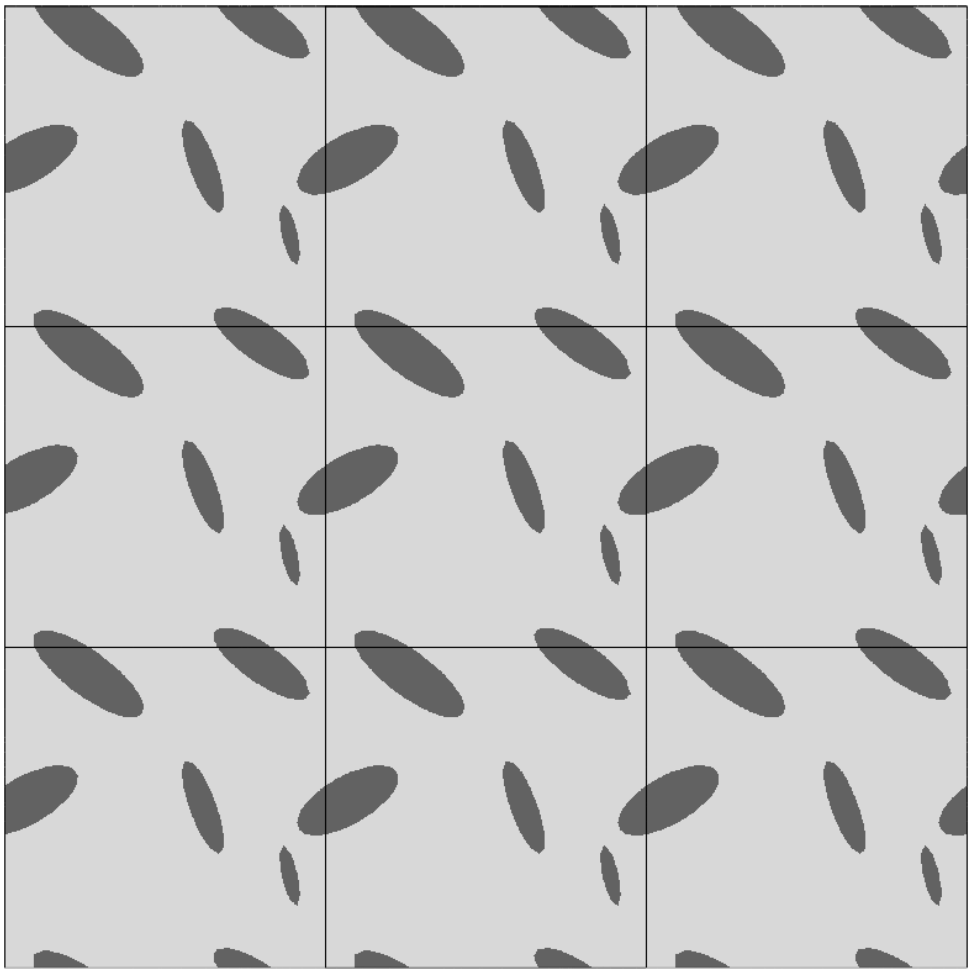

Figure 47. Cross-section of sample RVE for comparison to TEM

Prediction Results

Once estimates of precipitate volume fractions are obtained, predicted microstructures are built and taken through thermomechanical cycling. Responses of these VF ranges are compared to model results in Figure 48-Figure 51. For the responses of precipitated 50.8 material, data is given for 100, 150, and 200MPa bias loads. Since the 51.3 material could not be calibrated below 150MPa, results are given for 150 and 200MPa. For all materials, the expected reductions in transformation occur in relative proportion to the estimated volume fraction of precipitates.

The experimental data reveals that the formation of elastic precipitates at the expense of transformable material decreases the maximum transformation strain. Moreover, the heterogeneous nature of the precipitated microstructure significantly alters the effective strain-temperature hysteresis loop and shifts the phase transition temperatures to higher values.

The predictions of the effective strain-temperature response of thermally cycled 50.8 material aged at 300°C for 100hrs are compared against experimental data in Figure 48. The predictions are able to reproduce quantitatively all the aforementioned precipitation-induced changes in the thermomechanical response. For this material, the estimated volume fraction was 1.7%, showing that the presence of precipitates, even in small quantities, will readily affect the amount of attainable transformation strain at different bias loads. At 100MPa, the transformation strain is reduced from 5% down to 3.5%. This effect is captured quite well by the model which has predicted 3.8%. The model also captures the transformation temperature shift of approximately 20°C.

In the case of 50.8 material aged at 500°C for 24hrs which is shown in Figure 49, the predicted transformation strain is overestimated compared to the experimental data and the same hold trues in general about the phase transition temperatures.

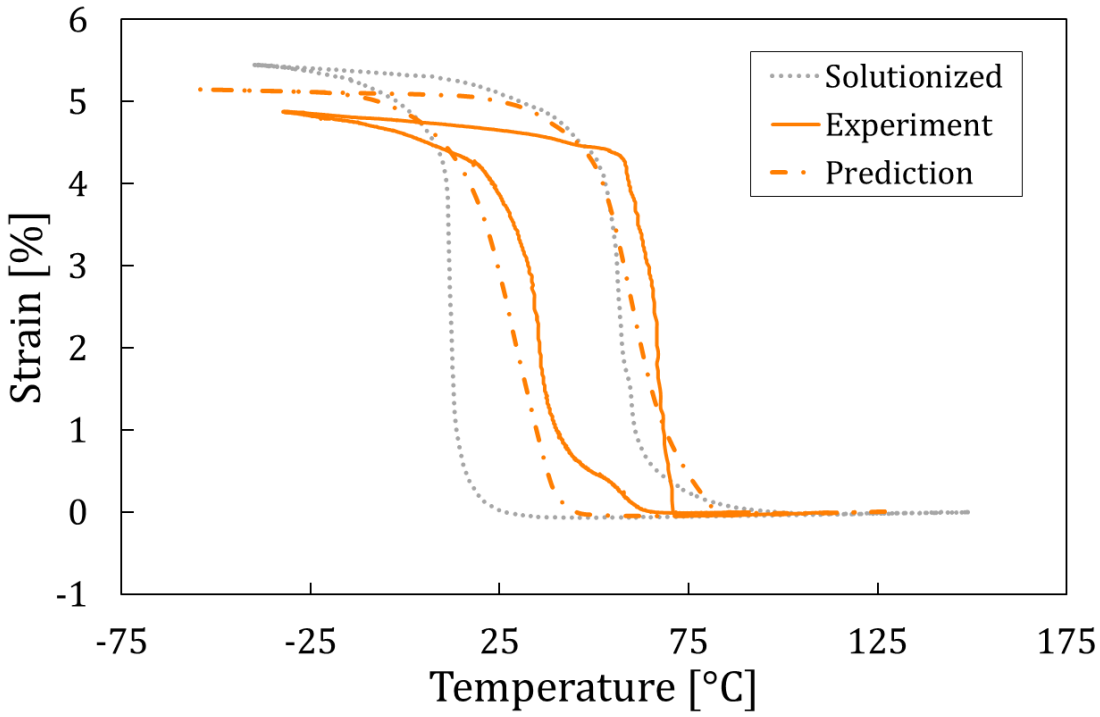

Figure 48. Results at 200, 150 and 100MPa of the 1.7%VF material. Solutionized (unprecipitated) experiment data given as grey dotted line for reference

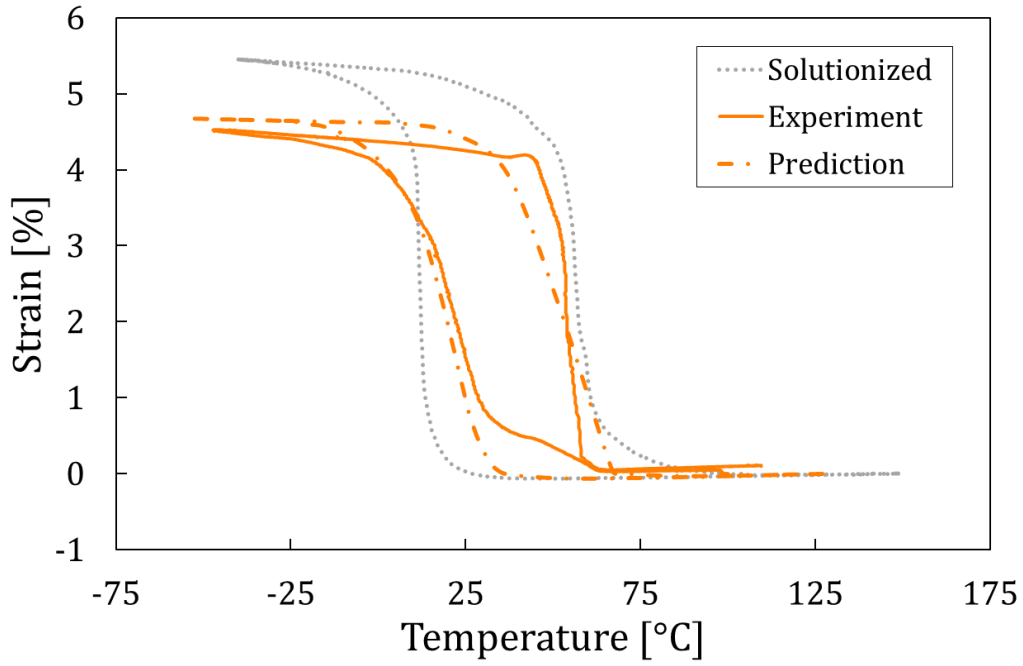

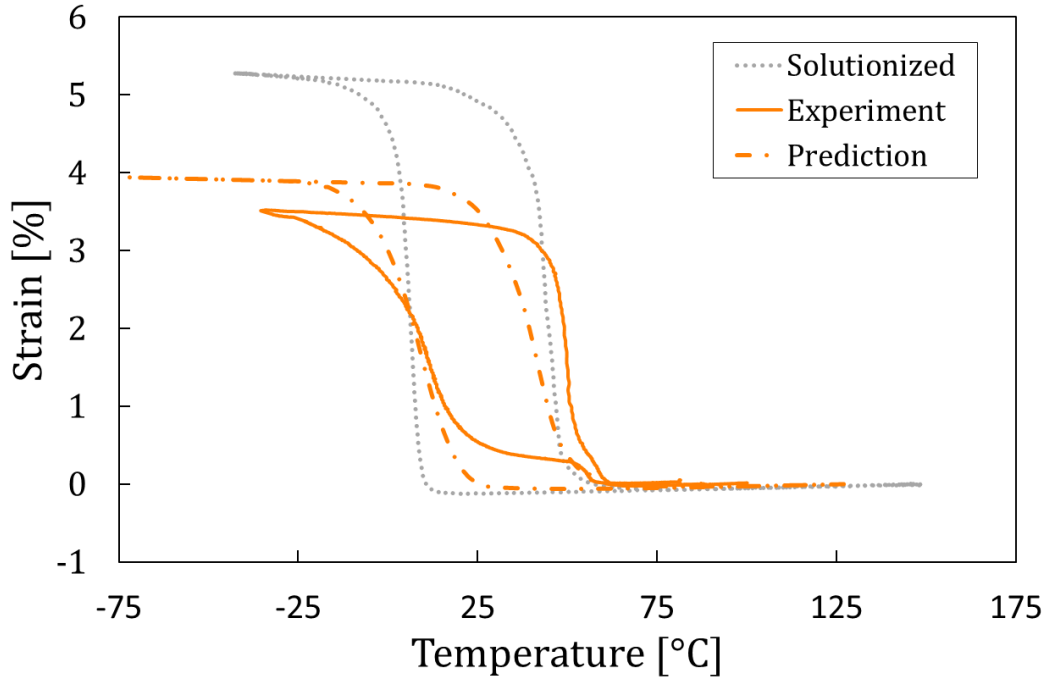

Figure 48. Continued

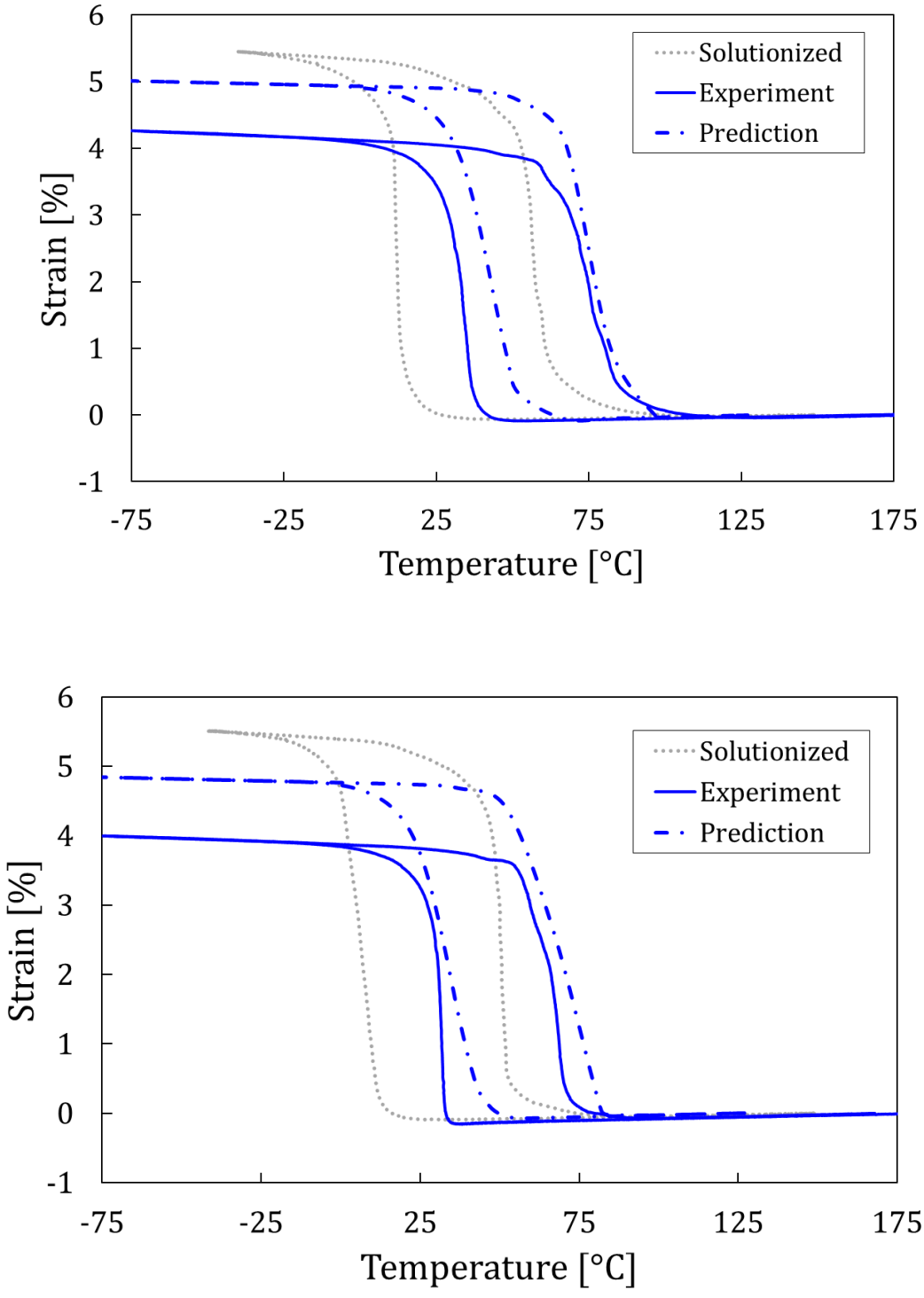

Figure 49. Results of 4.2%VF material at 100, 150 and 200MPa. Solutionized (unprecipitated) given as grey dotted line for comparison

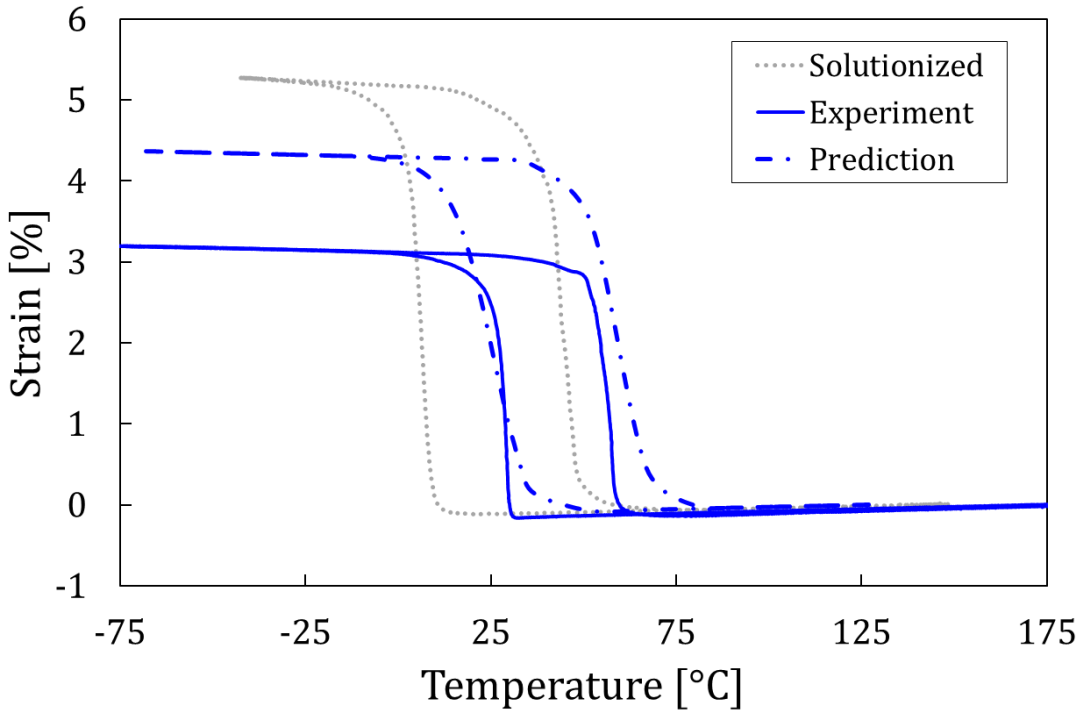

Figure 49. Continued

The 51.3 cases show large reduction in transformation strains as well as massive shifts in transformation temperature (over 100°C). For these cases, much of the reduction in transformation strain is captured. It is also seen that there is a reduction in hysteresis width and sharp transition from martensite to austenite phases, features which are not fully captured in the RVE response. In the case of the 51.3 material aged at 400°C for 100hrs shown in Figure 50, the predictions overestimate the transformation strains while the phase transition temperatures, M_s and A_f, and Clapeyron slopes are in good agreement with the experimentally observed ones. However, a more gradual strain-

temperature response in the transformation regime (transformation slope) is predicted than that observed, resulting in underestimation of M_f and A_s. Similarly, the transformation strain is overestimated for the 51.3 material aged at 400°C for 100hrs in Figure 51, but the M_s temperature and Clapeyron slopes (shift in transformation temperatures with respect to bias load) are in a good agreement with experiments. However, all other phase transition temperatures deviate considerably from the experimentally observed values.

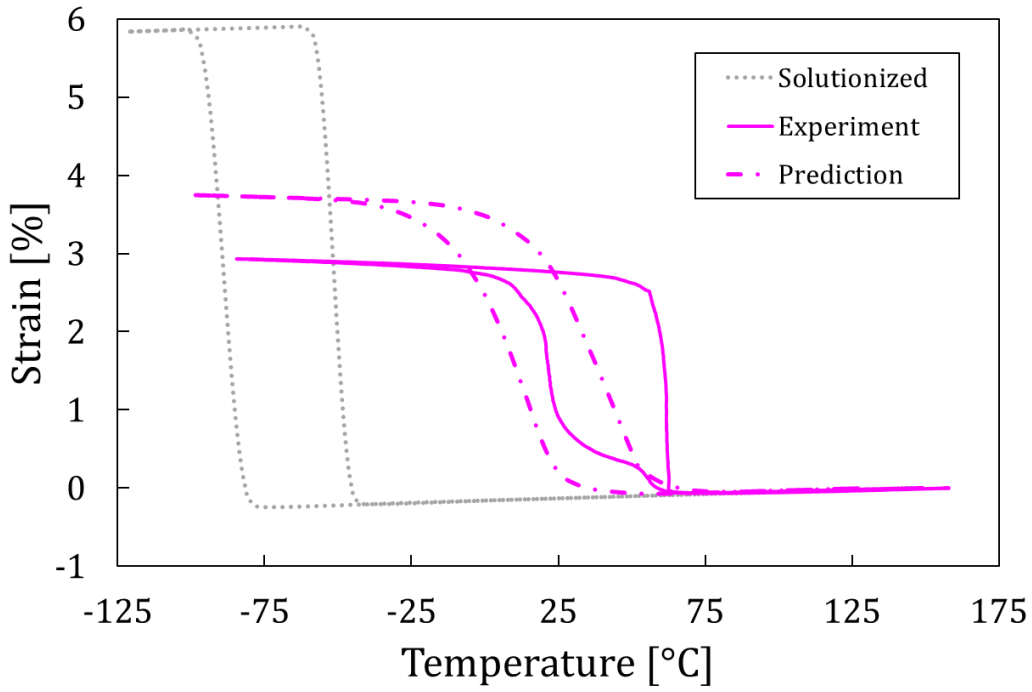

Figure 50. Results of 10.0%VF case at 150 and 200MPa. Solutionized (unprecipitated) given as grey dotted line for comparison

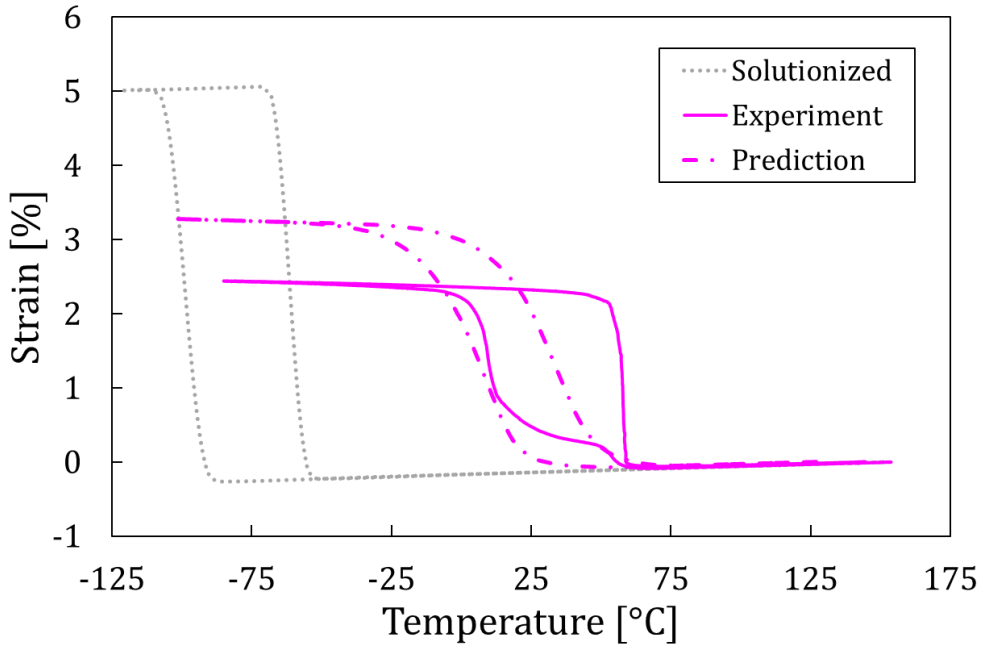

Figure 50. Continued

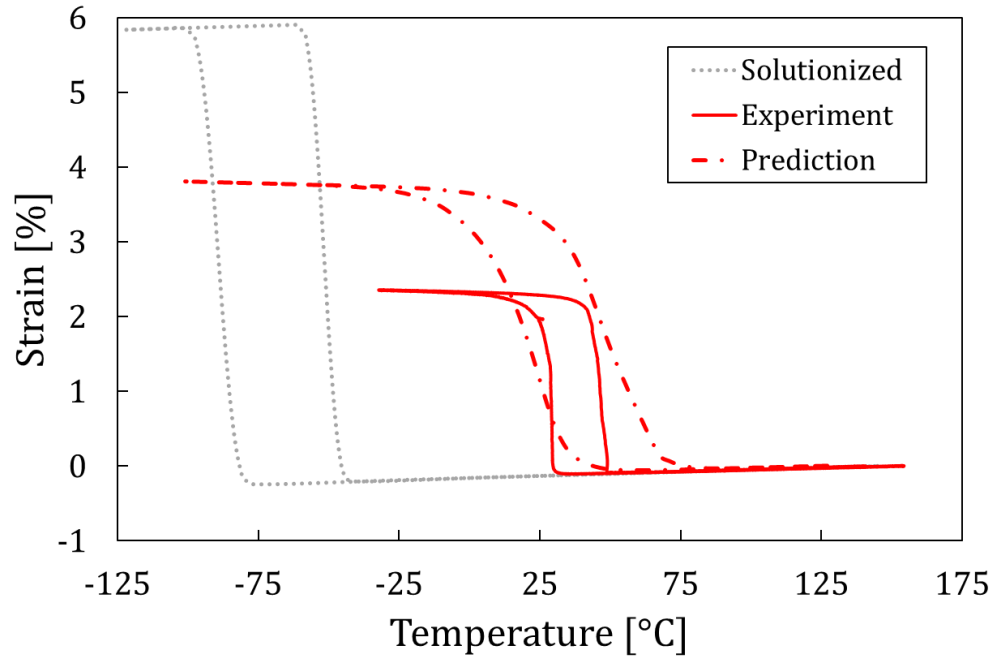

Figure 51. Results 11.5%VF case comparing responses at 150 and 200MPa. Solutionized (unprecipitated) given as grey dotted line for comparison

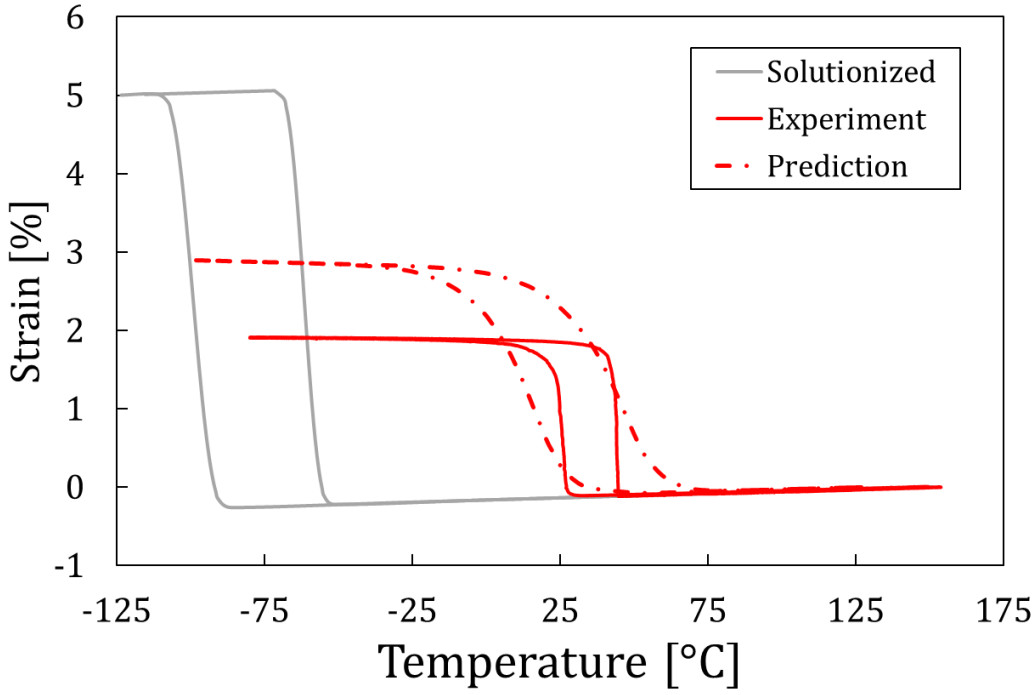

Figure 51. Continued

Model Deviations

As already mentioned, the model in its present form can only capture volume fraction, aspect ratio, and orientations as the main precipitate defining geometric quantities, i.e., to the extent that the constructed RVEs are truly representative of the material microstructure, but not size effects. Size effects arise mostly from the interparticle distance and the surface to volume fraction ratio of the precipitates. Their interaction however is rather complicated hindering a comprehensive discussion of the predictions with respect to these size effects. Nevertheless, an attempt to rationalize the

ability of the model to describe the thermomechanical response of different microstructures is attempted.

In almost all cases, the predictions overestimate the attainable transformation strain. It seems that the complexity of the martensitic microstructure formed (e.g., type and number of active martensitic variants, detwinning, and reoriantation), which impacts the observable macroscopic transformation strain, cannot be captured by the structural, compositional, and single parameter, that of martensite volume fraction, descriptions of the effects of precipitates and martensitic variants on the observable transformation strain.

With respect to the phase transition temperatures, the model captures well the martensitic-start temperatures and the Clapeyron slopes, partly due to the TTT maps used to estimate the former. Moreover, in the 51.3 cases, the slopes of the strain-temperature plots are lower than experimentally observed, irrespective of the interparticle distance and precipitate volume fraction. This is explained by the following. With respect to the fact that a large amount of Ni is being leeched from the SMA matrix to account for the precipitates, and the transformation temperatures are well intertwined with Ni content, the response of the 51.3 material will become dominated by how exactly the computed diffusion proceeds. The model assumption of randomness in particle orientation combined with the diffusion being highly dependent on particle orientation results in a random and smoothly changing distribution of Ni in the SMA matrix, and a hysteresis which transitions very smoothly in the model. In contrast, the experimental material has aligned particles which can give rise to a very different

distribution of Ni in the material matrix, and therefore hysteresis shape, not well matching the assumption of randomly oriented precipitates. These differences in the Ni profile distribution are also exacerbated by the relatively small interparticle distance with respect to particle size.

The sharp transformation upon heating in the experiments is explained by the small interparticle distance of precipitates and high stored elastic energies in the microstructure associated with the inability of precipitates to accommodate atomic lattice shear when martensite variants are formed. These features of transformation will give rise to alternate twinning modes tightly associated with precipitate directionality and result in a quick burst of transformation from martensite into austenite [43].

Summary

The modeling framework described in Chapter II was used to predict responses of NI_4Ti_3 precipitated NiTi SMAs. The predicted responses had only the solutionized material data and a single measured transformation temperature (under no load) of the aged material as inputs, with the full thermomechanical actuation response coming about through the construction and solution of a representative volume element. The results are in quite good agreement for the predictions of the 50.8 material, with the material aged at 300°C for 100hrs having excellent agreement with experimental results. For the 51.3 materials, higher deviations between prediction and experiment are seen, however, a large portion of the changes brought about by the precipitates are still captured, while reasons for deviation are explained in the chapter.

CHAPTER V

CONCLUSIONS AND FUTURE WORK

In this work, a modeling framework grounded in finite elements and using the concept of a representative volume element has been developed to create and solve microstructures representative of precipitated Ni-rich NiTi SMAs in order to explore and predict responses of these materials.

Conclusions

Chapter I gives an introduction to shape memory alloys and their phase change mechanism, and a brief literature review on precipitation in SMAs and the micromechanical methods used to simulate them. It concludes with a brief overview of the layout of the thesis.

Chapter II expounds the details of the modeling framework developed to run the micromechanical simulations summarized in the paper. It gives details of the RVE generation and preprocessing necessary to set up a model for solution in the finite element package Abaqus. It then describes the thermomechanical properties and constitutive responses of the precipitate and matrix phases. Finally it discusses the methods of incorporating the multiple physical processes accounted for in the analysis, namely development of coherency stresses, Ni diffusion, and thermomechanical cycling. Of special note in this chapter is the developed ability to have periodic placement of

particles under periodic boundary conditions, where particles are allowed to cross external boundaries.

Chapter III presents a study in which microstructural simulations explore precipitation in NiTi material. It gives details of precipitation effects on both pseudoelastic and actuation responses, where a range of volume fractions are considered and their effects on the macroscopic material response are shown. It also singles out the effects of coherent particles and Ni distribution by comparing fully developed RVEs to ones with no coherency stresses and a homogeneous distribution of Ni, respectively. It details the effects of precipitation on the effective transformation strain of the material and ends by upscaling the material response to the macroscale and calibrating a currently developed SMA model to the effective RVE response. The introduction of precipitates is seen to decrease the maximum transformation strain, shift the phase transformation temperatures to higher values, increase the difference between the start and finish temperatures for forward and reverse phase transformation, and result in a gradual transition from the elastic to transformation response and vice versa. The intensity of these changes to the transformation behavior characteristics increases with precipitate volume fraction.

Chapter IV describes a study in which the material response of precipitated NiTi alloys are predicted using the developed material modeling framework. It uses an initial calibration of the unprecipitated material and a single caloric measurement of the precipitated material to estimate the precipitate volume fraction and predict the full thermomechanical response of multiple SMA materials for multiple heat treatments. The

study considers two initial Ni compositions, representing a wide range of precipitate volume fractions and phase change properties. It is shown that the effective responses of low precipitate volume fractions can be captured extremely well, and at high volume fractions, general trends are captured while specific details are lost due to increased complexity in martensitic transformation not entirely captured in the model assumptions.

Future Work

For future work in this area, the inverse problem may be attempted where, given a set of target material properties, the framework may be utilized in order to determine the optimal initial material and heat treatment required to produce a material which best fits the desired thermomechanical response.

With respect to the constitutive model used to model the materials, additional information could be added to account for the effects of twinning types which may arise in the precipitated microstructure but are not seen in solutionized material. In addition, phase field methods could also be used to develop more accurate Ni fields for the models.

REFERENCES

[1] K. Otsuka, T. Kakeshita. Science and technology of shape-memory alloys. New developments, MRS. Bull. 27 (2002) 91-100.

[2] M.F.-X. Wagner, W. Windl. Elastic anisotropy of Ni4Ti3 from first principles, Scripta Mater. 60 (2009) 207-210.

[3] J. Michutta, C. Somsen, A. Yawny, A. Dlouhy, G. Eggeler. Elementary martensitic transformation processes in Ni-rich NiTi single crystals with Ni4Ti3 precipitates, Acta Mater. 54 (2006) 3525–3542.

[4] J. Frenzel, E.P. George, A. Dlouhy, C. Somsen, M.F.X. Wagner, G. Eggeler. Influence of Ni on martensitic phase transformations in NiTi shape memory alloys, Acta Mater. 58 (2010) 3444-3458.

[5] J.N. Reddy. An introduction to the finite element method, McGraw-Hill New York, 1993.

[6] K. Otsuka, X. Ren. Physical metallurgy of Ti–Ni-based shape memory alloys, Prog. Mater. Sci. 50 (2005) 511-678.

[7] E. Peraza-Hernandez, D. Hartl, R. Malak. Simulation-based design of a self-folding smart material system. ASME 2013 International Design Engineering Technical Conferences and Computers and Information in Engineering Conference: American Society of Mechanical Engineers, 2013. p.V06BT07A045-V006BT007A045.

[8] H.-J. Kim, S.-H. Song, S.-H. Ahn. A turtle-like swimming robot using a smart soft composite (SSC) structure, Smar. Mat. St. 22 (2013) 014007.

[9] D.J. Hartl, J.T. Mooney, D.C. Lagoudas, F.T. Calkins, J.H. Mabe. Use of a Ni60Ti shape memory alloy for active jet engine chevron application: II. Experimentally validated numerical analysis, Smar. Mat. St. 19 (2010) 015021.

[10] B. Carpenter, J. Lyons. EO-1 technology validation report: Lightweight flexible solar array experiment, NASA/GSFC. Last updated: August 8 (2001).

[11] P.K. Kumar, D.C. Lagoudas. Introduction to Shape Memory Alloys. Shape Memory Alloys, vol. 1. Springer US, 2008. pp. 1-51.

[12] J. Mohd Jani, M. Leary, A. Subic, M.A. Gibson. A review of shape memory alloy research, applications and opportunities, Materials & Design 56 (2014) 1078-1113.

[13] W. Huang. Shape memory alloys and their application to actuators for deployable structures, PhD. Dissertation. University of Cambridge (1998).

[14] J. Kudva. Overview of the DARPA smart wing project, J. Intel. Mat. Syst. Str. 15 (2004) 261-267.

[15] S. Wax, G. Fischer, R. Sands. The past, present, and future of DARPAs investment strategy in smart materials, Journal of Minerals, Metals, and Materials Society 55 (2003) 17-23.

[16] H. Prahlad, I. Chopra. Design of a variable twist tiltrotor blade using shape memory alloy (SMA) actuators. SPIE: Smart Structures and Materials, vol. 4327. Newport Beach, CA, 2001. p.46-59.

[17] D. Kennedy, F. Straub, L. Schetky, Z. Chaudhry, R. Roznoy. Development of an SMA actuator for in-flight rotor blade tracking, Intelligent Material Systems and Structures 15 (2004) 235-248.

[18] V. Birman. Review of mechanics of shape memory alloy structures, Appl. Mech. Rev 50 (1997) 629-645.

[19] D. Mantovani. Shape memory alloys: Properties and biomedical applications, Minerals, Metals and Materials Society 52 (2000) 36-44.

[20] G. Andreasen, T. Hilleman. An evaluation of 55 cobalt substituted nitinol wire for use in orthodontics, American Dental Association 82 (1971) 1373-1375.

[21] S. Thompson. An overview of nickel-titanium alloys used in dentistry, Int Endo J 33 (2000) 297-310.

[22] P. Anderson, D. Pedersen, A. Sivertsen, S. Sangesland. Detailed study of shape memory alloys in oil well applications. Sintef Petroleum Research Tech Report. Trondheim, Norway, 1999.

[23] T.W. Duerig, K. Melton, D. Stöckel. Engineering aspects of shape memory alloys, Butterworth-Heinemann, 2013.

[24] S. Saadat, J. Salichs, M. Noori, Z. Hou, H. Davoodi, I. Bar-On, Y. Suzuki, A. Masuda. An overview of vibration and seismic applications of NiTi shape memory alloy, Smart Mater. St. 11 (2002) 218.

[25] G. Song, N. Ma, H.-N. Li. Application of shape memory alloys in civil structures, Eng. Struct. 28 (2006) 1266–1274.

[26] F. Migliavacca, L. Petrini, M. Colombo, F. Auricchio, R. Pietrabissa. Mechanical behavior of coronary stents investigated through the finite element method, J. Biomech. 35 (2002) 803-811.

[27] L. Petrini, F. Migliavacca. Biomedical applications of shape memory alloys, J. Metall. (2011) 1-15.

[28] D.J. Hartl, D.C. Lagoudas. Aerospace applications of shape memory alloys, P. I. Mech. Eng. G-J Aer. (2007) 535-552.

[29] D. Lagoudas, D. Hartl, Y. Chemisky, L. Machado, P. Popov. Constitutive model for the numerical analysis of phase transformation in polycrystalline shape memory alloys, Int. J. Plasticity 32-33 (2012) 155-183.

[30] K. Fujishima, M. Nishida, Y. Morizono, K. Yamaguchi, K. Ishiuchi, T. Yamamuro. Effect of heat treatment atmosphere on the multistage martensitic transformation in aged Ni-rich Ti-Ni alloys, Mat. Sci. Eng. A-Struct. 438 (2006) 489-494.

[31] Y.N. Liu, M. Blanc, G. Tan, J.I. Kim, S. Miyazaki. Effect of ageing on the transformation behaviour of Ti-49.5 at.% Ni, Mat. Sci. Eng. A-Struct. 438 (2006) 617-621.

[32] A.D. Pelton, J.; Miyazaki, S. Optimization of Processing and Properties of Medical-Grade Nitinol Wire. Int'l Conference on Shape Memory and Superelastic Technologies SMST-2000, 2000. p.361-374.

[33] Z.H. Zhang, J. Frenzel, K. Neuking, G. Eggeler. On the reaction between NiTi melts and crucible graphite during vacuum induction melting of NiTi shape memory alloys, Acta Mater. 53 (2005) 3971-3985.

[34] M. Peltonen, T. Lindroos, M. Kallio. Effect of ageing on transformation kinetics and internal friction of Ni-rich Ni-Ti alloys, J. Alloy Compd. 460 (2008) 237-245.

[35] J. Khalil-Allafi, A. Dlouhy, G. Eggeler. Ni4Ti3-precipitation during aging of NiTi shape memory alloys and its influence on martensitic phase transformations, Acta Mater. 50 (2002) 4255-4274.

[36] W. Tang, B. Sundman, R. Sandstrom, C. Qiu. New modelling of the B2 phase and its associated martensitic transformation in the Ti-Ni system, Acta Mater. 47 (1999) 3457-3468.

[37] R.R. Adharapurapu. Phase transformations in nickel-rich nickel-titanium alloys: influence of strain-rate, temperature, thermomechanical treatment and nickel composition on the shape memory and superelastic characteristics. PhD Dissertation. UC San Diego, 2007.

[38] C. Grossmann, J. Frenzel, V. Sampath, T. Depka, G. Eggeler. Elementary Transformation and Deformation Processes and the Cyclic Stability of NiTi and NiTiCu Shape Memory Spring Actuators, Metall. and Mat. Trans. A 40 (2009) 2530-2544.

[39] M. Rahim, J. Frenzel, M. Frotscher, J. Pfetzing-Micklich, R. Steegmüller, M. Wohlschlögel, H. Mughrabi, G. Eggeler. Impurity levels and fatigue lives of pseudoelastic NiTi shape memory alloys, Acta Mater. 61 (2013) 3667-3686.

[40] J. Frenzel, Z. Zhang, K. Neuking, G. Eggeler. High quality vacuum induction melting of small quantities of NiTi shape memory alloys in graphite crucibles, J. Alloy Compd. 385 (2004) 214-223.

[41] D. Stroz, J. Kwarciak, H. Morawiec. Effect of Aging on Martensitic-Transformation in Niti Shape Memory Alloy, J. Mater Sci. 23 (1988) 4127-4131.

[42] M. Nishida, C.M. Wayman, A. Chiba. Electron-Microscopy Studies of the Martensitic-Transformation in an Aged Ti-51 at-Percent-Ni Shape Memory Alloy, Metallography 21 (1988) 275-291.

[43] E.Y. Panchenko, Y.I. Chumlyakov, I.V. Kireeva, A.V. Ovsyannikov, H. Sehitoglu, I. Karaman, Y.H.J. Maier. Effect of disperse Ti3N4 particles on the martensitic transformations in titanium nickelide single crystals, Phys. Met. Metallogr+ 106 (2008) 577-589.

[44] J.K. Allafi, X. Ren, G. Eggeler. The mechanism of multistage martensitic transformations in aged Ni-rich NiTi shape memory alloys, Acta Mater. 50 (2002) 793-803.

[45] L. Bataillard, J.E. Bidaux, R. Gotthard. Interaction between microstructure and multiple-step transformation in binary NiTi alloys using in-situ transmission electron microscopy observations, Philos. Mag. A 78 (1998) 327-344.

[46] E. Hornbogen. The Effect of Variables on Martensitic-Transformation Temperatures, Acta Metall. Mater 33 (1985) 595-601.

[47] P.W. Voorhees. The Theory of Ostwald Ripening, J. Stat. Phys. 38 (1985) 231-252.

[48] G. Madras, B.J. McCoy. Temperature effects on the transition from nucleation and growth to Ostwald ripening, Chem. Eng. Sci. 59 (2004) 2753-2765.

[49] S. Shabalovskaya. Biological aspects of TiNi alloy surfaces, J. Phys. IV 5 (1995) C8-1199-C1198-1204.

[50] L. Machado, M. Savi. Medical applications of shape memory alloys, Braz. J. Med. Biol. Res. 36 (2003) 683-691.

[51] J.D. Eshelby. The Determination of the Elastic Field of an Ellipsoidal Inclusion, and Related Problems, Proc. R. Soc. Lon. Ser.-A 241 (1957) 376-396.

[52] Z.K. Lu, G.J. Weng. Martensitic transformation and stress-strain relations of shape-memory alloys, J. Mech. Phys. Solids 45 (1997) 1905-1928.

[53] Z.K. Lu, G.J. Weng. A self-consistent model for the stress-strain behavior of shape-memory alloy polycrystals, Acta Mater. 46 (1998) 5423-5433.

[54] C. Collard, T. Ben Zineb, E. Patoor, M.O. Salah. Micromechanical analysis of precipitate effects on shape memory alloys behaviour, Mat. Sci. Eng. A-Struct. 481 (2008) 366-370.

[55] C.B.Z. Collard, T. Simulation of the effect of elastic precipitates in SMA materials based on a micromechanical model, Compos. Part B-Eng. 43 (2012) 2560-2576.

[56] Y. Benveniste. A New Approach to the Application of Mori-Tanaka's Theory in Composite Materials, Mech. Mater. 6 (1987) 147-157.

[57] H.A. Luo, G.J. Weng. On Eshelby's inclusion problem in a three-phase spherically concentric solid, and a modification of Mori–Tanaka's method, Mech. Mater. 6 (1987) 347–361.

[58] K. Tanaka, T. Mori. Average stress in matrix and average elastic energy of materials with misfitting inclusions, Acta Metall. Mater. 21 (1970) 571–574.

[59] G.J. Weng. Some elastic properties of reinforced solids, with special reference to isotropic ones containing spherical inclusions, Int. J. Eng. Sci. 22 (1984) 845–856.

[60] J.G. Boyd, D.C. Lagoudas. Thermomechanical Response of Shape Memory Composites, J. Intel. Mat. Syst. Str. 5 (1994) 333-346.

[61] J.G.L. Boyd, D.C. A thermodynamical constitutive model for the shape memory materials. Part I. The monolithic shape memory alloy, Int. J. Plasticity 12 (1996) 805-842.

[62] V. Birman. Properties and response of composite material with spheroidal super elastic shape memory alloy inclusions subject to three dimensional stress state, J. Phys. D Appl. Phys. 43 (2010) 225402.

[63] T. Mura. Micromechanics of defects in solids, Springer Science & Business Media, 1987.

[64] V. Buryachenko. Micromechanics of heterogeneous materials, Springer Science & Business Media, 2007.

[65] S. Nemat-Nasser, M. Hori. Micromechanics: overall properties of heterogeneous materials, Elsevier, 2013.

[66] J. Qu, M. Cherkaoui. Fundamentals of Micromechanics of Solids, Wiley, Hoboken, New Jersey, 2006.

[67] T. Kanit, S. Forest, I. Galliet, V. Mounoury, D. Jeulin. Determination of the size of the representative volume element for random composites: Statistical and numerical approach, Int. J. Solids Struct. 40 (2003) 3647–3679.

[68] B. Widom. Random Sequential Addition of Hard Spheres to a Volume, J. Chem. Phys. 44 (1966) 3888-3894.

[69] O. Pierard, C. González, J. Segurado, J. Llorca, I. Doghri. Micromechanics of elasto-plastic materials reinforced with ellipsoidal inclusions, Int. J. Solids Struct. 44 (2007) 6945-6962.

[70] V.-D. Nguyen, E. Béchet, C. Geuzaine, L. Noels. Imposing periodic boundary condition on arbitrary meshes by polynomial interpolation, Comp. Mater. Sci. 55 (2012) 390-406.

[71] S. Li, A. Wongsto. Unit cells for micromechanical analyses of particle-reinforced composites, Mech. Mater. 36 (2004) 543–572.

[72] N. Zhou, C. Shen, M.F.X. Wagner, G. Eggeler, M.J. Mills, Y. Wang. Effect of Ni4Ti3 precipitation on martensitic transformation in Ti-Ni, Acta Mater. 58 (2010) 6685-6694.

[73] D. Lagoudas, Z. Bo, M.A. Qidwai. A unified thermodynamic constitutive model for sma and finite element analysis of active metal matrix composites, Mech. Compos. Mater. Struct. 4 (1996) 153–179.

[74] D.C. Lagoudas. Shape Memory Alloys: Modeling and Engineering applications, Springer US, 2008.

[75] S. Lejeunes, S. Bourgeois. Abaqus plugins for generating boundary conditions for homogenization problems. 2010.

[76] Abaqus. Analysis User's Manual. Woodlands Hills, CA: Dassault Systèmes of America Corp., 2009.

[77] B. Azadi, R.K.N.D. Rajapakse, D.M. Maijer. One-dimensional thermomechanical model for dynamic pseudoelastic response of shape memory alloys, Smart Mater. Struct. 15 (2003) 429–442.

[78] C. Grabe, O.T. Bruhns. On the viscous and strain rate dependent behavior of polycrystalline NiTi, Int. J. Solids Struct. 45 (2008) 1876–1895.

[79] D. Schryvers, W. Tirry, Z.Q. Yang. Measuring strain fields and concentration gradients around Ni4Ti3 precipitates, Mat. Sci. Eng. A-Struct. 438 (2006) 485-488.

[80] K. Terada, M. Hori, T. Kyoya, N. Kikuchi. Simulation of the multi-scale convergence in computational homogenization approaches, Int. J. Solids Struct. 37 (2000) 2285-2311.

[81] S.D. A. Kröger, J. Frenzel, Ch. Somsen, A. Dlouhy, G. Eggeler. Direct transmission electron microscopy observations of martensitic transformations in Ni-rich NiTi single crystals during in situ cooling and straining, Mater. Sci. Eng. A-Struct. 481 (2008) 452-456.

[82] B.T. Lester, Y. Chemisky, D.C. Lagoudas. Transformation characteristics of shape memory alloy composites, Smart Mater. Struct. 20 (2011) 094002.

[83] Z. Bo, D.C. Lagoudas. Thermomechanical modeling of polycrystalline SMAs under cyclic loading, Part I: theoretical derivations, Int. J. Eng. Sci. 37 (1999) 1089–1140.

[84] Z. Bo, D.C. Lagoudas, D. Miller. Material characterization of SMA actuators under nonproportional thermomechanical loading, J. Eng. Mater. Technol. Trans. ASME 121 (1999) 75–85.

[85] D.J. Hartl, D.C. Lagoudas, F.T. Calkins, J.H. Mabe. Use of a Ni60Ti shape memory alloy for active jet engine chevron application: I. Thermomechanical characterization, Smart Materials and Structures 19 (2010) 015020.

[86] T. Saburi, S. Nenno, T. Fukuda. Crystal structure and morphology of the metastable X phase in shape memory Ti-Ni alloys, Journal of the Less Common Metals 125 (1986) 157-166.

[87] M. Nishida, C.M. Wayman, R. Kainuma, T. Honma. Further electron microscopy studies of the Ti11 Ni14 phase in an aged Ti52at%Ni shape memory alloy, Scripta Metall. Mater. 20 (1986) 899-904.

[88] G. Eggeler, E. Hornbogen, A. Yawny, A. Heckmann, M. Wagner. Structural and functional fatigue of NiTi shape memory alloys, Mat. Sci. Eng. A-Struct. 378 (2004) 24-33.

[89] T. Baxevanis, A. Cox, D.C. Lagoudas. Micromechanics of precipitated near-equiatomic Ni-rich NiTi shape memory alloys, Acta Mech. 225 (2014) 1167-1185.

[90] M.S. Qidwai, A.C. Lewis, A.B. Geltmacher. Using image-based computational modeling to study microstructure–yield correlations in metals. Acta Mater. 57 (2009) 4233-4247.